博士論文　（要約）

Development of Neural Network Potentials to Study Atomic Diffusion Behaviors in Amorphous Materials

（アモルファス材料中の原子拡散挙動の研究のためのニューラルネットワーク・ポテンシャルの開発）

Department of Materials Engineering

The University of Tokyo

李 文文

Li Wenwen

CONTENTS

Chapter 1

Introduction

With the development of nanotechnology, many new materials and devices with great research values and a vast range of prospects in applications were proposed. Recently, some nanoscale information and energy devices, whose operation depends on the control of atomic diffusion, have drawn a lot of research attentions. For example, the working mechanism of resistive random access memory (RAM), an emerging memory device, is immediately related to the diffusion of metal ions or the oxygen vacancies under a bias voltage. The diffusion rate has a significant influence on many key properties of resistive RAM, such as the switching time and turn-on voltage. Another example is the all-solid-state battery. As a battery, the operation of all-solid-state battery inevitably involves the ionic transportation between the two electrodes, and the ionic conductivity can greatly impact the performance of the battery. However, the sputtering and pulsed laser deposition techniques, which are frequently used in the fabrication of nanoscale devices, tend to make the form of materials amorphous in many devices. Therefore, the atomic diffusion in amorphous materials is a widely seen phenomenon. However, our understanding on this phenomenon is still very poor.

Atomistic simulations have been a very powerful tool to reveal the structural evolution in atomic level. However, the application of atomistic simulations in the theoretical study of atomic diffusion in amorphous materials was hindered by the complex and stochastic structure of the amorphous matrix. A systematical simulation method is needed. In this dissertation, we tackle with this issue by the combination of first-principle simulation and machine-learning techniques.

In this introductory chapter, we briefly review two kinds of nanoscale devices, *i.e.* atomic switch and all-solid-state battery, because the research topics discussed in Chapters 3, 4 and 5 stemmed from these devices. In addition, previous atomistic simulations of diffusion in

amorphous materials are reviewed. Afterward, an breif review of the neural network potential, a merging simulation techniques, is given. Finally, we describe the objectives of the present study and give the organization of this dissertation.

1.1 Atomic switch

The resistive random access memory (ReRAM) is a kind of nano information devices. Usually, they have a metal-oxide-metal sandwich structure. The operation mechanism of atomic switch depends on the oxidation/reduction reaction under external bias voltages, which changes the resistance of device.[1] The ReRAM can be categorized into two types according to the working mechanism: the electrochemical metallization memories in which the diffusion particle is thought to be metal cations, and the valance change memories, in which the diffusion particle is oxygen anions or vacancies.

The electrochemical metallization memory is also called atomic switch.[2] D. Eigler firstly introduced the term “atomic switch” in 1991.[3] The device they proposed can controlled the atom transfer between the tip of scanning tunneling microscope and the surface of the sample. By absorbing the transfer atoms to different sites, the resistance of the sample can be changed by one order of magnitude. As the development of atomic switch, the precipitation of metal atoms in the electrolyte materials was increasingly used in the operation of device. These mechanically control the atomic switch has attracted intensive research attention.

At the early stage of atomic switch development, the performance and application of atomic switch are overshadowed by the rapidly-developed semiconductor transistors, which are widely used as the logical cell and memory devices of von-Neumann computers in the present day. To increase the computational power, more and more semiconductor computation elements need to be integrated into one chip, which demands the further down-scaling of transistors. However, due to the quantum tunneling, the limitation of transistor down-scaling is supposed to be 7 nm. On the other hand, owing to its unique working mechanism, the atomic switch shows several excellent characteristics, such as non-volatility and scalability. These characteristics have made it a promising candidate for substituting the semiconductor transistors in the future computer.

1.1.1 Types of atomic switch

The atomic switch can be classified into gap-type and gapless-type according to the structure of device. The gap-type is firstly proposed. The switching of resistance in gap-type atomic switch depends on the growth/shrink of metallic nanowire that controlled electrically.[4] Figure 1.1(a) shows how the Ag nanowire grow from the surface of an Ag_2S crystal under an electron beam irradiation of scanning electron microscope (SEM). Injection of electrons from the SEM tip causes the reduction reaction of Ag^+ ions and formation of Ag nanodots on the Ag_2S surface. In contrast to SEM, the scanning tunnelling microscope (STM) can both inject and extract electrons by changing the bias voltage applied between tip and sample. When electrons are injected into the Ag_2S, the Ag^+ cations are reduced, resulting in the precipitation of Ag atoms on the surface of Ag_2S crystal. On the other hand, the electron extraction causes the oxidation of the precipitated Ag atoms. The oxidized Ag^+ cations dissolve into the Ag_2S

and cause the shrink of Ag nanowire.[5] The control of Ag nanowire growth and shrink by STM is shown in Figure 1.1(b). The gap-type atomic switch was developed based on the controlling technique of nanowire mentioned above.[6][7] The Ag/Ag_2S/Pt atomic switch was fabricated by fixing the relative position of the Ag_2S tip and Pt electrode in one device. The growth of Ag nanowire under external bias results in the connection between Ag_2S tip with Pt electrode and the device change into the "ON" state. Under reverse bias, the nanowire will shrink and the device is turned off. Figure 1.2 shows the structure and *I-V* curve of the Ag/Ag_2S/Pt gap-type atomic switch.[2]

The gap-type atomic switch has been realized base on different electrolytes, such as Ag_2S[6–8], Cu_2S[9], CuI, $RbAg_4I_5$[10]. A theoretical model was established to explore the relation between switching time and switching bias of a Ag/Ag_2S/Pt atomic switch.[11]

$$t_{sw} = \frac{1}{C_1 P_d(V_{sw}) P_{up}(V_{sw})} \int_{z_{on}}^{z_{off}} \exp\left(\frac{E_a - C_2\sqrt{It}}{k_B T}\right) dZ \tag{1.1}$$

where $P_d(V_{SW})$ and $P_{up}(V_{SW})$ are probability parameters determined by the atomic diffusion on the Ag_2S surface and atomic diffusion over a step hopping in the precipitated Ag nanodot, respectively. The model indicates that the the diffusivity of participated metal atoms has great impact on the switch time of gap-type atomic switch. The crossbar circuits based on gap-type

atomic switch have been successfully fabricated. [12] In addition, some atomic switches with new functions, such as learning abilities, neuromorphic and synaptic operations, were developed based on the gap-type atomic switch.

Another type of atomic switch is gapless-type. Similar with the gap-type, the gapless-type also has sandwich structure, consist by active metal electrode (*e.g.* Cu and Ag), inert electrode (*e.g.* Pt) and ionic conductive layer (*e.g.* Ta_2O_5 and SiO_2). Its biggest difference with the gap-type atomic switch is that the electrolyte material is in contact with both electrodes in the gapless-type. In the gapless-type atomic switch, the conductive path was formed inside an ionic conductive layer.[13] The typical operation process of a gapless-type atomic switch in illustrated in Figure 1.3. The first step is "forming process", which is the first time turning-on process after the fabrication of device. In this step, the metal atom (such as Cu and Ag) dissolve in to the ionic conductive layer at the anode/electrolytes interface under a positive bias voltage. Then, under the electronic field, the dissolved metal ions diffuse in the direction of inert

electrode, and finally lead to the inhomogeneous nucleation of metal atom filament at the surface of the inert electrode. Then the metal filament grows until it forms a bridge between the two electrodes and turns on the device, and the device is turned on. The turn-off mechanism of gapless-type atomic switch is related to the joule-heating-assisted oxidation reaction. As the temperature rises due to the joule heating, the metal atoms located at the thinnest part of the conductive filament are oxidized, and the conductive path is disconnected. Due to the filament breaking taking place at the thinnest part of metallic filament, the turn-on operation after the "forming process" costs much shorter time. The gapless-type atomic switches have been fabricated with a variety of materials. The active metal electrode can be Cu or Ag, while the ionic conductor can be Ag_2S[14–16], Cu_2S[17,18], GeSe[19], Ta_2O_5[20], HfO_2[21], SiO_2[22], Al_2O_3, TiO_2[23], and ZnO[24]. The inert electrode can be Pt, W, Au and Mo.

The switch time of gapless-type atomic switch is related to the applied voltage, diffusion constant of cations in the ionic conductive materials, the reduction/oxidation activation energy and temperature.[25] Since the thickness of ionic conductive layer is usually longer than a few nanometers, the switching times depends on the cation diffusion constant.[26] The gapless-type atomic switch is the nonvolatile bipolar switch, which needs the bipolar bias voltages to writing and erasing. The gapless-type atomic switch can be used as the nonvolatile memories and reconfigurable switches in field programmable gate arrays. [27] A nonvolatile memory chip, which is based on the Cu_2S atomic switch, has been successfully fabricated. [27]

1.1.2 Ta_2O_5 atomic switch

The Cu/Ta_2O_5/Pt gapless-type atomic switch was firstly fabricated by T. Sakamoto et.al.[20] Due to its high threshold voltage and compatibility with the complementary metal-oxide-semiconductor (CMOS) techniques, it has attracted intensive research interests. In the fabrication process, the Pt electrode was firstly deposited by sputtering. Then hydrogen silsesquioxane, which works as the interlayer dielectric, was patterned on the Pt. The Ta_2O_5 film was fabricated on the electrode by pulsed laser deposition. Lastly, the Cu electrode was deposited. The thickness of Pt electrode and Ta_2O_5 film were 50 nm and 15 nm respectively. Due to the fabrication technique, the Ta_2O_5 was in an amorphous state. The *I-V* characteristic of the Ta_2O_5 atomic switch is shown in Figure 1.4. It can be seen that the current increases by more than five orders of magnitude at the voltage of 2.2 V. The switch mechanism, as we

mentioned, is related to the formation and annihilation of the Cu conductive filament.

Based on the Ta_2O_5 atomic switch, further investigations were conducted to understand the relation between properties of devices and its structure. First, to facilitate the application of atomic switch in logic devices, the turn-on voltage should be large enough. N. Banno *et al.* established the relation between Cu^+ ion diffusivity and the turn-on voltage based on both $Cu/Cu_2S/Pt$ and $Cu/Ta_2O_5/Pt$ switches.[26] They found that the turn-on voltage increases linearly when the Cu^+ ion flux (the product of Cu^+ diffusion coefficient and the Cu^+ concentration) increases exponentially.

Another interesting experiment was the examination of effect of moisture to the operational characteristics atomic switch. To this end, the $Cu/Ta_2O_5/Pt$ and $Cu/SiO_2/$ Pt cells are fabricated under different ambient water vapor pressure and temperature.[28] The main findings are: 1) the water molecular will be absorbed in the grain boundary and form a network of hydrogen bonds. The water molecular absorption will facilitate the metal ionic diffusion. 2) The Cu oxidation at the anode interface might occur via the reaction between Cu and H_2O ambient.

Very recently, the effect of electrolyte film density on the atomic switch operational characteristics was investigated based on the $Cu/Ta_2O_5/Pt$ cell.[29] The research shows that the structural properties of Ta_2O_5 film have great impact on the switch behavior of atomic switch. With the decrease of Ta_2O_5 film density, the redox current is increased and forming voltage is reduced. It is assumed that the decrease of forming voltage can be attribute to the enhace of Cu ionic diffusion in the low-density film.

In addition, the first-principles calculation was used to reveal the microscopy structural and switch mechanism of Cu/Ta_2O_5/Pt atomic switch [30–34]. B. Xiao *et al* revealed the structure of Cu metallic filament in the *a*-Ta_2O_5 cell. [30,34] The molecular dynamic simulation shows that the minimum diameter of Cu filament is about 0.24 nm. The Cu_2O layer will form at the interface of Cu and *a*-Ta_2O_5, The Cu^+ in the Cu_2O layer can be that main sources of the diffusive Cu ions in the Ta_2O_5 layer.[30,31]

1.2 All-solid-state battery

The all-solid-state battery is a kind of battery containing both the solid electrodes and the solid electrolyte. Common rechargeable batteries contain a liquid electrolyte, which leads to the low charge retention, limited operation temperature and risk of leakage. The solid-state battery works on the basis of the same working mechanism as other batteries, except that the liquid electrolyte is replaced with a solid electrolyte. An immediate benefit of using the solid electrolyte is that we can inherently avoid the risk of the liquid leakage and the consequent safety problem. Moreover, due to the omission of large separator in the liquid electrolyte, which is necessary for liquid cells, solid state batteries can achieve a much thinner thickness. Solid-state electrolytes have a typical thickness of approximately 1 μm, whereas the separator in liquid electrolyte-based cells typically has a thickness of 20 μm. For this reason, the solid-state battery has great potential in achieving larger energy density.

1.2.1 The structure of solid-state battery

The solid-state batteries are formed by two electrodes and an electrolyte layer in between.[35] The structure of a planar all-solid-state battery is shown in Figure 1.5. The battery usually is fabricated on a substrate. First, the active electrode is deposited on the top of the current collector. To ensure the high power capabilities of battery, the electrode materials should have good electronic and ionic conductivities and high charge density. Above the electrode, the solid-state electrolyte is deposited. The electrolyte layer should have high ionic conductivity and low electronic conductivity. At last the second electrode should be positioned.

It should be mentioned that the two electrodes (cathode and anode) should have a large equilibrium potential difference to guarantee a sufficient battery voltage.

Compared with the common batteries, the all-solid-state battery has several advantages due to the omission of liquid electrolyte. First, it fundamentally solved the safety problem caused by the leakage of organic solvent. Second, it has much longer cycle-life owing to the absence of liquid electrolyte, which is involved in the degradation of traditional batteries. The disadvantage of solid-state batteries is much lower ionic conductivity of the solid electrolyte compared with the liquid one. This low conductivity results in a higher voltage drop. So searching the solid electrolyte with high conductivity is a very important research topic in the field of all-solid-state battery.

1.2.2 Li_3PO_4 based electrolyte

As mention above, the biggest drawback of all-solid-state batteries is the low ionic conductivity of solid electrolyte. Thus, great effort has been made to discover the electrolyte materials with fast ionic diffusion. Different kinds of electrolytes have been proposed, such as $LiNbO_3$, Lithium Lanthanum Titanium Oxides, Polymer Electrolytes, etc. Among them, amorphous lithium phosphates are a popular class of electrolytes because of its high ionic conductivity, and chemical and physical stability. The pure bulk Li_3PO_4 has an ionic conductivity of about $3 \cdot 10^{-7}$ $S \cdot cm^{-1}$.[36] Many experiments found that better ionic conductivity can be achieved by creating mixed phosphates. Therefore, a variety of mixed phosphates

electrolytes that based on Li_3PO_4 based are proposed, such as $Li_2O{\cdot}P_2O_5{\cdot}SiO_2$, $Li_3PO_4{\cdot}Li_4PS_4$.

In the 1990s, the LiPON electrolyte material was developed at Oak Ridge National Laboratory. The LiPON is fabricated by sputter deposition of Li_3PO_4 thin films in the nitrogen atmosphere. [36,37] The LiPON has doubly and triply coordinated nitrogen atoms and bridging O atoms, which will form a crosslink network between the phosphates. The LiPON has a high conductivity of $3{\cdot}10^{-6}$ $S{\cdot}cm^{-1}$. LiPON has been most frequently used electrolyte in the all-solid-state batteries.

The Li_3PO_4 based electrolytes can be fabricated with sputter deposition[36,38], pulsed laser deposition[39], ion-beam assisted deposition [40,41] etc. These fabrication methods make the resultant materials have an amorphous structure.

1.3 Previous study on atomic diffusion in amorphous materials

Just like the atomic switch and all-solid-state battery, the working mechanisms of many recently-developed nano-scale information and energy devices are related to the atomic diffusion in the electrolyte. Because that the fabrication methods of these devices are usually sputtering or pulsed laser deposition, the electrolyte materials tend to exist in amorphous form. For this reason, to understand the microscope mechanism of the atomic diffusion behavior in amorphous materials is becoming increasingly important.

Atomistic simulation has played a significant and increasing role in the materials science. It has been a very powerful tool for the investigation of the microscope structure evolution. Thus, a lot of theoretical research was conducted to investigate the structural properties of the amorphous materials. The models of amorphous material were almost exclusively constructed with the melt quenching method (also called simulating annealing method). This method is based on the molecular dynamics, and its specific procedure is as follow. First, a crystal structure the model is melted with high-temperature (usually higher than melt point of material) molecular dynamics simulation, until liquid-like structure is achieved. Then, the material is gradually annealed to low temperature (typically 300 K). The resultant model can present amorphous state of the material. The melt quenching method have been used in a variety of

materials, and usually the amorphous model can reproduce the structure characteristic (such as pair correlation functions and structure factors) of the amorphous materials prepared experimentally. [42–45]

On the on the hand, relatively few research was conducted to simulate atomic diffusion in amorphous materials, due to the relative large computational cost. Here, we briefly introduce some atomic simulations about atomic diffusion in different amorphous materials and the simulation methods used in them. First, the lithium diffusion in amorphous silicon was investigated theoretically, because the kinetics of Li diffusion is an issue of central importance in the mechanical failure of amorphous Si (*a*-Si) electrodes.[46] The nudged elastic band together with first-principles calculations were used to study the diffusion pathways of Li inside a supercell contains 60 Si atoms. The diffusion pathways inside the *a*-Si model are shown in Figure 1.6. The Li diffusion pathways were found to have relatively low energy barriers (<0.50 eV). In addition, it was found that both the energy barriers for diffusion and the topology of the atomic structure control the diffusion behavior. For the same issue, the ab-initio molecular dynamics was performed to compute the Li diffusion coefficient in *a*-Si.[47] The supercell contains 120 atoms and molecular dynamics was performed for 15 ps. It was found that Li diffuses faster in amorphous than in crystalline Si. In addition, theoretical research was also performed to understand the performance of battery coating materials, amorphous Al_2O_3 and

AlF_3.[48] The *a*-Al_2O_3 and *a*-AlF_3 models contains 32 and 40 atoms, respectively. Form the two models, 307 and 356 Li diffusion paths are characterized with climbing images nudged elastic band method. Then the Li diffusivity was calculated with kinetic Monte Carlo simulation.

The simulation of atomic diffusion in amorphous needs more computational effort than crystal case. For example, the number diffusion pathways existed in an amorphous supercell (as shown in the Figure 5.1) is much more than a crystalline case. Such issue is one factor leading to the poor understanding of diffusion in amorphous. The previous research, to some level, provides insight into their respective materials. However, these research is not system for two reasons. First, because of the stochastic nature of amorphous materials, it is almost impossible to represent them by small structure models. A reliable theoretical study might need the use of large-scale model or the averaging over calculation results for many small models. Second, the difference of fabrication condition results in a very different structure of amorphous materials. The variation of density and composition of the amorphous materials certainly has great influence on the diffusion behaviors of the constituent atoms.

The most primary factor that hindered the systematic theoretical research of diffusion in amorphous material is that the high computational cost and slow simulation speed of first-principles calculation.

1.4 Application of neural network potentials

The high-dimensional neural network (NN) potential was proposed by J. Behler and coworkers. It has attracted much attention as a promising way of achieving high computational accuracy and speed [1]. The basic idea of high-dimensional NN potential is to represent the total energy E of the system as a sum of atomic contribution E_i. The contribution of each atom is predicted using an NN according to its local atomic environment. The atomic environment is described with the atom-centered symmetry function. The high-dimensional NN potential can be trained with gradient based optimization algorithm using a large amount of DFT calculations result as reference data. The details about how to construct a high-dimensional NN potential will be elaborated in Chapter 2.

Table 1.1: List of neural network potentials in the previous research

Materials	Number of Parameters	RMSE of Energy (meV/atom)		RMSE of Force (eV/Å)		Database size	Ref.
		Training	Test	Training	Test		
Si	-	4 ~ 5	5 ~ 6	0.2	0.2	~10,000	[49]
Cu	2521	3.6	3.9	0.081	0.079	37,763	[52]
C	1901	4.0	4.9	-	-	~60,000	[26]
Na	-	0.72	0.91	-	-	~17,000	[133]
ZnO	-	3.5	3.9	0.03	0.03	38,750	[53]
GeTe	7,281	5.01	5.60	0.46	0.47	30,000	[91]
CuZnO	8,553	5.8	6.1	0.18	0.17	100,000	[56]

The previous studies shows that high-dimensional NN potentials are much more accurate than conventional interatomic potentials while the computation speed is usually several orders of magnitude faster than DFT calculations, and thus were utilized for simulating various material, such as Si,[49] C,[50,51] Cu,[52] ZnO,[53] TiO_2,[54] H_2O dimers,[55] Cu clusters supported on Zn oxide,[56] and Au/Cu nanoparticles with water molecular.[57] The detailed information of several constructed NN potentials has been listed in Table 1.1. As we can see from the table, all NN potentials provide very precision energy and atomic forces. Since the NN potential omits the electronic calculation, the calculation speed is several orders of magnitude faster than DFT.

Owning to the accuracy and computational efficiency of the high-dimensional NN potential, it has been used to address several key issues in the materials science that beyond the reach of DFT. For example, an ab-initio quality NN potential was constructed for carbon, to carry out a large-scale study of the graphite-to-diamond transition.[50] The simulation was performed with a 100×100×100 Å supercell contains 145152 carbon atoms. Another example of the application of NN potential is the study of fast crystallization of the phase change materials GeTe.[58] In this study, a large-scale molecular dynamic simulation was performed with the NN potential. The simulation cell contains 4096 atoms, and the simulation time is 2-

4 ns. Very recently, the high-dimensional NN potential was used to study the self-diffusion of surface defects on low-index copper surface in the water environment.[59]. The simulation supercell contains approximately 2000 atoms. Molecular dynamic simulation was performed for 1 ns to study the diffusion properties of surface defects at different copper surfaces.

1.5 Objective of the present work

As mentioned in Section 1.3, many theoretical studies were conducted to simulate atomic diffusion behaviors in amorphous materials. However, these research is not enough for the complete understanding for this issue. First, the diffusion behavior are all comes from the calculation result of one amorphous model in the previous study. However, whether all the structural characteristic of amorphous materials can be represented by only one model is still unclear. Thus, it is more accurate to get the reliable results from the large-scale amorphous model or several small-scale models. Second, the amorphous materials inevitably subject to the density and composition variation depending on the fabrication conditions. However, no previous research considered such issue in their simulation.

In principle, we can consider all these factors by performing a vast number of computation with first-principles method. However, due high computational cost and slow simulation speed of first-principles calculation, to perform a systematical simulation of atomic diffusion must need a huge computational resource. Therefore, to tickle this problem, a reliable and more efficient simulation method is needed.

In this study, we try to establish computational approaches that can accurately and efficiently predict the atomic diffusion behavior in the amorphous materials. These approaches are based on the combination of first-principle calculation and the machine learning techniques. The dissertation is organized as following: Chapter 2 provides the computational methodology used in this study. The computational approaches for the atomic diffusion, including molecular dynamics, nudged elastic band and kinetic Monte Carlo, will be described. In addition, the emerging simulation technique, machine-learning interatomic potential, will be introduced. In Chapter 3, we proposed a simple neural-network-based interatomic potential, which is named simplified neural network potential. We demonstrated that the new method is capable of

accurately predicting the diffusion paths and barrier energies of Cu diffusion in amorphous Ta_2O_5. In Chapter 4, we adopted the high-dimensional neural network potential, which is proposed by J. Behler, to study the Li diffusion behavior in amorphous Li_3PO_4. All the calculation results, including the diffusion coefficient, diffusion pathways, and activation energy are carefully compared with the results of the first-principles simulations. In addition, the neural network potential is used to construct a large-scale amorphous Li_3PO_4 structure. Based on the neural network potential methods that we validated in Chapters 3 and 4, we systematically investigate the Cu diffusion behavior in the amorphous Al_2O_3, with considering a large density and composition variance of amorphous matrix, in Chapter 5. Finally, a summary of our study is given in Chapter 6.

Chapter 2

Methodology

In this chapter, the computational approaches used in this work are introduced. First, the frequently used atomic simulation methods for the atomic diffusion, such as nudged elastic band method, kinetic Monte Carlo simulation and molecular dynamics, are described in detail. Then, we explain the potential energy surface, which is the foundation of atomic simulation. The two types of potential energy surface, *i.e. ab-initio* and empirical interatomic potentials, are elaborated. Lastly, we introduce a recently developed computation method, *i.e.* the machine-learning interatomic potential. The machine-learning interatomic potential represents potential energy surfaces by fitting large data sets of *ab-initio* calculation results with machine-learning techniques. In this part, we focus on the high-dimensional neural network potential, since it is used in the present study described in the following chapters.

In the dissertation, the Vienna *ab initio* simulation package (VASP) [60,61] was utilized to perform all the required *ab-initio* calculations, including energy calculation, nudged elastic band calculation and *ab-initio* molecular dynamic. On the other hand, all the calculations that based on neural network potential is performed with the code developed by ourselves. The nudged elastic band and molecular dynamics methods are also implemented in the code.

2.1 Computational approaches for atomic diffusion

In this part, we survey the available computational methods for studying atomic diffusion in solid bulk materials. The molecular dynamics, nudged elastic band and kinetic Monte Carlo

methods are introduced, as well as the *pros and cons* of each method in studying atomic diffusion.

2.1.1 Molecular dynamics method

Molecular dynamics is an atomic simulation approach. By simulating the motion of molecules and atoms in a certain period of time, the physical properties of the material can be obtained. Usually, the molecular and atomic trajectories are obtained by numerically solving the Newton equations of motion.

2.1.1.1 Molecular dynamics algorithm

In the MD simulation, it is assumed that all atoms and molecules obey the laws of classical mechanics. Then the equation of motion is numerically solved to get the trajectory of each atom. The statistical method is used to calculate the macroscopic physical quantity of the system.

The basic algorithm of MD simulation is shown in Figure 2.1. Firstly, the initial configuration, which is usually a structure derived from the experimental data or quantum

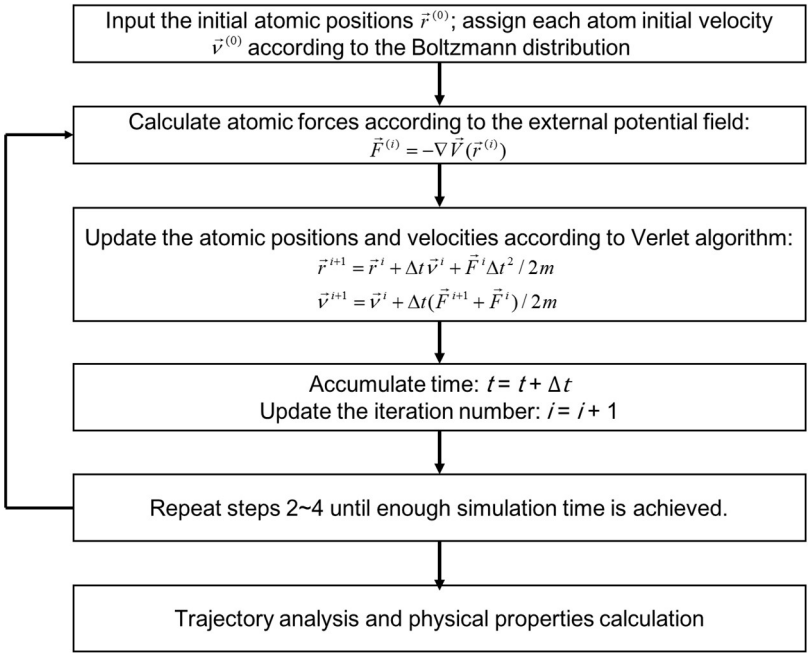

Figure 2.1: Illustration of molecular dynamics simulation based on the Verlet algorithm.

chemistry calculation, is given. After that, each atom is assigned with an initial velocity $v^{(0)}$, which is generated according to the Boltzmann distribution. Then, the evolution of atomic positions are obtained by solving the classical equation of motion

$$m\frac{\partial^2 r}{\partial t^2} = F. \tag{2.1}$$

Many algorithms can be used to perform the step-by-step numerical integration of the equation. The Verlet algorithm [62] is the most popular way, in which the atomic coordinates and velocity at the time $t+\Delta t$ can be evaluated according to:

$$\vec{r}^{\,i+1} = \vec{r}^{\,i} + \Delta t\vec{v}^{\,i} + \vec{F}^{i}\Delta t^2 / 2m, \tag{2.2}$$

and,

$$\vec{v}^{\,i+1} = \vec{v}^{\,i} + \Delta t(\vec{F}^{\,i+1} + \vec{F}^{\,i}) / 2m. \tag{2.3}$$

After a long enough simulation time, the macroscopic physical properties can be calculated. The actual calculations of the macroscopic physical quantities are often carried out in the final stage of the simulation.

The determination of the force acting on each nucleus is the most crucial part of molecular dynamics. The potential energy surface, also known as the force field, provides the atomic force information for the MD simulation.[63] The potential energy surface is obtained either by the on-the-fly quantum mechanics calculation (*i.e.* ab-initio MD) or by empirical interatomic potential (i.e. classical MD). Detailed information about potential energy surface will be elaborated in Section 2.2.

2.1.1.2 Diffusion coefficient

The diffusion coefficient of an atom can be estimated by analyzing the mean square displacement (MSD) along the trajectory of molecular dynamics. The MSD is defined as:

$$msd(\Delta t) = \left\langle \left(r_i(t_0 + \Delta t) - r_i(t_0)\right)^2 \right\rangle, \tag{2.4}$$

where $r_i(t_0)$ and $r_i(t_0+\Delta t)$ represent the position of particles i at origin time t_0 and $t_0+\Delta t$, respectively, and the angle bracket denotes averaging. The MSD is a measure of the atomic

displacement during a short time interval Δt. It should be mentioned MSD only looking at relative times rather than absolute time, which means any step of MD trajectory can be regard as the original time t_0. In solids, liquids and gases, the trajectory of an atom under thermal motion has quite complex shape in space, due to the collisions with other atoms. The atom motion resembles a random walk. In such case, the MSD of particles will increase linearly with time. Thus, it is possible to investigate the behavior of diffusion by looking at the slope of MSD. Such relation is defined by the Einstein equation:

$$D = \frac{1}{6} \lim_{\Delta t \to \infty} \frac{\left\langle \left(r_i(t_0 + \Delta t) - r_i(t_0) \right)^2 \right\rangle}{\Delta t}. \tag{2.5}$$

where D indicats the diffusion coefficient, which also known as diffusivity.

2.1.1.3 Diffusion activation energy

Another key property of atomic diffusion, the diffusion activation energy, can also be evaluated from the MD simulation. In doing so, the atomic diffusion coefficients at various temperatures should be calculated with the Einstein equation (Equation 2.5). In general, the temperature dependence of atomic diffusion coefficient obeys the Van't Hoff equation or the Arrhenius Law:

$$D = D_0 \exp\left(-\frac{E_a}{kT} \right). \tag{2.6}$$

where E_a is the diffusion activation energy, D_0 is the pre-exponential factor, k is Boltzmann constant and T is temperature (in Kalvin). This equation can be rewritten as:

$$\log(D) = \log(D_0) - \frac{E_a}{\ln(10)k} \left(\frac{1}{T} \right). \tag{2.7}$$

Therefore, the activation energy E_a and prefactor D_0 can be obtained by linear fitting of the plot of $\log(D)$ against $(1/T)$.

2.1.1.4 Pros and cons of molecular dynamics

The MD simulation can provide unique insight into the atomic diffusion mechanism. The

MD simulation does not require prior knowledge of the materials which makes it suitable for the investigation of new materials. Various diffusion properties, such as the diffusion coefficient, activation energy, diffusion pathways, can be directly obtained from the MD simulation.

The limitation of MD is mainly the short simulation time. Due to the small time step (usually 1fs/step) used in the MD, the total time span of a molecular dynamic trajectory is usually limited in picoseconds or nanoseconds. Therefore, the MD is mainly used for the materials with fast diffusivities. Moreover, in many cases, MD have to be performed at elevated temperatures to get a faster diffusion speed and then the diffusion coefficients are extrapolated to the temperature range where we are interested. However, such extrapolation is also based on the assumption that the diffusion mechanism is the same at any temperature ranges. In another word, the temperature dependence of diffusion coefficients perfectly obeys the Arrhenius relation and the material has invariable activation energy.

2.1.2 Nudged elastic band method

In many solid materials, the atomic diffusion process can be regarded as atom hopping among many well-defined equilibrium sites via an activated states located at the saddle point of the diffusion pathways. The nudged elastic band (NEB) method is capable of searching the diffusion pathway between two equilibrium sites and estimating the activation energy of such atomic hopping.[64,65]

2.1.2.1 Computation algorithm

The nudged elastic band method was developed from the chain-of-states method, which is also devised to search the minimum energy path between two equilibrium sites.[66] In the NEB method, we begin with the geometry optimization of the initial and final equilibrium structures. Then, a serial of images of the system was interpolated between the initial and final structures. The atoms in the interpolated image structures feel the force from both the external force field $-\vec{\nabla} V(\vec{r}_i)$ and imaginary spring force F_i^s. In the NEB method, the force acting on image *i* is defined as:

$$\vec{F}_i = -\vec{\nabla}V(\vec{r}_i) + \vec{\nabla}V(\vec{r}_i)\cdot\hat{r}_{\parallel}\hat{r}_{\parallel} + F_i^s \cdot \hat{r}_{\parallel}\hat{r}_{\parallel}, \tag{2.8}$$

where:

$$F_i^s = k_{i+1}(\vec{R}_{i+1} - \vec{R}_i) - k_i(\vec{R}_i - \vec{R}_{i-1}). \tag{2.9}$$

The $\hat{r}_{\parallel}$ is the unit tangent to the diffusion pathway. Thus the first two terms of Equation 2.8 $-\vec{\nabla}V(\vec{r}_i) + \vec{\nabla}V(\vec{r}_i)\cdot\hat{r}_{\parallel}\hat{r}_{\parallel}$ represent the perpendicular component of external potential force and the last term $F_i^s \cdot \hat{r}_{\parallel}\hat{r}_{\parallel}$ represents the parallel component of spring force. Such projection of force was referred as "nudging". The optimization of the images according to Equation 2.8 ensures the convergence to the minimum energy paths and can maintain equal spacing between neighboring images.

The schematic of NEB calculation is shown in Figure 2.2. The energy profile along the diffusion path can also be plotted, from which barrier energy of atomic hopping can be computed. The barrier energy E_a is given by:

$$E_a = E_{\max} - E_{initial}\ , \tag{2.10}$$

where E_{max} is the maximum energy along the minimum energy path, and $E_{initial}$ is the energy of the initial structure. Performing NEB calculation also requires an accurate description of external force field, *i.e.* the potential energy surface. In most cases, the external atomic forces are provided by the first-principles calculation, though occasionally the empirical interatomic potentials can also be used.

2.1.2.2 Pros and cons of NEB

The NEB method has many merits including 1) the guarantee to find a continuous minimum energy path between the given initial and final states; 2) a discrete representation of diffusion path with fine resolution (if used with enough number of images); 3) relatively light computation compare to the MD calculation, and 4) easy parallelization of the algorithm in the practice use.[66]

However, the application of NEB method is limited to the cases of dilute limits, that is, hopping of a single atom or a single vacancy in the host structure. The identification of concerted motions of multiple atoms, which often appear during atomic diffusion, is still very challenging for the NEB method. In addition, the NEB method is difficult to apply to the high-disordered system, such as amorphous materials, due to the existence of massive inequivalent diffusion pathways. Even if all the diffusion pathways in an amorphous structure are characterized with NEB, to obtain the actual diffusion behavior still requires other simulation approaches, such as the kinetic Monte Carlo method.[67]

2.1.3 Kinetic Monte Carlo method

Kinetic Monte Carlo simulation (KMC) is a very powerful tool for simulations of dynamics, because of its highly adaptive and simple procedure.[67] For studies of atomic diffusion, it requires the input information of all the atomic diffusion pathways and corresponding barrier energies, which are usually computed with NEB method.

Same as the molecular dynamics, the KMC provides the time-evolution trajectory of materials system. In the case of MD, however, as mentioned in Section 2.1.1.4, the small time step limits the application of MD to the long time-scale simulation. Even with an acceleration algorithm, such as hyperdynamics, the simulation time of MD can be extended to at most several ms.

As illustrated in Figure 2.3, the diffusion particles spend most of the time at a well-defined equilibrium site, *i.e.* the bottom of a potential well, and only a small fraction of the time at the diffusion pathways in an MD trajectory of atomic diffusion. In the KMC simulation, we change our focus from the "trajectory of atomic movement" to the "evolution of system", then the simulation time-scale will span from the atomic vibration scale to the system transition scale. The extension of the time-scale is achieved by the discard of the small vibration which has nothing to do with how the system crosses through the energy barrier. The KMC simulation assumes that the atomic diffusion process in the solid materials is a typical Markov process, in which the future evolution of a system is solely based on its present state and has nothing to do with the history.

2.1.3.1 Transient state theory

The most vital process of KMC is to calculate the transition rate, which determines the accuracy of the simulation results. In general, the transition state theory (TST) is used to calculate the transition rate. In the TST, the transition rate of the system depends on the behavior of the system at the saddle point, while the influence of the state of the equilibrium (potential well) can be neglected. If a large number of identical systems form a canonical ensemble, the flow of the system across a vertical section perpendicular to the transition path

i-j in a unit of time is k_{ij}. In the TST, the transition rate from *i* to *j* can be obtained as[68]:

$$k_{ij} = \frac{1}{2}\left(\frac{2k_bT}{\pi m}\right)^{1/2}\left\langle \delta\left[f\left(\vec{R}\right)\right]\nabla f\right\rangle_i, \tag{2.11}$$

where $f(\mathbf{R})$ is the plane equation of the perpendicular section. However, in practical calculations, k_{ij} is frequently obtained according to the harmonic transition state theory (hTST)**:**

$$k_{ij} = \frac{\prod_{i=0}^{3N}\nu_{ij}^{0}}{\prod_{i=0}^{3N-1}\nu_{ij}^{sad}}\exp\left(-\frac{\Delta E_{ij}}{k_BT}\right). \tag{2.12}$$

The first term of Equation 2.12 requires the phonon calculations for the two systems where the diffusion particle is located at the initial position and the saddle point, respectively. The phonon calculation can be performed by Hessian matrix diagonalization or density functional perturbation method (DFPT), and E_{ij} is the energy barrier of the pathway *i-j*, which can be obtained by NEB. Therefore, Equation 2.12 guarantees that the k_{ij} can be analytically solved by using an atomistic simulation (MD or DFT). However, the calculation of phonon spectra at the saddle point should be calculated for each transition process, which greatly increases the amount of calculation. So the prefactor is often set as a constant value:

$$k_{ij} = \nu'\exp\left(-\frac{\Delta E_{ij}}{k_BT}\right) \tag{2.13}$$

where the typical value for *v'* is 10^{13} Hz.

2.1.3.2 Outline of KMC algorithm

There are many ways to implement the KMC method. In this section, we only introduce the direct method, which is the most commonly used algorithm with high efficiency. In each step, two random numbers r_1 and r_2 are generated following the uniform distribution in the range (0,1]. The r_1 is used to select the transition path, r_2 determines the time interval of system staying in one state. To be more specific, we assume that the system is in the state of *i*, and then the transition event *k* is chosen if the $\frac{1}{k_{total}}\sum_{j=1}^{k-1}k_{i,j} < r_1 < \frac{1}{k_{total}}\sum_{j=1}^{k}k_{i,j}$, in which k_{total} is the sum of

k_{ij} for all possible transition events. Then the system time proceeds for $\delta t = -\frac{1}{k_{total}}\ln(r_{ik})$. The algorithm is summarized as follows:

1) Calculate the total transition rate of state i, $k_{total} = \sum_j k_{i,j}$;
2) Generate random number r_1;
3) Determine the transition event k that satisfies the condition: $\frac{1}{k_{total}}\sum_{j=1}^{k-1} k_{i,j} < r_1 < \frac{1}{k_{total}}\sum_{j=1}^{k} k_{i,j}$;
4) The system is changed to state k, while the time of simulation is increased by $\delta t = -\frac{1}{k_{total}}\ln(r_2)$.
5) Repeat the procedure from step 1.

It should mention that the residual time of a KMC event is calculated as $\delta t = 1/k_{total}$ in some of the previous KMC studies, but the simulation results are basically the same.

Similar to the molecular dynamics, various atomic diffusion properties can be extracted from the state-to-state trajectory generated by KMC simulation. The diffusion coefficients of particles as well as the diffusion activation energies can be calculated with the method introduced in Section 2.1.1.2 and Section 2.1.1.3.

2.1.3.3 Application of KMC

The superiority of KMC is obvious: it expands the simulation time span for several orders of magnitude and enables the study of atomic diffusion at a relatively lower temperature than MD. In addition, if we know these rate constants exactly, the state-to-state trajectory will be indistinguishable from a (much more expensive) trajectory generated from a full molecular dynamics simulation.

However, the KMC simulation requires that every escape pathway for every state (that will be encountered in the dynamics simulation) should be accurately characterized. However, the real dynamical evolution of a system will often surprise us with unexpected and complex reaction pathways. Because these pathways (before we have seen them) are outside our intuition, they will typically not be included in the rate catalog, and hence cannot occur during

the KMC simulation. In such a case, KMC would give a seriously flawed description of the diffusion dynamics.

2.2 Potential energy surface

Potential energy surface is the direct function of atomic configurations and potential energies. For dynamic simulation, like MD, the energies and forces for a large number of configurations should be provided from the potential energy surface. So, the potential energy surface is the foundation for performing the simulation introduced in the proceeding section. The potential energy surface is constructed by either quantum mechanical methods, *i.e. ab-initio* methods, or by molecular mechanics with empirical interatomic potentials. Both methods will be introduced in the following text.

2.2.1 Ab-initio method

2.2.1.1 Many-body Schrödinger Equation

In the first-principles calculation, the state of system is determined by solving the time-independent many-body Schrödinger equation:

$$\left(-\sum_{i=1}^{N} \frac{1}{2} \nabla_i^2 - \sum_{A=1}^{M} \frac{1}{M_A} \nabla_A^2 - \sum_{i=1}^{N} \sum_{A=1}^{M} \frac{Z_A}{r_{iA}} + \sum_{i=1}^{N} \sum_{j>i}^{N} \frac{1}{r_{ij}} + \sum_{A=1}^{M} \sum_{B>A}^{M} \frac{Z_A Z_B}{R_{AB}} \right) \Psi_s = E_s \Psi_s , \qquad (2.14)$$

where i and j represent electrons, and A and B represent nuclei. r_{iA}, r_{ij} and R_{AB} represent the distance between electron i and nuclei A, election i and electron j, nuclei A and nuclei B, respectively. M_A and Z_A are the atomic mass and atomic number of element A. However, Equation 2.14 is so complex that solving it for only a few atoms is impossible even today. Thus, several approximations should be introduced to solve the many-body Schrödinger equation.

Born-Oppenheimer approximation, which assumes that the motion of nuclei and electrons can be treated separately, was firstly introduced to simplify Equation 2.14. It is based on the large difference of the nuclear and electronic masses: Then the electrons can be expected to be

in instantaneous equilibrium with the much heavier nuclei. Under this approximation, time-independent many-body Schrödinger equation can be rewritten as:

$$\left(-\sum_{i=1}^{N}\frac{1}{2}\nabla_i^2-\sum_{i=1}^{N}V_{ext}(r_i)+\sum_{i=1}^{N}\sum_{j>i}^{N}\frac{1}{r_{ij}}\right)\Psi_s=E_s\Psi_s, \tag{2.15}$$

where V_{ext} represents the external field created by the nuclei, *i.e.* $V_{ext}(r_i)=-\sum_{A=1}^{M}\frac{Z_A}{r_{iA}}$.

2.2.1.2 Density functional theory

By applying the Born-Oppenheimer approximation, 3*M* nuclear degrees of freedom are removed from the many-body Schrodinger equation. However, the 3*N* electronic degrees of freedom left in Equation 2.15 make it still very difficult to solve. The density functional theory provides a method to systematically map the many-body problem to the single-body problem with only 3 degrees of freedom.

The density functional theory is based on the two theorems proposed by Hohenberg and Kohn.[69,70] The first Hohenberg-Kohn theorem proves the existence of one-to-one mapping between the external potential $V_{ext}(\boldsymbol{r})$ and the electronic density $\rho_0(\boldsymbol{r})$ at the ground state. In another word, once the ground state electronic density $\rho_0(\boldsymbol{r})$ is given, the external potential $V_{ext}(\boldsymbol{r})$, as well as the Hamiltonian, is uniquely determined. The second Hohenberg-Kohn theorem proves that for any external field $V_{ext}(\boldsymbol{r})$, the total energy $E[\rho(\boldsymbol{r})]$ can be regard as the functional of electronic density $\rho(\boldsymbol{r})$, and for a specific external field, the electronic density $\rho(\boldsymbol{r})$ which minimizes the total energy is the ground state density $\rho_0(\boldsymbol{r})$.

The Hohenberg-Kohn theorems demonstrate that a many-body electronic system can be treated as a functional of the ground state electronic density $\rho_0(\boldsymbol{r})$. However, the exact form of total energy functional $E[\rho(\boldsymbol{r})]$ is not provided. So physical sound and reliable approximations are indispensable. However, to find a reasonable approximation of the energy functional is difficult, especially for the kinetic term. To circumvent this problem, Kohn and Sham replace the many-body system as a set of independent and non-interacting particles. The Kohn-Sham equation[69] can be expressed as:

$$\left(-\frac{1}{2}\nabla^2 + V_H(r) + V_{ext}(r) + V_{xc}(r)\right)\psi_i(r) = \xi_i\psi_i(r), \tag{2.16}$$

$$\sum_i \psi_i(r)\psi_i^*(r) = \rho(r), \tag{2.17}$$

where the term $V_H(r)$ is the Hartree potential describing the Coulomb interaction energy of an electron in the average field generated by all other electrons:

$$V_H(r) = \int d^3r' \frac{\rho(r')}{|r-r'|}. \tag{2.18}$$

The term $V_{ext}(r)$ is the external potential which is generated from the nuclei-electron interaction. The term $V_{xc}(r)$ is the exchange-correlation potential which contains all the interactions that are not considered in $V_H(r)$ and $V_{ext}(r)$. The exact form of $V_{xc}(r)$ is still unknown but several reliable approximations have been devised.

The Kohn-Sham equation enables us to obtain the ground state information by solving a set of single-particle equations (Equation 2.15) with three degrees of freedom each. The electron density $\rho(\boldsymbol{r})$ can be obtained using the single-particle wavefunctions $\psi_i(r)$ according to Equation 2.17. It should be pointed out that $\rho(\boldsymbol{r})$ appears in $V_H(r)$, thus Equation 2.16 and 2.17 should be solved self-consistently. Once the ground state density $\rho_0(\boldsymbol{r})$ and single-particle wavefunctions $\psi_i(r)$ are obtained from the self-consistent calculation, the total energy of the system can be expressed as:

$$\begin{aligned} E[\rho(r)] &= -\frac{1}{2}\langle\psi_i(r)|\nabla|\psi_i(r)\rangle + \int d^3r V_{ext}(r)\rho(r) + \frac{1}{2}\int d^3r \int d^3r' \frac{\rho(r)\rho(r')}{|r-r'|} + E_{xc}[\rho(r)] \\ &= \sum_i \varepsilon_i - \frac{1}{2}\int d^3r \int d^3r' \frac{\rho(r)\rho(r')}{|r-r'|} + E_{xc}[\rho(r)] - \int d^3r V_{xc}(r)\rho(r). \end{aligned} \tag{2.19}$$

where $E_{xc}[\rho(r)]$ is related with the exchange-correlation potential $V_{xc}(r)$ by the equation:

$$V_{xc}(r) = \frac{\delta E_{xc}[\rho(r)]}{\delta\rho(r)}. \tag{2.20}$$

2.2.1.3 Exchange and correlation functions

The previous section outlined the formalism of DFT, which is an exact theory if the exact

XC functional is known. Unfortunately, the exact form of XC function is unknown, so we need reasonable approximations. A simple way is to assume exchange correlation potential at the position ***r*** depending only on the electron density value at ***r*** and not on its derivates, then the relation between exchange-correlation energy density $\epsilon_{xc}[\rho(r)]$ and $E_{xc}[\rho(r)]$ can be express as[69,70]:

$$E_{xc}[\rho(r)] = \int \varepsilon_{xc}[\rho(r)]\rho(r)d^3r. \tag{2.21}$$

Such approximation is called local density approximation (LDA). The LDA is exact for a homogenous gas, and works well in the system where the charge density does not vary too rapidly.

The several ways to improve LDA have been proposed, and the most obvious way is generalized gradient approximation (GGA), which express the exchange-correlation energy as functional of both electron density and its gradient.[71] The GGA exchange-correlation energy is expressed as:

$$E_{xc}[\rho(r)] = \int d^3r\rho(r)\varepsilon_{xc}[\rho(r)]F_x(s). \tag{2.22}$$

where $F_x(s)$ is a dimensionless function that includes the gradient of density. Various forms of $F_x(s)$ have been proposed, such as Perdew-Wang (PW91) [72] and Perdew-Burke-Enzerhof (PBE) [73].

2.2.1.4 Bloch theorem

The number of atom that is consisted in solid materials is about 10^{23}, which makes the explicitly consideration of each particle impossible. However, the Bloch theorem can simplified such problem under periodic boundary condition. In the Bloch theorem, the one-electron wavefunctions under a periodical boundary condition can be expressed as:

$$\psi_i(r) = u_{i,k}(r)e^{ik\cdot r}, \tag{2.23}$$

$$u_{i,k}(r) = u_{i,k}(r+R), \tag{2.24}$$

where $u(\boldsymbol{r})$ is a periodic function with the same periodicity as the periodical potential, ***k*** is a vector in the reciprocal lattice. The range of ***k*** vector is usually limited in first Bollouin zone,

which is the Winger-Seitz cell of the reciprocal lattice $\boldsymbol{G}$ defined by $\boldsymbol{G}\cdot\boldsymbol{R} = 2\pi N$, where N is arbitrary integer. The periodical part of Bloch wavefunctions $u(\boldsymbol{r})$ can be solved independently for each $\boldsymbol{k}$ vector, according to:

$$\left[-\frac{1}{2}(\nabla + ik)^2 + V(r)\right]u_{i,k}(r) = \varepsilon_{i,k}u_{i,k}(r). \tag{2.25}$$

The Bloch theorem transfer the calculation of wavefunction of infinite number of electrons to the calculation of finite number of electrons at infinite number of $\boldsymbol{k}$ points which are limited inside the first Bollouin zone. In addition, election wavefunction over a small region can be represented by a single $\boldsymbol{k}$ point. The properties, such as total energy, number of elections, of solid materials can expressed as the summation of $\boldsymbol{k}$.

$$f_i = \frac{1}{N_k}\sum_k f_i(k), \tag{2.26}$$

where N_k is the number of K points used in the calculation. The discrete set of k points can be automatically generate by Monkhost-Pack Scheme [74]. The error cause by using discrete $\boldsymbol{k}$ point mesh can be reduce by using denser sets of $\boldsymbol{k}$ points.

2.2.1.5 Plane wave

In practical calculation, the periodical function $u(\boldsymbol{r})$ in Equation 2.23 can be written as a sum of plane wave:

$$u_i(r) = \frac{1}{\Omega^{1/2}}\sum_G c_{i,G}e^{iG\cdot r}. \tag{2.27}$$

Combine the Equation 2.23 and 2.27, the electronic wavefunction can be rewritten as :

$$\psi_{i,k}(r) = \frac{1}{\Omega^{1/2}}\sum_G c_{i,G}e^{i(G+k)\cdot r}. \tag{2.28}$$

The plane wave set are complete and orthonormal. The coefficient c can be solved with Iterative diagonalization and minimization method. However, a large number of plane wave set functions should be used to expand the electronic wavefunctions. Usually, the plane waves with small kinetic energy $|\boldsymbol{k}+\boldsymbol{G}|^2$ is more important than those with large kinetic energies. For this

reason, we set a truncate criterion that the plane waves with kinetic energies lower than certain value (the cutoff energy) are used.

$$\frac{1}{2}|G+k|^2 < E_{cutoff}. \tag{2.29}$$

In principle, the cutoff energy should be tested to guarantee the convergence of total energy.

2.2.1.5 Pseudopotentials and Projector-Augmented-Wave method

The core electrons do not have contribution to the physical properties of materials. However, a large number of plane waves are needed to describe the core electrons due to the rapid oscillation of potential and wavefunctions near the nuclei. Thus, pseudopotential is introduced to achieve better computational efficiency. The pseudopotential replaces the all-electron potential by an effective potential that only acting on the valence electrons. By using the pseudopotential, the number of plane waves and number of electrons are reduced. There are several types of pseudopotential have been proposed, including norm-conserving pseudopotentials, ultra-soft pseudopotentials and the Projector-Augmented-Wave (PAW) method.

The PAW method can keeps all the information of core electrons. In PAW method, a set of smooth partial wavefunctions $\tilde{\phi}_i$ are related with all electron wavefunctions ϕ_i with a linear transformation *T*. The smooth wavefunctions and all electron wavefunctions are matched outside the core region. The smooth wavefunction can be expressed with Dirac notion as:

$$|\tilde{\phi}\rangle = \sum_i c_i |\tilde{\phi}_i\rangle, \tag{2.30}$$

and all electron wavefunctions are expressed as:

$$|\phi\rangle = \sum_i c_i |\phi_i\rangle. \tag{2.31}$$

The smooth wavefunctions $\tilde{\phi}_i$ are related with all electron wavefunctions ϕ_i with a linear transformation ***T***:

$$|\phi\rangle = T|\tilde{\phi}\rangle = |\tilde{\phi}\rangle + \sum_i c_i \left(|\phi_i\rangle - |\tilde{\phi}_i\rangle\right) \tag{2.32}$$

To make sure the transformation $\boldsymbol{T}$ is linear, the coefficient c_i must satisfy:

$$c_i = \left\langle \tilde{p}_i \middle| \tilde{\phi} \right\rangle, \tag{2.33}$$

where p is the projection operator. The transformation can be express as:

$$T = 1 + \sum_i \left(\left| \phi_i \right\rangle - \left| \tilde{\phi}_i \right\rangle \right) \left\langle \tilde{p}_i \right|. \tag{2.34}$$

There are several possible choices of the projection operator. Compare with other pseudopotentials, the PAW method can conserve the information of all-electron wavefunctions. For this reason, it is widely used in the electronic structure calculation. For any operator A that used for the all electron wavefunctions, we can defined a modified operator $\tilde{A}$ that can be used for the smooth wavefunction, by:

$$\tilde{A} = T^+ A T. \tag{2.35}$$

2.2.1.6 Atomic Force in DFT

DFT provide an accurate and efficient way to determine the ground state energy of a structure. To perform dynamics simulation base on the DFT, such as ab-initio molecular dynamics, the atomic forces should be determined. The atomic forces can be calculated in DFT according to:

$$\begin{aligned} \vec{F}_I &= -\nabla_{\vec{R}_I} \left[\min_{\{\psi_i\}} E\left[\{\psi_i\}, \vec{R}\right] \right] \\ &= -\frac{\partial E}{\partial \vec{R}_I} + \sum_{i,j} \Lambda_{i,j} \frac{\partial}{\partial \vec{R}} \left\langle \psi_i \middle| \psi_j \right\rangle - 2 \sum_i \frac{\partial \left\langle \psi_i \right|}{\partial R_I} \left[\frac{\delta E}{\delta \left\langle \psi_i \right|} - \sum_j \Lambda_{i,j} \left| \psi_j \right\rangle \right]. \end{aligned} \tag{2.36}$$

The first term is called Hellmann-Feynman force.[75] The second term is Pulay force, due to the holonomic orthonormality constraint.[76] The last term is referred as non-self-consistent force.[77]

2.2.2 Empirical interatomic potentials

The empirical interatomic potentials use simple mathematical functions to describe the

relation between the potential energy of a system with N atoms and the coordinates of atoms. The empirical interatomic potentials have the formula of:

$$V_{tot} = V(\vec{r}_1, \vec{r}_2, \vec{r}_3, \bullet\bullet\bullet, \vec{r}_N) = \sum_i^N V_1(\vec{r}_i) + \sum_{i,j}^N V_2(\vec{r}_i, \vec{r}_j) + \sum_{i,j,k}^N V_3(\vec{r}_i, \vec{r}_j, \vec{r}_k) + \cdots\cdots, \tag{2.37}$$

where V_1, V_2 and V_3 represent one-body term, two-body term and three-body term, respectively. N is the number of atoms and $\boldsymbol{r}_i$ is the position of atom i. The atomic force can be calculated by:

$$\vec{F}_i = -\nabla_i V(\vec{r}_1, \vec{r}_2, \vec{r}_3, \bullet\bullet\bullet, \vec{r}_N). \tag{2.38}$$

Base on Equation 2.37, the empirical interatomic potential can be loosely categorized into two classes: pair potentials that contain only two body terms, and many-body potentials that contain three-body terms and higher terms.

The empirical potentials usually have a simple, physical-motivated formula. For example, the Lennard-Jones potential is defined as:

$$V(r) = 4\varepsilon\left[\left(\frac{\sigma}{r}\right)^{12} - \left(\frac{\sigma}{r}\right)^{6}\right], \tag{2.39}$$

where r is the interatomic distance. The first term represents the repulsion between atoms at short distance region, while the second term describes the atomic attraction that dominating at long distance. The parameters σ and ε are determined by fitting the experimental data.

2.3 Neural network potential

The density functional theory (DFT) and empirical interatomic potential have been widely used in the dynamics simulation in the fields of chemistry, condensed matter physics and materials science. However, the bottlenecks for performing these methods are also obvious. DFT calculation requires a huge computational resource, which limits its application to large-scale structures. On the other hand, to construct interatomic potentials providing reliable energies and forces is not easy due to the limitation of the simple formula of the potential. The

development of a method having both high reliability and computational efficiency remains a challenge. To address this problem, an alternative approach for the representation of potential energy surfaces by fitting large data sets from electronic structure calculations has been proposed recently. Since such an approach is based on the machine-learning (ML) techniques, it is referred as machine-learning interatomic potential.[78,79]

The machine-learning interatomic potentials have three characteristics as follows: 1) An ML technique is employed to construct a functional relation between the atomic coordinates and its energy (or atomic forces); 2) Construction of ML potential does not base on any physical approximations, and it is just the mathematical fitting of the reference data; 3) ML potential is based on a set of structure and energy data obtained from electronic calculations, such as DFT. The machine learning techniques include linear regression [25], Gaussian process [23], Kernel regression[80] and neural network (NN) [51]. Based on these techniques, various methods have been developed such as high-dimensional neural network potential (HD NN potential),[49,81–84] Gaussian approximation potential (GAP),[85,86] sparse linear regression method,[87,88] *etc*.

2.3.1 Neural network

Many different types of NNs have been proposed in the literature for various purposes [51], while the most frequently used type is multi-layers feed-forward NNs. The multi-layers NN is consist of a lot of computational units, which is called nodes. As illustrated in Figure 2.4, the nodes are arranged in layers. The NN configuration, that is the number of layers and the number of neurons per layer, determines the complexity of NN. The NN can construct a functional relation between the input values (the value that supply to the input nodes) and the output value (the computed results in the output nodes). In general, one or more hidden layers are employed to bridge the input and the output layer. It should be mentioned that the nodes do not have a clear physical meaning. Instead, they just define the mathematical formula of the NN. The higher the flexibility can be achieved by employing the larger the numbers of layers and nodes per layer. The nodes in each layer is connected to the nodes in the neighboring layers via a connection coefficient, which is called “weights”. The numerical value of a node j in layer n, y_j^n, is then calculated from the values of the nodes y_i^{j-1} in the previous layer j-1 according to:

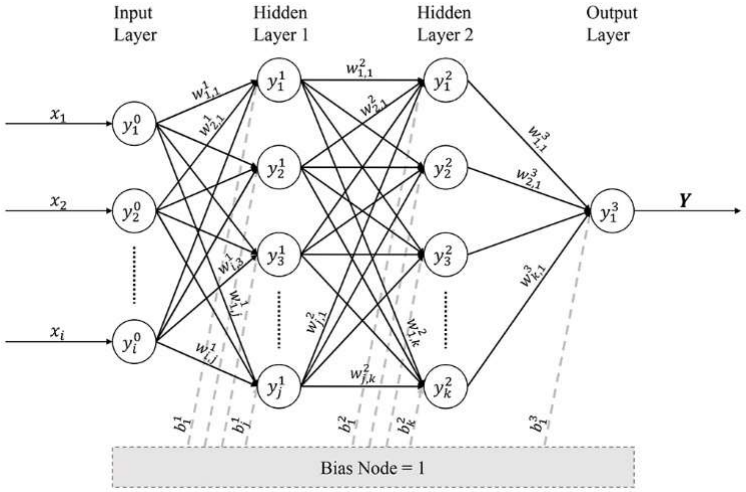

Figure 2. 4: Schematic structure of a small feed-forward NN.

$$y_j^n = f\left(\sum_{i=1}^{N_{n-1}} w_{i,j}^n \cdot y_i^{n-1} + b_i^n\right). \tag{2.40}$$

where $w_{i,j}^n$ represents the connection weights and b_i^n is called the "bias". The function f is called activation function. The frequently used activation functions include Sigmoid, Hyper-tangent, Gaussian and Linear. In this dissertation, the NNs that are used to construct potentials employ the hyperbolic tangent function f^H for the hidden layers, and the linear function f^L for the output layer. The formula of these two functions are:

$$f^H(x) = \frac{1-e^{-2x}}{1+e^{-2x}}, \tag{2.41}$$

and,

$$f^L(x) = x. \tag{2.42}$$

Note that the NN configuration is usually indicated by a set of number for simplicity. For instance, the notation "20-10-10-1" represents a NN that is composed by an input layer with 20 nodes, two hidden layer with 10 nodes each, and 1 output nodes. Such notation method will be frequently used in this dissertation.

2.3.2 General idea of high-dimensional NN potential

The central idea of high-dimensional neural network potential is to construct the potential using a set of atomic NNs[82]. Each atomic NN is simply a multi-layer perceptron with a single output node. The single output of the atomic NN is called atomic energy, which represents the contribution of an atom to the total energy. Thus the potential energy E is given by:[82,89]

$$E = \sum_{i=1}^{N_{atom}} E_i . \tag{2.43}$$

The atomic energies depend on the local atomic arrangement around the center atom, which is referred as "local atomic environment".[82] The local atomic environment of an atom is defined by a cutoff sphere with a radius of R_c. It is assumed that only the atoms inside the cutoff sphere have contribution to the atomic energy. The input of each atomic NN is the atom-centered symmetry functions, which will be elaborated in the next section. The values of symmetry functions depend on the atomic coordinates of all neighboring atoms inside the cutoff sphere, and serve as a structure fingerprint (the measure that quantify the similarity of different structures) of the local atomic environment. It should be mention that although the atomic energies are calculated in the computational process, the parameter of atomic NN is actually optimized using the total energy as the target value. Thus, to extract the atomic energies value from reference DFT calculation would not be necessary. The optimization of NN parameters can be done by gradient-based optimization algorithms, such as Broyden–Fletcher–Goldfarb–Shanno algorithm (BFGS)[90] and Conjugate gradient (CG). Of course, these gradient-based optimization algorithms requires the derivative of total energy error with respect to each parameter of all atomic NN used in the potential. The schematic of high-dimensional NN potential for a structure that contains three atoms is shown in Figure 2.5.[82] It should be mention that the same atomic NNs are assigned to the atoms belonging to the same atomic species. For this reason, the high-dimensional NN potential can be applicable to the systems with an arbitrary size. For example, if a new atom was introduced into the three-atom structure illustrated in Figure 2.5, the NN potential should by modified merely by adding one more atomic NN with the same topology and weight parameters.

For multicomponent systems, the consideration of electrostatic interactions may be necessary due to charge transfer between different elements. For this purpose, J. Behler and his coworker calculated the electrostatic term with either Coulombs equation or Ewald summation, while the charge of each atom is predicted by a second set of atomic NNs.[53] However, they

also claimed that including long-range electrostatic interactions only marginally improves the quality of the NN potential for most materials.[83] It is because that the electrostatic interaction energy inside the cutoff sphere are already included in the atomic energy, thus the additional electrostatic term is relevant for only the electrostatic interactions outside of cutoff sphere. However, the computational costs is raised due to the usage of additional NNs. Therefore, in many previous studies, high-quality NN potentials can be obtained without taking the long-term electrostatic interaction into account explicitly.[56][91] In our study, the NN potential scheme without long-range electrostatic term is adopted.

2.3.2 Atom-centered symmetry functions

To accurately describe the local atomic environment is crucial for constructing robust high-dimensional NN potential. Considering the nature of atomic NN, the structure descriptors used in the NN potential should fulfill the following criteria: 1) the values and slopes of descriptors should be continuous for the application of force calculation; 2) the values of descriptors should be invariant in translation and rotation; 3) the value of descriptors should be unchanged when two atoms of the same element permute; 4) the number of descriptors should

be constant irrespective of the number of atoms exist inside the cutoff sphere.[92] Derivation of structure descriptors that meet such criteria is not easy, but several functions, *i.e.* atom-centered symmetry functions, have been proposed.[92]

All the atom-centered symmetry functions contain a cutoff function to define the local environment. The cutoff function used in the present work is expressed as:

$$f_c\left(R_{ij}\right)=\begin{cases}0.5\times\left[\cos\left(\dfrac{\pi R_{ij}}{R_c}\right)+1\right] & R_{ij}<R_c\\ 0 & R_{ij}>R_c\end{cases}. \tag{2.44}$$

The symmetry functions can be categorized into radial and angular symmetry functions, which describe the radial and angular distribution in the local environment, respectively.

$$G^1=\sum_j f_c(R_{ij}), \tag{2.45}$$

$$G^2=\sum_j e^{-\eta(R_{ij}-R_s)^2}\cdot f_c(R_{ij}), \tag{2.46}$$

and,

$$G^3=\sum_j \cos(\kappa R_{ij})\cdot f_c(R_{ij}), \tag{2.47}$$

The G^1 function is a simple summation of cutoff functions for all neighboring atoms inside the cutoff sphere. In the G^2 function, the cutoff function is combined with the Gaussian functions, so that the Gaussian exponent η is introduced to control the radial resolution. The parameter R_s can be used to shift the peak of function, to facilitate a better description of specific interatomic distance. The G^3 function represents a damped cosine function, in which parameter κ controls the period length. The three kinds of symmetry functions with different parameters are plotted in Figure 2.6.[92] The radial distribution can be described by a set of radial symmetry functions with different parameters, i.e. cutoff radii in G^1, η and R_s in G^2 and κ in G^3.

Two types of angular symmetry functions are also proposed by J. Behler. The angular symmetry functions consider not only the interatomic distance of neighboring atoms but also the angle of the triples formed by the center atom and two arbitrary neighboring atoms. The two kinds of angular are expressed as:

$$G^4 = 2^{1-\zeta} \sum_{j,k\neq i}^{all} \left(1+\lambda\cos\theta_{ijk}\right)\cdot e^{-\eta\left(R_{ij}^2+R_{ik}^2+R_{jk}^2\right)} \cdot f_c(R_{ij})\cdot f_c(R_{ik})\cdot f_c(R_{jk}), \tag{2.48}$$

and,

$$G^5 = 2^{1-\zeta} \sum_{j,k\neq i}^{all} \left(1+\lambda\cos\theta_{ijk}\right)\cdot e^{-\eta\left(R_{ij}^2+R_{ik}^2\right)} \cdot f_c(R_{ij})\cdot f_c(R_{ik}), \tag{2.49}$$

where θ_{ijk} is defined as acos($\boldsymbol{R}_{ij}\cdot\boldsymbol{R}_{ik}/R_{ij}R_{ik}$). In both functions, the parameter ζ is used to control the angular resolution, and λ, which takes +1 or -1, is used to shift the maximum of function between $\theta_{ijk}=0$ and $\theta_{ijk}=\pi$. The angular part of G^4 and G^5 functions are plotted in Figure 2.7. Similar with the radial functions, the Gaussian function with parameter η is also incorporated to control the radial resolution.

2.3.3 Training of neural network

The most import step of constructing the high-dimensional neural network is to determinate the weight parameters of atomic NN, namely, training of neural network. Many different algorithms can be employed to numerically determine such values. The gradient-based optimization algorithms are frequently used for this purpose. As mentioned previously, the optimization algorithms require the derivative of NN potential error with respect to the each weight parameter. Usually, the root mean square error (RMSE) of NN potential energy is chosen as the measure of NN error, *i.e.* the objective function of optimization algorithm. The RMSE is defined as:

$$\mathrm{RMSE} = \sqrt{\frac{1}{N}\sum_{i=1}^{N}\left(E_{i,ref} - E_{i,NN}\right)^2}, \tag{2.50}$$

where N is the number of strucutures that used as the reference data, $E_{i,ref}$ and $E_{i,NN}$ are the total energy of the ith structure obtained by reference electronic calculation and NN potential prediction, respectively. It should mention that for the training of atomic NN, the backpropagation algorithm is usually adopted, which makes parameters converge to a local

minima. Several approaches are proposed to find the global minimum in the weight parameter space, such as Kalman filter[93] and the Levenberg–Marquardt algorithm. However, application of these algorithms is extremely challenging due to a lot of parameters used in the NN potential. Therefore, many times of training of NN with randomly initialized weights are usually performed to find a local minima with sufficient accuracy.

The iterative training ensures the NN potential provides reliable energies for structures not included in the training set. However, this would be not enough. Only if the NN potential yields accurate results for the structures not used in the training, it can be safely used in the atomic simulation. For this purpose, an independent validation data set, *i.e.* the so-called testing set, should be prepared. During the optimization of NN weights, the RMSE of both training and testing set should be monitored. As shown in Figure 2.8, both the training and testing errors reduce rapidly in the initial stage of training. Then, the testing error will reach the minima and then start to increase, while the training error still decreases monotonously. The different behaviors between the training and testing error curves in the latter part indicate the overfitting of NN potential, which occurs due to the too-flexible function formula of NN. To avoid the overfitting, “early stopping” method is adopted in our study. In the early stopping method, the training and testing error in each training iterations are monitored, and training of NN will be truncated when the testing error starts to increase. The early stopping method gives an appropriate number of training iterations.

The high-dimensional neural network can provide a very accurate description of potential

energy surface, owing to its complicated non-linear formula. It provides the total energy of a structure directly, and then the atomic forces can be calculated according to:

$$F_\alpha = -\frac{\partial E}{\partial \alpha} = -\sum_{j=1}^{N_{atom}} \frac{\partial E_j}{\partial \alpha} = -\sum_{j=1}^{N_{atom}} \sum_{\mu=1}^{N_{sym,j}} \frac{\partial E_j}{\partial G_{j\mu}} \cdot \frac{\partial G_{j\mu}}{\partial \alpha}, \tag{2.51}$$

where α represents the x, y and z axis of Cartesian coordination, E_j is the atomic energy of the jth atom and $G_{j\mu}$ is the μth symmetry function used for the jth atom.

Chapter 3

Potential for Cu Diffusion in Amorphous Ta_2O_5

In this chapter, a simple neural network (NN) interatomic potential to investigate the diffusion of a single Cu atom in amorphous Ta_2O_5 is developed. The developed potential is as accurate as the DFT in predicting hopping paths and the corresponding barrier energies in a given amorphous structure. Although the developed NN-based approach exhibited some limitations since it was constructed specifically for Cu, the obtained results showed that the NN potential was able to satisfactorily describe the Cu diffusion behavior.

3.1 Background

3.1.1 Ta_2O_5 crystalline

Ta_2O_5 have a wide band gap and high-constant[94], thus it is frequently used in various electronic devices, such as the capacitor in DRAM devices, gate dielectric thin-film in transistors, and coating materials in solar cells and photocatalyst. Basically, Ta_2O_5 has four crystal structures at low and high temperature. The β-Ta_2O_5 and δ-Ta_2O_5 exist at low temperature. The β-Ta_2O_5 has orthorhombic structure and *Pccm* space group. A β-Ta_2O_5 cell contains 4 Ta atoms and 10 O atoms, and the lattice constants are a= 6.217 Å, b=3.677 Å and c=7.794 Å.[95] The δ-Ta_2O_5 has hexagonal structure. [96] Its space group is *P6/mmm*. The unit

cell contains 4 Ta atoms and 10 O atoms. The lattice constants are a = 3.370 Å and c = 8.432 Å according to the calculation. The structure of high-temperature Ta_2O_5, namely H-Ta_2O_5 is is determined to be tetragonal and the space group of $I4_1/amd$. The L-Ta_2O_5 also exists at low-temperature but is stabilized only in the Ta_2O_5-WO_3 binary system. The L-Ta_2O_5 is measured to be the orthogonal structure. Figure 3.1 gives the illustrations of all four kinds of crystal Ta_2O_5.

Except for the experimental measurements, the crystal structures, as well as the electronic properties of crystal Ta_2O_5, were also intensively investigated with first-principles calculations.[32,97–99] The GGA and LDA calculations show that the band gap of β and δ-Ta_2O_5 are ~0.1 eV and ~1eV, respectively. To overcome the well-known underestimation of band gap by DFT with conventional LDA and GGA, HSE06 hybrid functional was used to calculate the DOS of the two low-temperature Ta_2O_5 crystals by Y. Wu *et al.*[97] The HSE06 functional opens the gaps to 0.9 eV and 2.0 eV for the two phases.

3.1.2 Amorphous Ta_2O_5

The structures of the different crystalline polymorphs of tantalum oxides are intensively

studied by both from diffraction-based experimental measurements and from the atomic simulations using the density functional theory. However, there are only a few publications about the structure of amorphous Ta_2O_5. The structural information is the foundation of further investigation of other properties of this important material. R. Bassiri *et al* tried to get a deeper understanding of the amorphous structure based on both experiment and atomic simulation. [100] First, the amorphous film was fabricated by argon-ion-beam-sputtering. Then electron diffraction patterns were measured. In order to accurately probe the atomic structure and gain a full understanding of the information stored in the RDF, reverse Monte Carlo (RMC) refinements of atomistic models was performed using the experimentally obtained scattering intensities. Information from the density-functional-theory-based molecular dynamics simulations of liquid quenching was used in the RMC refinements in order to ensure that a physically meaningful model of the amorphous material, which fits both the theoretical and experimental data, can be obtained.

The atomic structure that obtained from the aforementioned method is shown in Figure 3.2. The total pair distribution function (PDF) of the atomic structure is shown in 3.2(c). The first peak position in the PDF corresponds to the Ta–O distances found at 1.93 Å. The shoulder of the second peak at about 3.2 Å can be attributed to the Ta–Ta distances. It was found that the refined amorphous structure had a considerable contribution from the planar or nearly planar Ta_2O_2 fragments with a relatively short average Ta–Ta distance of 3.2 Å. The average coordination numbers computed from the refined model are 6.53 for Ta and 2.09 for O.

Another attempt to reproduce amorphous Ta_2O_5 structure was conducted by B. Xiao *et al*.

Their model was generated with a much simple atomic simulation approach: melt quenching method. In B. Xiao's work, the model for amorphous Ta_2O_5 was generated using *ab-initio* MD: the crystalline hexagonal δ-Ta_2O_5 was first melted at 6000K and then cooled down to 300K with a quenching speed of 4 K/3fs. In the resultant amorphous structure, the length of Ta-O bond is estimated to be 1.97 Å, and Ta-Ta bond is 3.2 Å. The presence of considerable amount of Ta_2O_2 quadrangle fragments also can be found in this model. All these structure characteristics are consistent with the study of R. Bassiri *et al*.

3.1.3 Cu diffusivity in amorphous Ta_2O_5

The diffusion coefficient (D_{Cu}) and the solubility of Cu^+ ions in Ta_2O_5 were measured by N. Banno *et al*. The sample is fabricated by depositing a 120 nm thickness Ta_2O_5 film on Cu with pulsed laser deposition. The Cu diffusion coefficient is measured by characterizing the Cu distribution profile in the sample by secondary ion mass spectroscopy (SIMS) after annealing at different temperatures. Annealing temperatures vary in the range of 200 ℃–500 ℃. The Cu diffusivities derived from the SIMS depth file. The temperature dependence of Cu diffusivity obeys the Arrhenius relationship. By extrapolating the temperature dependence of obtained D_{Cu}, the room temperature diffusivity was estimated to be 4.9×10^{-20} cm^2/s, which is extremely low in comparison with the diffusion coefficient in other electrolytes. Due to the suppressed Cu^+ ion diffusion, the Ta_2O_5 switch provides a high turn-on voltage V_{ON} (0.65 V), which is a desirable characteristic for the application of Ta_2O_5 based atomic switch in a field programmable gate array.

Another experimental evaluation of room temperature Cu diffusivity was performed by T. Tsuruoka *et al*. They fabricated Cu/Ta_2O_5/Pt multilayer thin film, which is an atomic switch device, by electron-beam (EB) deposition. Then the cyclic voltammetry (CV) measurement was performed. Figure 3.3(a) shows the typical variation of CV curves for Cu/Ta_2O_5/Pt cells measured with different sweep rates v. The current peaks in the positive (negative) sweep direction are associated with the oxidation (reduction) processes at the anode interface. In general, we could clearly observe two oxidation current peaks and two reduction current peaks in the Cu/Ta_2O_5/Pt cell as indicated by $j_{p,ox1}$, $j_{p,ox2}$, $j_{p,red1}$, and $j_{p,red2}$.The reduction current density j_p is related to the ionic concentration c_{ion}, the number of electrons transferred z and the sweep rate v and the diffusion coefficient D. The relationship can be estimated from the

Randles–Sevick equation

$$j_p = 2.99\times10^5 \cdot z^{3/2} \cdot c_{ion} \cdot \sqrt{\alpha D v} \tag{3.1}$$

where α is the charge transfer coefficient. The values of diffusion coefficient D estimated using Equation (3.1) are plotted in Figure 3.3(b) as a function of v. D increases with the increase of v. The diffusion coefficient D can be estimated to be $\approx 10^{-13}$ $cm^{2/}s$ for Cu^{2+} at room temperature. However, this estimated value of D is about eight orders of magnitude higher than the extrapolated diffusion coefficient of Cu ions evaluated by N. Banno *et al*. The enhanced diffusion coefficient may come from the downscaling of the film thickness as well as the structural difference of the deposited Ta_2O_5 film.

3.1.4 Research objective

Due to the successful fabrication of $Cu/Ta_2O_5/Pt$ atomic switch, the Cu diffusion behavior in amorphous Ta_2O_5 has drawn considerable attention. However, the theoretical study is still lacking. Similar to many theoretical studies about atomic diffusion in crystal, the NEB method combined with DFT is applicable to study Cu diffusion in an amorphous Ta_2O_5 supercell to evaluate atomic migration energy. However, due to the disordered and stochastic structure dozens, or even hundreds of diffusion pathways should be characterized in an amorphous

supercell that contains about 100 atoms. For this reason, the computation cost for amorphous materials is much more expensive than the crystalline case. In this chapter, we want to theoretically reveal the Cu diffusion mechanism in atomic level. More importantly, we want to develop a simulation tool that can be efficiently predict of atomic diffusion behavior in amorphous materials with relatively low computational cost.

The outline of this chapter is as follows. Section 3.2 describes a new NN potential to examine the diffusion behavior of a single Cu atom in amorphous Ta_2O_5. Although the described system contains three different atomic elements, the utilized NN potential is much simpler than those proposed previously for ternary systems.[56] Hence, such method is named as "simplified neural network potential" in this dissertation. The potential energy surface of Cu, diffusion paths, and barrier energies obtained using the NN potential (which are compared with the results of DFT calculations) are presented in Section 3.3. In Section 3.4, the diffusion behavior of Cu is further examined by calculating the diffusion network, diffusion coefficients, and effective diffusion activation energy. In Section 3.5, we will explore the possibility of applying the potential to different amorphous Ta_2O_5 matrices. The obtained conclusions are provided in Section 3.6.

3.2 Construction of simplified NN potential

3.2.1 General Idea

The main idea of the simplified NN potential utilized in this study is to express the total energy of the structure containing a relaxed amorphous Ta_2O_5 matrix and a single Cu atom, $E_{Ta2O5+Cu}$, as the sum of the energies of the pure Ta_2O_5 matrix, E_{Ta2O5}, and dissolution energy of the Cu atom, $E_{dissolution}$. The second term $E_{dissolution}$ can be further subdivided into two parts: 1) the energy change when the Cu atom is inserted into the frozen host matrix, E_{insert}, and 2) the energy change due to the host matrix relaxation (*i.e.* the displacements of nearby Ta and O atoms caused by the insertion of Cu atom), E_{relax}:

$$E_{Ta_2O_5+Cu} = E_{Ta_2O_5} + E_{dissolution} = E_{Ta_2O_5} + E_{insert} + E_{relax}. \quad (3.2)$$

The value of the first term, E_{Ta2O5}, can be directly obtained by performing DFT calculations, while the NN approach is focused on predicting the value of $E_{dissolution}$. The value of E_{insert} is determined from the atomic arrangements around the inserted Cu atom *before* the relaxation, while that of E_{relax} is determined from the matrix structure *after* the relaxation. In this work, however, we implicitly assumed the positional shifts of atoms in the host Ta_2O_5 matrix in structure optimization were not significant. In this case, the magnitudes of both E_{insert} and E_{relax}, and thus that of $E_{dissolution}$ can be approximated as a function of atomic arrangements around the inserted Cu atom *before* the relaxation. Fortunately, this assumption appears to be valid for NEB calculations since the atomic displacements in the host matrix are usually smaller than 0.5 Å. Then we can forget about the host matrix structure *after* the relaxation and consider only the initial host structure and the Cu insertion position explicitly. It should be noted that although the matrix relaxation was not actually preformed in calculations using the constructed NN potential, the energy after matrix relaxation was directly predicted, because E_{relax} calculated with in the DFT was taken into account in the training of NN. In another word, we expect that the effects of Ta_2O_5 relaxation *after* the Cu insertion were automatically taken into account in the NN potential.

The use of a simplified NN potential considerably reduces the complexity of the computational procedures utilized in previous works because it contains only one NN, while the other high-dimensional NN potentials consist of multiple NNs corresponding to different species. The number of parameters in a simplified NN potential is equal to several hundred, which is much smaller than that in a typical NN potential. The details of the utilized simplified NN potential will be provided in the following sections.

3.2.2 NN input and output

We think the symmetry function proposed by J. Behler *et al* is a good choice to describe the atomic environment of Cu,[81,92] because they provide a unique description of the atomic positions and contain a constant number of functions independent of the number of atoms in the supercell. The applicability of symmetry functions is proved in the construction other kinds of NN potentials. The detailed information of symmetry function has been introduced in the

Section 2.3. In the present work, G^2-type radial symmetry functions (Equation 2.30) and G^5-type angular symmetry functions (Equation 2.33) were used.

The NN defines a functional relation between the atomic environment of a Cu atom in the amorphous matrix (which is described by the symmetry functions in the nodes of the input layer) and the dissolution energy of the Cu atom $E_{dissolution}$, which is obtained in the node of the output layer. After the value of $E_{dissolution}$ is calculated, the total energy of the structure can be easily computed by adding the energy of the pure amorphous matrix E_{Ta2O5}. As we mentioned previously, in the training procedure of the present NN, the pre-relaxation structures were used as the input, while the corresponding energies after matrix relaxation were used as the target. Thus, the effects of Ta_2O_5 relaxation after Cu insertion were automatically incorporated into the training process of NN. Similar to the high-dimensional NN potential, the force component acting on the Cu atom F_α with respect to the coordinate $\alpha = x, y,$ or z can be evaluated according to the chain rule:

$$F_\alpha = -\frac{\partial E}{\partial \alpha} = -\sum_\mu \frac{\partial E}{\partial G_\mu} \times \frac{\partial \mu}{\partial \alpha}. \tag{3.3}$$

However, the simplified NN potential related system energy with only the Cu position. Thus the atomic forces of other atoms cannot be calculated in this method. The molecular dynamics simulation cannot be performed with the simplified NN potential.

3.2.3 Amorphous Ta_2O_5 model

A model for the amorphous Ta_2O_5 matrix was constructed using the melt quenching method based on *ab-initio* MD. The simulation was performed with VASP. In the calculation, The PAW method was adopted to treat atomic core electrons, while the generalized GGA (PW91) was adopted to describe the electron-electron interactions.[101,102].A plane-wave basis set with a cutoff energy of 500 eV was used, and 2×2×4 *k*-points were adopted. Here the crystalline hexagonal δ-Ta_2O_5 consisting of 32 Ta and 80 O atoms was used as the initial structure. The studied structure was first melted at 6000 K for 9 ps and then cooled down to 300 K at a rate of 4 K/3 fs. Finally, the structure was annealed at 300 K for 9 ps (the utilized time step was set to 3 fs during the entire simulation). The final structure obtained during the melt quenching procedure was further optimized at a force tolerance of 0.01 eV/Å (its corresponding unit cell was relaxed with respect to the atomic coordinates and cell shape).

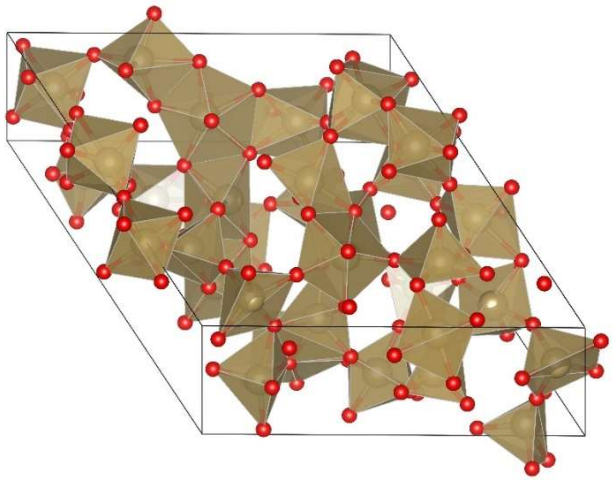

Figure 3.4: The structure of amorphous Ta_2O_5 generated using the melt quenching method of the utilized DFT procedure.

After relaxation, the density of amorphous Ta_2O_5 was 7.55 g/cm^3, which was close to the magnitude obtained by R. Bassiri *et al.*[100] The structure of the amorphous Ta_2O_5 created by the aforementioned process is shown in Figure 3.4.

3.2.4 Training data

Construction of a neural network potential acquires the training procedure, in which the weight parameters of NN are determined according to the reference data. As a result, a training database that contains a variety of training structures and corresponding energies should be constructed. All the training data utilized for training the NN potential were generated based on the amorphous Ta_2O_5 model created in the proceeding section.

Considering the input and output of the NN potential, we can see that a piece of training data should contain 1) the structural information about Cu insertion position, and 2) the Cu dissolution energy at this position (in which the amorphous matrix relaxation should be taken into account). The procedure of creating training data is as follow. First, one Cu atom was randomly inserted into the amorphous Ta_2O_5, and the resulting structure was optimized while keeping the Cu atom position fixed. During optimization, 1×1×2 *k*-points were used for all structures, and the force tolerance was equal to 0.05 eV/Å. Lastly, the Cu dissolution energy $E_{dissolution}$ at this position can be obtained by subtracting the energy of pure Ta_2O_5 matrix from

the final total energy. The same pseudopotential and cutoff energy are adopted as previous melt quenching simulation. To construct the NN potential, 2000 training data were obtained. The resulting data was randomly distributed into two sets: a training set (90%) which will be used as the reference data to tuning the parameters of neural network, and an independent testing set (10%) which will be used as independent validation data.

3.3 Performance of NN Potential

3.3.1 Energy calculations

We utilized a multi-layer feedforward neural network (MLFF NN) to express the relation between the atomic structure and energy, as was done in most of the previous studies of NN potentials. For the activation function, the hyperbolic tangent function f^H was used for the hidden layers, and the linear function f^L for the output layer. The

Table 3.1 Convergence testing of the cutoff distance for the utilized NN potential.

Configuration	Cutoff distance (Å)	Training RMSE (eV)	Testing RMSE (eV)
36-8-8-1	4	0.039	0.063
36-8-8-1	5	0.027	0.048
36-8-8-1	6	0.026	0.062
36-8-8-1	7	0.025	0.052
36-8-8-1	8	0.024	0.050
36-8-8-1	9	0.024	0.051

Broyden−Fletcher−Goldfarb−Shanno (BFGS) algorithm[90] was adopted to train the NN , while a root-mean-square error (RMSE) between predicted value and reference value was used

as the objective function.

Determination of the parameters of NN potential (such as the cutoff distance R_c of symmetry functions, the number of hidden layers and the number of nodes in each layer) needs a testing procedure. We tested the convergence of the cutoff distance R_c using NN potentials with the architecture of 36-8-8-1. The symmetry functions with the cutoff distance in 4~9 Å were used as the input of NN. After the "early stop" method (introduced in Section 2.3.3) was adopted to determine the number of training iterations. The RMSEs of NN potentials in the training and testing sets are listed in Table 3.1. As we can see, the accuracy of NN potential increases with the cutoff distance. The accuracy is basically converged when the cutoff distance was larger than 7 Å.

Then several NN configurations was tested to find the optimum NN to represent the

Table 3.2 Testing the NN configurations with different sets of the input symmetry functions.

Configuration	Num. of parameters	Training RMSE (eV)	Testing RMSE (eV)	Configuration	Num. of parameters	Training RMSE (eV)	Testing RMSE (eV)
60-10-10-1	731	0.037	0.113	36-8-8-1	377	0.024	0.050
60-9-9-1	649	0.038	0.125	36-7-7-1	323	0.037	0.061
60-8-8-1	569	0.039	0.096	36-6-6-1	271	0.041	0.060
60-7-7-1	491	0.039	0.107	36-5-5-1	221	0.049	0.064
60-6-6-1	415	0.054	0.112	36-4-4-1	173	0.058	0.070
60-5-5-1	341	0.064	0.124	36-8-8-8-1	449	0.016	0.043
60-4-4-1	269	0.085	0.122	36-6-6-6-1	313	0.037	0.062
60-6-6-6-1	457	0.037	0.130	36-4-4-4-1	193	0.048	0.061
60-4-4-4-1	289	0.063	0.113	16-16-16-1	561	0.037	0.061
36-14-14-1	743	0.013	0.054	16-12-12-1	373	0.034	0.061
36-12-12-1	613	0.015	0.056	16-8-8-1	217	0.033	0.064
36-10-10-1	491	0.017	0.045	16-6-6-1	151	0.049	0.060
36-9-9-1	**433**	**0.023**	**0.039**	16-6-6-6-1	193	0.047	0.064

potential energy surface. Three different sets of symmetry functions was used to describe the chemical environments of the atoms. The set I included 8 G^2 functions and 22 G^5 functions for O and Ta atoms, respectively. Set II included 8 G^2 functions and 10 G^5 functions. Set III includes 8 G^2 functions. The RMSEs of the energies are listed in Table 3.2, and the NN configuration with the lowest testing RMSE is shown in bold in the table. The optimum NN is based on the input symmetry function set II (the parameters of these input symmetry functions are presented in the appendix), and it contains two hidden layers and 9 nodes per layer. The NN potential contains 433 parameters in total. This NN architecture was adopted in the following study.

After training, the NN potential achieved a root-mean-square error (RMSE) of 23 meV/structure for the reference training set, and RMSE of 39 meV/structure for the independent testing set. The mean absolute errors (MAEs) obtained for the training and test

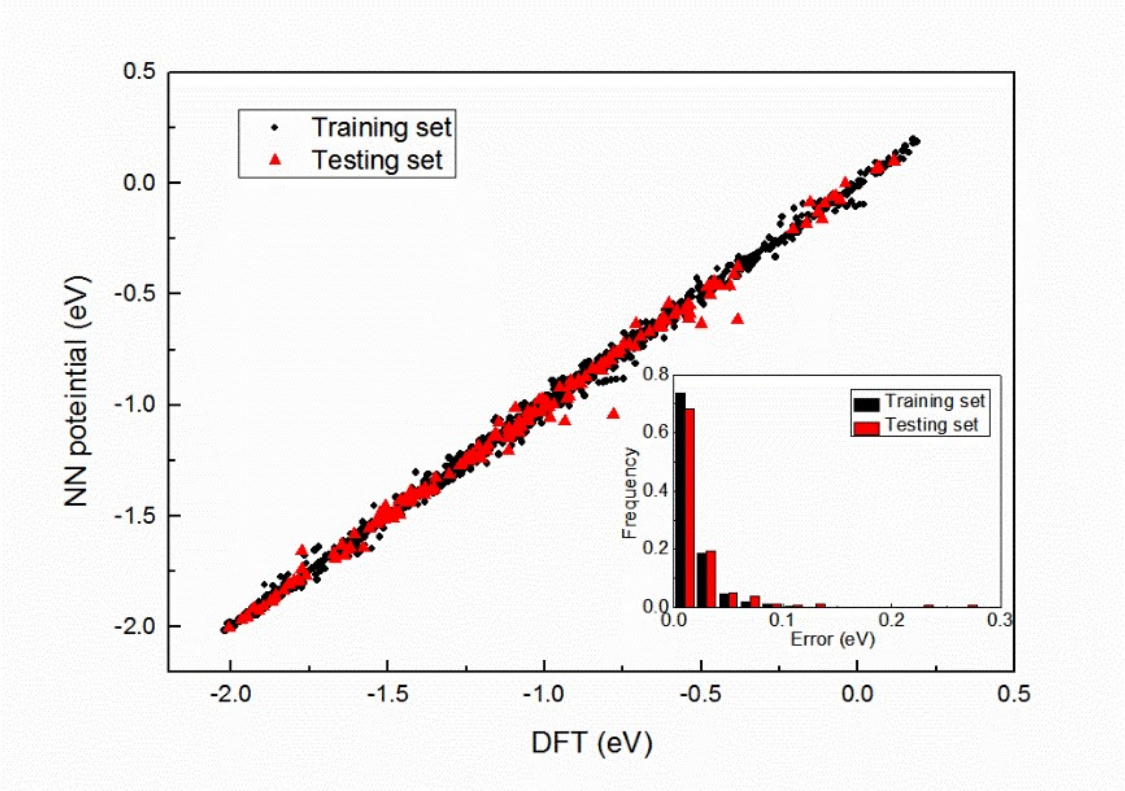

Figure 3.5: A comparison between the total energies of the training set and testing set structures obtained using the DFT and NN approaches. The inset contains the MAE distributions ($|E_{NNP} - E_{DFT}|$) calculated for these two data sets.

structures were 16 and 21 meV/structure, respectively. According to the results presented in Figure 3.5. The energies of the training and test structures calculated using the NN potential matched the values obtained via DFT simulations (the corresponding correlation coefficients were equal to 0.998 and 0.997, respectively).

It should be noted that the calculation of the total energy of a single geometric configuration, which was conducted using the current implementation of the NN potential

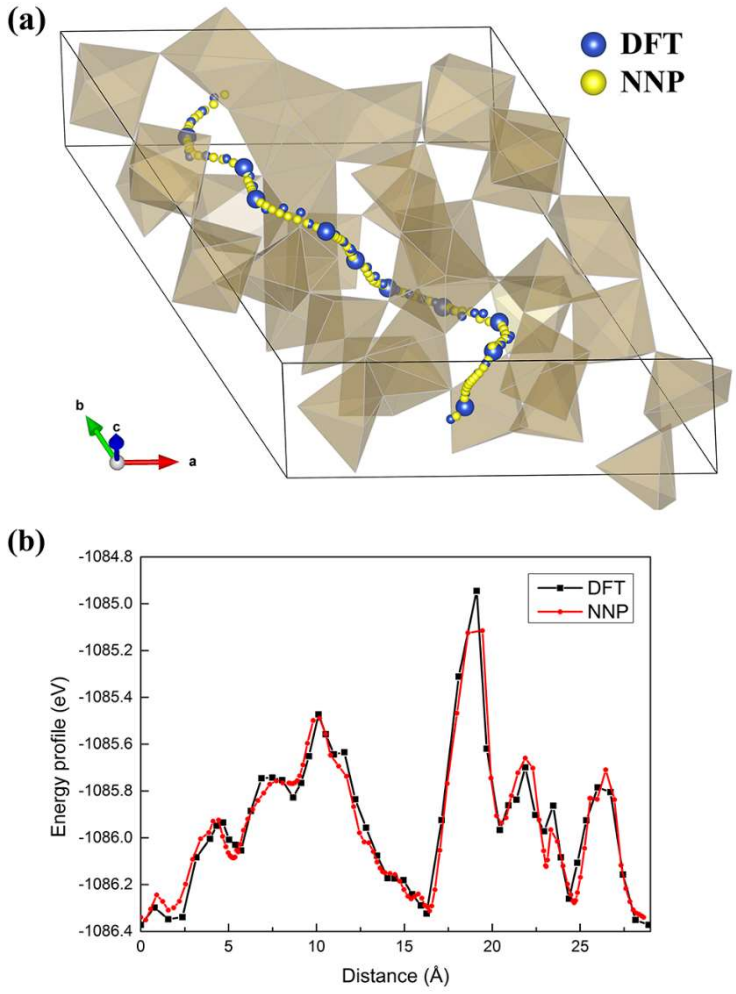

Figure 3.6: A comparison between the NEB calculation results obtained for the selected diffusion pathway of a Cu atom in amorphous bulk Ta_2O_5 using the DFT and NN potential approaches. (a) Transient images of the Cu atom obtained during the NEB calculations, from which the locations of diffusion pathways can be acquired. The convex polyhedrons represent Ta–O species in the amorphous matrix, while O and Ta atoms are not shown for clarity. (b) Energy profiles computed along the corresponding diffusion paths.

model on a single CPU core (Intel® Xeon® W3565 processor), took only 0.001 s (for comparison, performing the same task using the VASP code and 12 CPU cores of the same type took about 1 h). Hence, the computational speed obtained using the NN potential was 10^7 times greater than that observed during DFT simulations

3.3.2 NEB calculations

To test the reliability of the NN potential for describing the atomic diffusion process, the former was used to predict a long path of the Cu diffusion in the amorphous Ta_2O_5 matrix and the corresponding energy profile via NEB simulations. During this procedure, the overall motion of the Cu atom was described by several hops between the equilibrium sites. The locations of images after optimization (representing the diffusion path) are shown in Figure 3.6(a). The obtained NN potential was in good agreement with the DFT results. The lengths of the diffusion paths defined as the sums of distances between the adjacent Cu transient positions were equal to 28.6 and 28.9 Å for the NN potential and DFT simulations, respectively. The corresponding energy variations along the long-range diffusion path, which are plotted against the diffusion length in Figure 3.6(b), also demonstrate a good agreement between the two utilized methods. The largest mismatch between the data obtained via the NN potential and DFT calculations was about 0.15 eV, which corresponded to the saddle point of the highest barrier. Apart from the inherent inaccuracy of the NN potential method, a large discrepancy observed for this point might also result from the NEB images that missed the saddle point of the minimum energy path, which represented a common problem for NEB calculations and could be fixed by using a climbing image NEB method.[64]

3.4 Cu Diffusion in amorphous Ta_2O_5

3.4.1 Metastable interstitial positions

Determining potential equilibrium sites in amorphous bulk materials is a challenging task because of structural disorder. To avoid bias, it is important to locate all interstitial sites without

making assumptions about their structure. Owing to the high computation speed of the NN potential, all possible Cu positions in the amorphous Ta_2O_5 matrix structure were investigated in this work. The computational procedure is: first, Cu atoms were inserted at each of the points defining the 50×50×50 uniform grid in the matrix supercell, and then their positions were optimized using the BFGS algorithm. The inserted Cu atom will shift to the closest energetic minimum position, *i.e.* the equilibrium site. Since the very dense initial mesh was used, we supposed that all the equilibrium sites on the potential energy surface can be found in this way. Of course, many of the Cu atoms inevitably shift into the same energy basin, and their final positions were close both spatially and energetically. However, these atoms usually do not end up with exactly the same spatial position, because the usage of lax force convergence criterion which terminated Cu optimization slightly before reaching energy minimum. Therefore, hierarchical clustering analysis was performed for the optimized interstitial positions using the distances between two Cu atoms as the metric[103]. it should be noted that the described technique was used in previous studies to search for equilibrium sites in amorphous bulk materials[46,104]. As a result, the calculated interstitial positions were successively merged until all the distances between clusters became longer than the cutoff distance of 0.5 Å. During

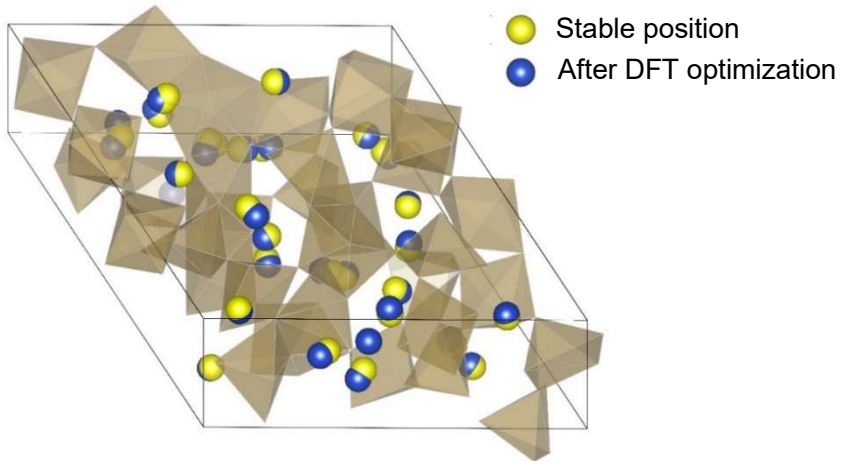

Figure 3.7: The metastable Cu interstitial positions that obtained from the searching protocol using neural network potential are represented by the yellow sphere. The final Cu positions after further optimization in the DFT calculation is represented by the blue spheres. The polyhedrons represent the shape Ta-O units in the amorphous Ta_2O_5 model.

this procedure, 29 different clusters were obtained. For each cluster, the energy variance of all configurations was below 0.04 eV, and the lowest energy configuration was used to represent the metastable Cu interstitial position. These metastable Cu interstitial positions were represented by the yellow spheres in Figure 3.7.

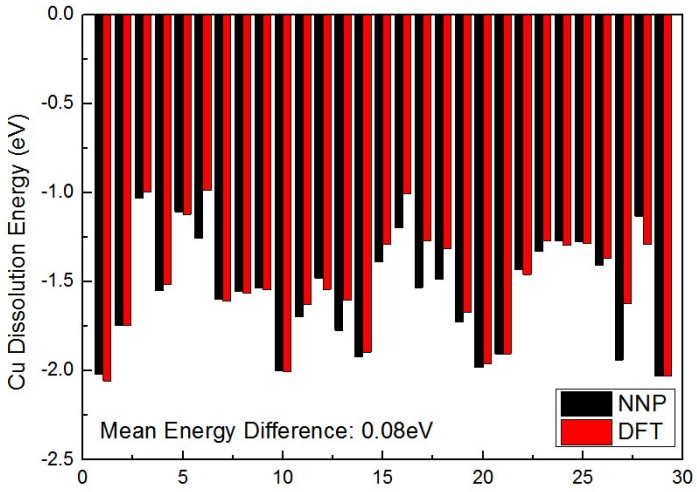

Figure 3.8: The black bars represent the energies of structures predicted by the neural network potential when the Cu atoms are inserted into the 29 equilibrium sites of the amorphous matrix. The red bars represent the energies calculated by DFT after the further optimization. For clarity, the Cu dissolution energies are shown, instead of the total energies.

The Cu stable positions found by the aforementioned approach was further validated with DFT calculation using VASP. In doing so, we created a set of initial structures in which one Cu atom located at the equilibrium site. These structures were then fully optimized within VASP code. The Cu atoms should not move considerably if the Cu stable positions predicted by the neural network potential are reliable. In our test, the Cu atoms shifted for 0.23 Å in average during the DFT optimization, while the largest atomic position shift was about 0.59 Å. For all the Cu stable positions predicted by the neural network potential, we could find the corresponding stable positions in the DFT calculation. This demonstrates the reliability of neural network potential in searching equilibrium positions. The Cu positions after the DFT optimization are shown in Figure 3.8 by the blue spheres. The energies of these equilibrium structures are plotted in Figure 3.8, in comparison with the energies of equilibrium structures predicted by the neural network.

3.4.2 Diffusion network

According to the results obtained in the previous section, 29 metastable interstitial positions of Cu atoms were determined using the NN potential. Assuming that a Cu atom can hop between the two adjacent interstitial positions with a distance between them less than 5 Å, 67 diffusion paths have been obtained (during the search, the paths that can be considered as the combinations of two or more individual pathways were eliminated). It should be mentioned that t he cutoff distance of the atomic hopping should be large enough, so that the diffusion pathways can link all the metastable interstitial positions together, and form a 3D diffusion network. However, the allowance of large hopping distance inevitably introduces diffusion pathways that actually are the combination of two or several individual hopping. Such diffusion pathways should be removed manually. After that, the activation energies of the resulting pathways were determined using the NEB method. The spatial locations of all the obtained

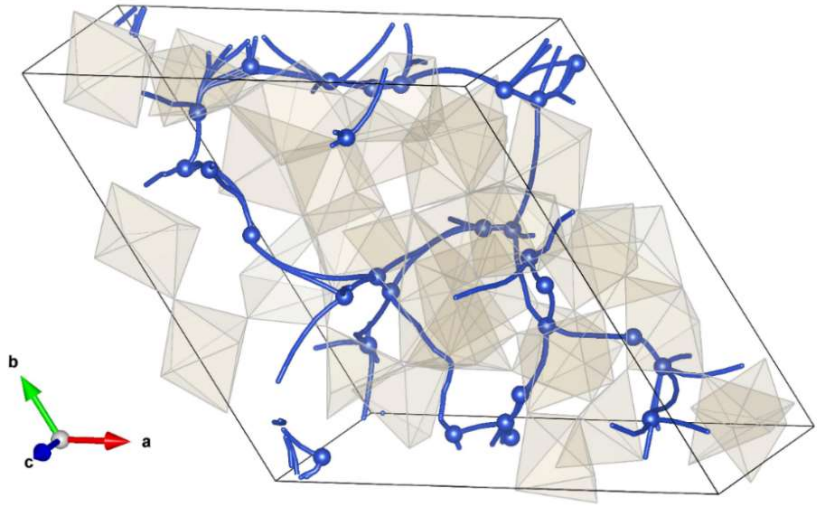

Figure 3.9: Equilibrium sites (blue spheres) and diffusion pathways (blue lines) determined for the Cu atoms in the bulk amorphous Ta_2O_5 structure. The polyhedrons represent Ta–O polyhedrons, while O and Ta atoms have been removed for clarity.

diffusion paths are depicted in Figure 3.9.

For each individual diffusion path, two different activation energies corresponding to the two opposite hopping directions were computed. In general, for the path connecting sites *i* and *j* with the saddle point energy E_{ij} (which represents the maximum energy of the NEB energy

profile), the activation energy of Cu diffusion from *i* to *j* is equal to E_{ij}–E_i (here E_i is the energy of site *i*), while the activation energy of the diffusion in the opposite direction equals E_{ij}–E_j. The calculated barrier energies of the diffusion paths span across a wide range between 0.01 eV and 1.79 eV with an average value equal to 0.55 eV, while their lengths vary from 0.91 to 4.98 Å. Figure 3.10 displays the distribution of barrier energies determined for single hops. Although most of the pathways exhibit relatively small barrier energies of less than 0.2 eV, it does not imply that the corresponding Cu diffusion activation energies are very low because a particular Cu atom may not be able to escape from the narrow region between the sites connected via the paths with such small energies. Thus, the statistic of single hopping barrier energy cannot reveal the cha racteristic of atomic diffusion behavior. For this reason, we proposed a new measurement, namely, periodical paths barrier energy. The periodical diffusion paths are defined as the pathways connecting equilibrium sites and their equivalents in the adjacent supercells. The barrier energy of a periodical path was equivalent to the largest barrier energy calculated for individual hops. We sampled the shortest (determined from the obtained number of nearest-neighbor hops) and the second shortest periodical diffusion paths, and the

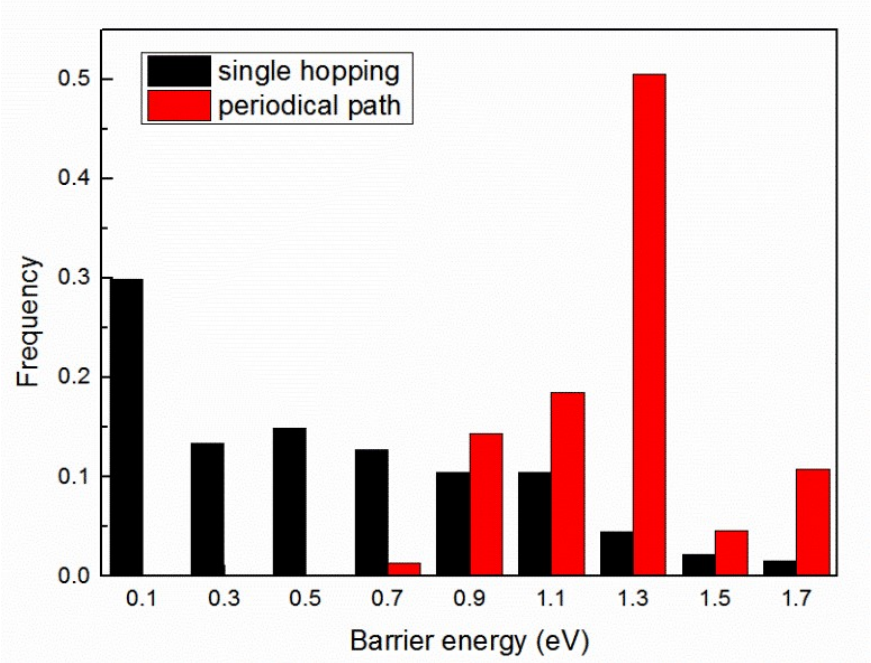

Figure 3.10: Distributions of the barrier energies calculated for all diffusion pathways of atomic Cu in bulk amorphous Ta_2O_5. The black columns correspond to individual hops (single NEB calculations), and the red columns represent the periodical paths, which connect equilibrium sites with their equivalent sites in the adjacent supercells. The frequencies were normalized with respect to the total number of diffusion pathways.

results of the statistical analysis summarized in Figure 3.10 reveal that the obtained barrier energies of the periodical paths vary from 0.68 eV to 1.79 eV. Interestingly, the lowest value (0.68 eV) corresponds to the activation energy of Cu diffusion in the diffusion network obtained via kinetic Monte Carlo (KMC) simulations, which will be described in detail in the next subsection.

3.4.3 KMC simulations of Cu diffusion

The diffusivity and diffusion activation energy of Cu atoms were examined by performing KMC simulations, which is introduced in Section 2.1.3. The in this simulation we assume the vibration frequency of Cu atom (*v'* in Equation 2.13) is equal to about 10^{13} s^{-1}. The Cu diffusion barrier energies calculated with NEB are used as the input parameters of KMC simulation. At the beginning of the simulations, Cu atoms were distributed randomly among the interstitial sites according to the Boltzmann-weighted energy relationship. Afterwards, the initial state was equilibrated by running 5000 MC events per atom. After reaching equilibrium, additional 10 million MC events were run for 1000 atoms, and the self-diffusivity of Cu atoms was evaluated from their respective trajectories using the Einstein expression (Equation 2.13):

Figure 3.11(a) describes the self-diffusivity of Cu atoms in *a*-Ta_2O_5 estimated at

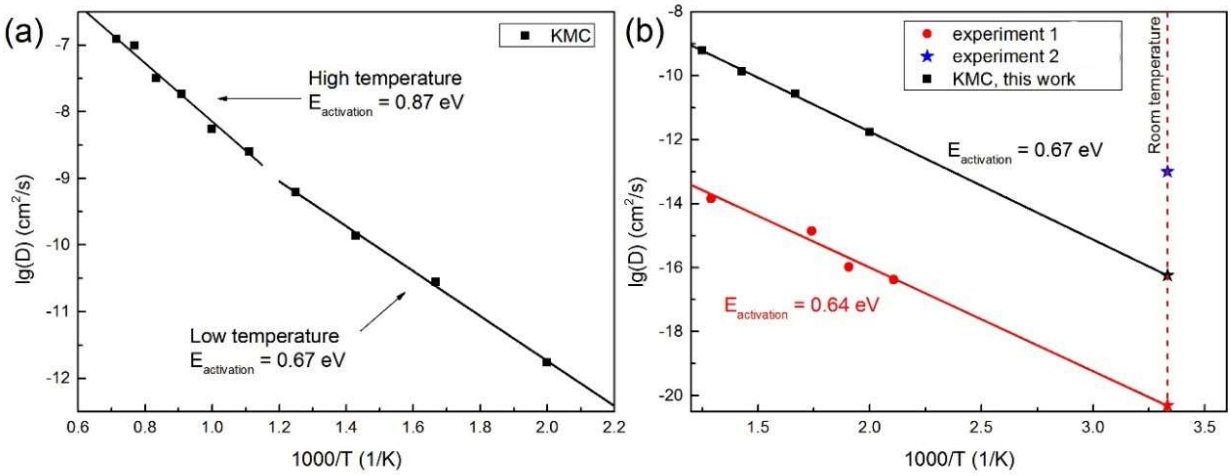

Figure 3.11: (a) Cu self-diffusivity in the amorphous bulk Ta_2O_5 structure calculated from the results of KMC simulations. The two black lines represent the linear fits of the simulation data obtained at high temperatures (900–1400 K) and low temperatures (500–800 K). (b) The comparison of Cu diffusivity between experimental observations and KMC simulation. The data of experiments 1 and 2 are taken from ref. [26] and [29], respectively.

temperatures ranging from 500 to 1400 K. After fitting the obtained temperature dependence of the Cu self-diffusivity with the Arrhenius expression (Equation 2.6), slight differences between the activation energies calculated for the low-temperature (500–800 K) and high-temperature (900–1500 K) regions were observed. The activation energy at low temperature is 0.67 eV, which is 0.2 eV lower than the high-temperature activation energy 0.87 eV. In addition, the obtained low-temperature activation energy values matched the lowest barrier energies of the periodical paths obtained in the previous section, suggesting that at low temperatures, one or several periodical paths with the lowest barrier energies determined the hopping behavior of Cu atoms, while the contribution of the pathways with higher barriers (which were calculated via Equation (2.13)) increased rapidly with increasing temperature.

Lastly, we compared the diffusion behaviors extracted from the KMC simulation with the experimental observations. Two independent experiments about the Cu diffusion in amorphous Ta_2O_5 thin film have been introduced in the previous Section 3.1.[26,29] The diffusivities evaluated from the experiments are shown in Figure 3.10(b), as well as the KMC simulation results in the same temperature range. In the first experiment, the Cu diffusivity at 200~500℃ was measured with secondary ion mass spectroscopy.[26] By fitting the measured data to the Arrhenius relation, the activation energy for Cu diffusion is estimated to be 0.64 eV, while the room temperature diffusivity is estimated to be 4.9×10^{-21} cm^2/s. In the other experiment, the Cu diffusivity in amorphous Ta_2O_5 film deposited by electron-beam was evaluated to be 10^{-13} cm^2/s from cyclic voltammogram measurements.[29] The discrepancy of about eight orders of magnitude in the room temperature diffusivity may be ascribed to the difference in the sample thickness and the structure of the deposited Ta_2O_5 film.[29] Though the large discrepancy between the two experiments makes the quantitative comparison with our simulation results difficult, we may be able to say that our KMC results are reasonable. Firstly, the low temperature activation energy obtained from KMC simulation, 0.67 eV, is close to the one estimated from the first experiment, 0.64 eV. Secondly, the room temperature diffusivity extrapolated from the KMC results, 5.7×10^{-17} cm^2/s, is in between the two experimental estimates.

3.5 Transferability of simplified NN potential

The construction and application of the simplified NN potential is describe in the above. However, the application of the constructed potential is still limited to the amorphous matrix utilized in the training procedure. It is desirable for the constructed NN potential to exhibit high transferability (when it can be used to study Cu diffusion in the amorphous Ta_2O_5 matrix with a significantly different atomic structure). To test the transferability properties of the NN potential, two additional amorphous structures were created using the melt quenching method. The initial structure corresponded to that of the amorphous Ta_2O_5 utilized as the matrix for the training structures, as shown in Figure 3.4. The melting temperature was set to 4000 K. One structure was melted for 1 ps, and the other one was melted for 10 ps (these two structures were named structure I and structure II, respectively).

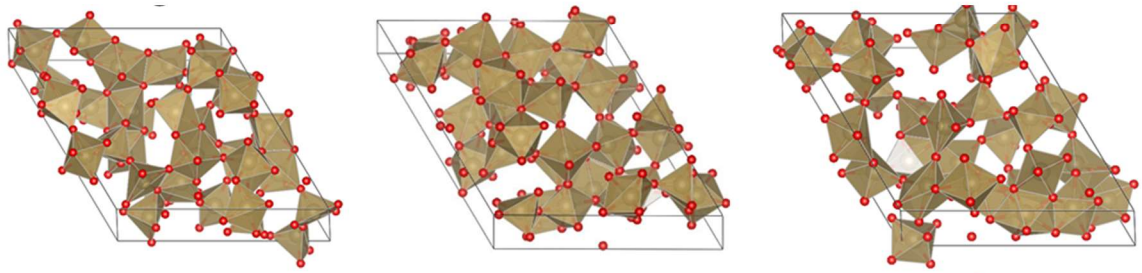

Figure 3.12 (a) The amorphous Ta_2O_5 matrix utilized in creating training database. (b) and (c) the amorphous Ta_2O_5 matrix I and II that created with melt quenching method using (a) as the initial structure. Matrix I was melted as 4000K for 1 ps and the matrix II was melted for 10 ps.

Subsequently, 50 test structures were created by randomly inserting Cu atoms into each matrix. The NN potential trained for the initial amorphous structure was used to predict Cu dissolution energies for all the test structures that were created from amorphous structures I and II. Figure 3.12 shows the correlation between the total energies of the test structures predicted using the NN potential and the corresponding DFT energies. The NN potential exhibited higher accuracy for the structures created from amorphous structure I as compared to those created from structure II, and their corresponding RMSE and MAE values were 0.117 eV and 0.071 eV, respectively.

The observed transferability of the utilized NN to amorphous matrix I can be explained by the use of symmetry functions for describing the atomic arrangement in the Cu local environment. To be more specific, the symmetry function values of two local environments are

very close when their atomic arrangements are similar (even if they are located in different matrices). In other words, the NN potential is expected to predict the Cu dissolution energy $E_{dissolution}$ for structures containing different matrices with a relatively high accuracy as long as similar Cu local atomic environments are used in the corresponding training structures. On the other hand, the NN potential may lose its ability to predict energy when the Cu local environment in the test structure is very different from those in all training structures (this may be the reason for the relatively poor performance demonstrated by the NN potential for amorphous matrix II).

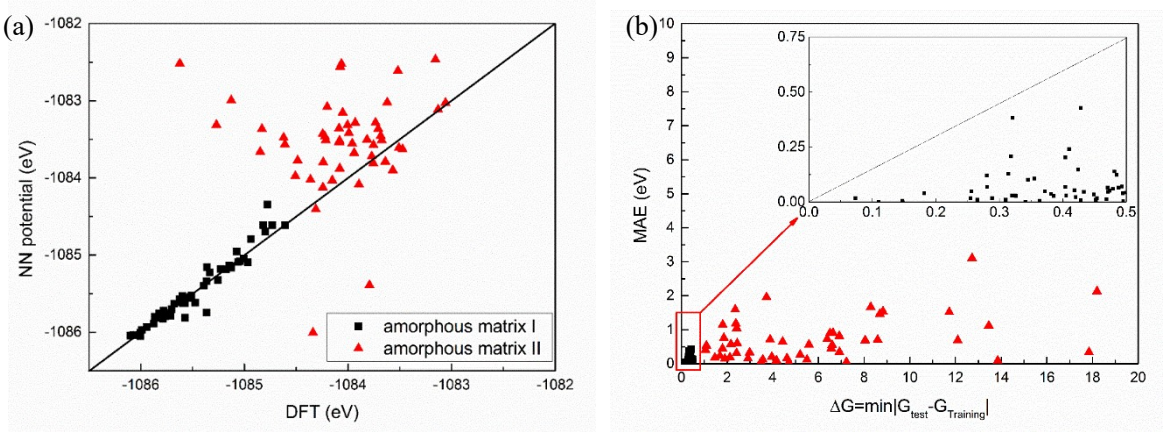

Figure 3.13. A correlation between the total energies of the test structures created from amorphous structures I and II (which were calculated using the NN potential) and the corresponding DFT reference values. (b) Transferability analysis of the utilized NN potential. The MAEs obtained for the energies calculated using the NN potential are plotted as functions of the nearest Euclidean distances between the symmetry function vectors of the test structures and those of the structures in the training set, $\Delta G = \min\left(\left|\overrightarrow{G_{\text{test}}}-\overrightarrow{G_{\text{training},\,i}}\right|\right)$. The test structures created from amorphous structures I and II are represented by the black squares and red triangles, respectively.

To perform a more comprehensive transferability analysis of the NN potential, the obtained MAE values were plotted as functions of the similarities of Cu local environments, which were represented by the formula $\Delta G = \min(|G_{\text{test}} - G_{\text{training},\,i}|)$ utilized for the nearest Euclidean distance between the symmetry function vector of the test structure and those of the structures in the training set. When ΔG is small, at least one training structure exists, in which the Cu local environment is similar to that of the test structure. As expected, the test structures with smaller ΔG exhibited smaller errors. The ΔG values calculated for the test structures of

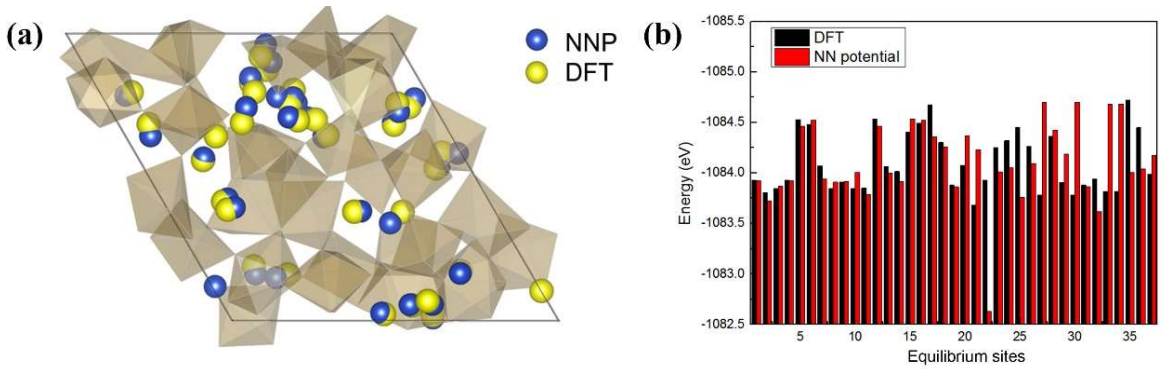

Figure 3.14: Test of NN potential transferability in searching metastable positions. The amorphous matrix II was used as host matrix. (a) 37 metastable positions found in the amorphous matrix II, using the same method introduced in the section 3.4.1. Then, those positions are further optimized with DFT. During the DFT optimization Cu displaced for 0.46 Å in average, while the maximum displacement is 1.3 Å. (b) Energies of equilibrium configurations obtained with NN potential and DFT respectively. The average error is 0.28 eV, while the maximum error is 1.29 eV.

amorphous phase I were much smaller than those obtained for amorphous phase II since the former were melted for a much shorter time, which allowed to retain a larger number of the structural features of the initial amorphous Ta_2O_5. The obtained analysis results also suggested a possible way to improve the transferability of the NN potential by including the training structures created from different amorphous matrices.

Finally, the transferability of NN potential was also examined for the Cu metastable positions and the energy profile along a diffusion path in the amorphous matrix II. By performing the same metastable position searching protocol as introduced in Section 3.4.1, 37 metastable positions were found in the amorphous matrix II. Then, these positions were further optimized with DFT. During the DFT optimization, Cu atoms were displaced by 0.46 Å in average, while the maximum displacement was 1.3 Å. The reliability of NEB calculation is tested in matrix II as well. The comparison of diffusion paths and energy profile between NN potential and DFT is shown in the Figure 3.14. Not surprisingly, the accuracy of NN potential in the amorphous matrix II, which is significantly different from the amorphous matrix utilized in training, is not good. However, the NN potential captures the characteristics of atomic diffusion in the test matrix rather well, though at several points the energy prediction error is

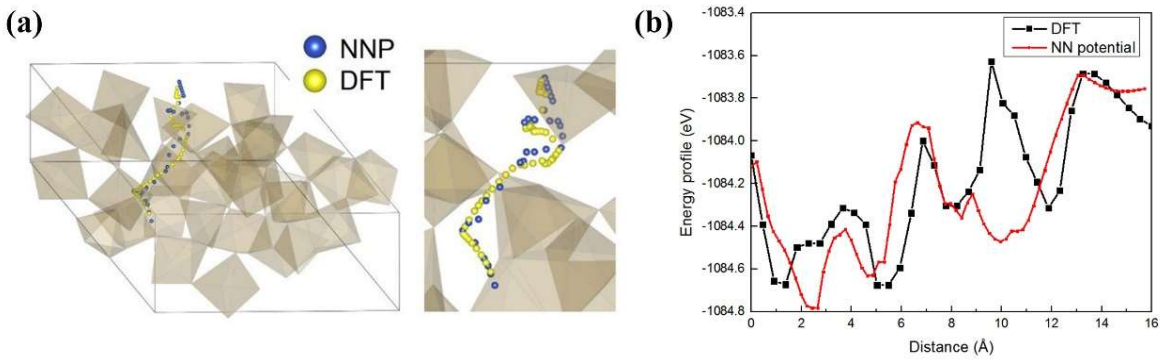

Figure 3.15: Test of NN potential transferability in the NEB calculation. A long diffusion path in amorphous II was chosen as an example. The length of the diffusion paths is about 16 Å. (a) Diffusion path indicated by the Cu transient positions, which were extracted from the NEB calculation. (b) Energy profiles along the diffusion path predicted by the NN potential and DFT respectively.

large. We expect that the transferability of the proposed method can be significantly improved by training the NN potential with a wide variety of the local environments of Cu atoms (which would require the use of various amorphous host matrices) and/or larger cutoff radii of the symmetry functions.

3.6 Advantages and disadvantages of simplified NN potential

The advantages of the simplified NN potential are as follows: 1) it is based on the multi-layer perceptron NN, which can be easily constructed using various open-source codes; and 2) the number of data sets required for training the NN is about 1~2 orders of magnitude smaller than that utilized for a typical ternary high-dimensional NN potential.

However, the proposed simplified method also has limitations. First, it cannot be extended to MD techniques because of the absence of atomic descriptions (especially forces acting on atoms) in the host matrix. Second, the transferability of the simplified NN potential was not very high (except for the cases with a very similar matrix structure). As illustrated in Section

3.5, the simplified NN potential captures rough characteristics in the calculation of metastable Cu positions, migration paths and migration energy barriers in a different amorphous matrix, but in some cases the errors are considerably large. The improvement of its transferability remains as future task.

On the basis of the above, we think that the NN potential method proposed in this chapter can be complementary to the high-dimensional NN potential in studying atomic diffusion. Highly reliable description of atomic diffusion behavior is possible by a well-constructed high-dimensional NN potential (the performance of high-dimensional NN potential will be shown in Chapter 4), while at least rough overview can be obtained by the present NN potential with much lower computational cost.

3.7 Summary

In this work, a simplified NN potential was developed to investigate the diffusion behavior of a single Cu atom in amorphous Ta_2O_5 structure. In contrast to the NN potentials that were used for describing binary and ternary systems in previous studies, the proposed technique was found to be much simpler, easier to use, and required much less training data. The reliability of the utilized NN potential was validated via energy predictions and NEB calculations. Its RMSE for energy predictions was equal to 23 meV/structure for the training set and 39 meV/structure for the testing set, and the NEB calculation results obtained for selected diffusion pathways were in good agreement with the DFT simulation data.

Using the developed NN potential, the equilibrium positions and diffusion paths of Cu atoms in the amorphous Ta_2O_5 structure were located and characterized. The obtained energy barriers of single-hop paths ranged between 0.01 and 1.79 eV. The lowest energy barrier determined for the periodical pathways connecting equilibrium interstitial sites and their equivalent sites in the adjacent supercells was 0.68 eV. This magnitude matched the Cu diffusion activation energy calculated from the Arrhenius plot of the low-temperature self-diffusivity values generated via KMC simulations (0.67 eV) as well as the number obtained from experimental observations (0.64 eV). The conducted KMC simulations also revealed that the Cu diffusion activation energy obtained at high temperatures (0.87 eV) was larger than the

magnitude calculated at low temperatures. Though the proposed simplified NN potential has disadvantages such as the inability to perform molecular dynamics simulations, it can be used as an important complementary technique, especially for studying atomic diffusion processes.

Chapter 4

Potential for Li Atom Diffusion in Amorphous Li_3PO_4

Li diffusion in amorphous Li_3PO_4 (*a*-Li_3PO_4) based electrolytes is an important phenomenon in nanoscale information and energy devices, such as all-solid-state battery[105] and recently developed nonvolatile memory device [106]. However, theoretical studies based on density functional theory (DFT) are limited by the high computational demand. In Chapter 3, we proposed a simple neural-network-based method that can be used to study the single atom diffusion in an amorphous matrix. The method can give accurate diffusion pathways and barrier energies. However, the transferability is limited. In the present study, we explored the applicability of high-dimensional neural network (NN) potentials developed by J. Behler *et al*[49] to the study of Li atom diffusion in *a*-Li_3PO_4, considering that their NN potential scheme has great transferability. The general ideal and construction procedure of Behler-scheme high-dimensional NN potential has been introduced in Section 2.3. The high-dimensional NN potential was used together with NEB, KMC and MD to characterize the diffusion paths, barrier energies, diffusion coefficient and effective activation energy. The results were compared with the corresponding DFT simulation, and show that NN potential can accurately reproduce the DFT results in studying the atom diffusion of amorphous. The computation speed of NN potential is 3~4 orders of magnitude faster than DFT. Lastly, structure and ion transport properties of *a*-Li_3PO_4 were studied with the NN potential using a large-scale model containing more than 1000 atoms. The preliminary results agree well with the experimental observation and might shed light on rvealing diffusion mechanism.

4.1 Background

4.1.1 Experimental characterization of amorphous Li_3PO_4

The Li_3PO_4 is intensively used as the electrolyte material of various thin-film electrochemical devices for its high ionic conductivity, low electronic conductivity and great chemical stability. The *a*-Li_3PO_4 thin film can be fabricated by RF sputtering, pulsed laser disposition (PLD) and rapid quench.

The structure of *a*-Li_3PO_4 thin film was systematically studied by Kuwata *et al*.[107] The thin films were deposited by PLD of Li_3PO_4 targets using an ArF excimer laser in different oxygen atmosphere bias from 0.1 to 10 Pa at room temperature. The local structure of *a*-Li_3PO_4 thin film was studied by Fourier transform infrared spectroscopy (FTIR) and Raman spectroscopy. From the FTIR spectroscopy (Figure 4.1(a)), it can be seen that the Li_3PO_4 film grown by the ArF excimer laser at 0.2 Pa shows five absorption peaks, which are located at 1170, 1038, 932, 750 and 586 cm^{-1}. The peaks at 1038 and 586 cm^{-1} can be attributed to the asymmetric stretching and asymmetric bending vibration modes of tetrahedral PO_4^{3-} units. The other three bands result from the $P_2O_7^{4-}$ units. The formation of $P_2O_7^{4-}$ units is due to the partial condensation reaction of Li_3PO_4 :

$$2Li_3PO_4 \rightarrow Li_4P_2O_7 + Li_2O \quad (4.1)$$

The additional Li_2O units were lost in the deposition procedure. The observation of Raman spectroscopy also agreed with the FTIR. As shown in Figure 4.1 (b), four peaks can be seen in the *a*-Li_3PO_4 thin film. Compared with the bulk polycrystalline Li_3PO_4, the spectroscopy of a-Li_3PO_4 has an additional weak peak at 750 cm^{-1}, which corresponds to the vibration of the P–O–P group.

Table 4.1: The conductivity and Li diffusion activation energies of amorphous lithium phosphate electrolyte films prepared by different methods. D_{Li} indicates the diffusion coefficient of Li atoms, $D\sigma$ is conductivity diffusion coefficient, which is calculated from conductivity σ with Nernst-Einstein equation.

Sample	Fabrication method	Properties	Measurement techniques	E_a(eV)	Reference
a-Li_3PO_4	PLD; ArF	D_{Li}	Ion-exchange, SIMS	0.58	[108]
a-Li_3PO_4	PLD; ArF	D_{Li}	Mask, SIMS	0.57	[108]
a-Li_3PO_4	PLD; ArF	D_σ	impedance spectroscopy	0.55	[108]
a-Li_3PO_4	PLD; ArF	σ	impedance spectroscopy	0.58	[107]
a-Li_3PO_4	PLD; ArF	σ	impedance spectroscopy	0.57	[134]
a-Li_3PO_4	PLD; YAG	σ	impedance spectroscopy	0.60	[134]
a-Li_3PO_4	RF sputtering	σ	impedance spectroscopy	0.68	[36]

Due to the loss of Li_2O units, the composition of *a*-Li_3PO_4 thin film was slightly changed from the stoichiometric value. From the inductively coupled plasma atomic emission spectroscopy (ICP-AES) analysis, the Li/P atomic ratio of the Li_3PO_4 film grown by the ArF excimer laser at 0.2 Pa O_2 was estimated to be 2.9. The Li/P atomic ratio measured here has been used as important structural information when we constructed the large-scale *a*-Li_3PO_4 model (see Section 4.5.1).

The Li diffusion coefficient and the ionic conductivity in the *a*-Li_3PO_4 thin film can be measured by different techniques. The impedance spectroscopy is frequently used to measure the ionic conductivity of electrolyte materials. The ionic conductivity was determined from the

frequency-independent plateau in the impedance spectra. Recently, the Li diffusivity in the *a*-Li_3PO_4 was measured using the ion-exchange and SIMS techniques.[108] In Table 4.1, the activation energy of Li diffusion and ionic conductivity measured with different experimental methods are listed. From the table, we can found that the Li diffusion activation energy is related to the fabrication method of thin film. The film fabricated with PLD has a diffusion activation energy of 0.55~0.60 eV, while the activation energy of RF sputtering film is higher (0.68 eV).

4.1.2 Theoretical research about crystalline Li_3PO_4

The structural, electronic, atomic diffusion properties of two well-characterized crystalline Li_3PO_4 forms, which labeled as β- and γ-Li_3PO_4, were systematically investigated by Y. Du *et al*, with first-principles calculation. Crystalline γ-Li_3PO_4 has the orthorhombic *Pnma* structure, while the β-Li_3PO_4 has the orthorho mbic *Pmn2* structure. Figure 4.2(a) shows the structure of β- and γ –Li_3PO_4. The lattice constants extracted from first-principles calculation are in good agreement with the experimental observation for both crystals. In addition, the first-principles calculation shows that the β-Li_3PO_4 is energetically more favorable compared with the γ-Li_3PO_4. However the energy difference is small, that is ΔE_β-ΔE_γ = 0.01 eV per Li_3PO_4 unit. The partial density of states (DOS) calculated with first-principles calculation are shown in Figure 4.2(b). The two crystalline forms have similar DOS properties. For both materials, the band gaps are about 6 eV. The values are smaller than the experimentally measured one, 8 eV. Such band-gap underestimation can be attributed to the well-known problem of density functional theory using the local/semi-local approximation.

Migration energy barriers of Li vacancy and Li interstitials were studied using the NEB method based on first-principle calculation (LDA approximation). For the vacancy migration, the lowest diffusion barriers were estimated to be 0.62 eV and 0.55 eV for γ and β-Li_3PO_4, respectively. The interstitialcy diffusion mechanism of Li_3PO_4 involves the concerted motion of two Li atoms. During the interstitialcy migration process, an interstitial Li ion kicks out and replaces a neighboring Li of the host lattice, while the “kicked-out” Li ion takes an equivalent interstitial site. From the NEB calculation, the lowest migration barriers for the Li interstitial were found to be 0.29 and 0.39 eV for the γ and β-Li_3PO_4, respectively. These results indicate that the interstitial ion processes are considerably more efficient for ion transport than the

vacancy transport processes in these materials.

4.1.3 Research objective

The Li_3PO_4, as an important electrolyte material, has been intensively studied both experimentally and theoretically. However, there is little published information about the structural and atomic diffusion properties of *a*-Li_3PO_4. Since the high-dimensional neural network (NN) potentials proposed by J. Behler can achieve high accuracy and good transferability, and a recently published work shows that the high-dimensional NN potential can be successfully used in the study of defects diffusion on the surface of crystalline copper[59], this method seems suitable for studying the structural and atomic diffusion properties of *a*-Li_3PO_4. However, the structure variety in the amorphous materials is much more complicated than that in the crystal, and so it is still unclear how accurate the high-

dimensional NN potential can be when it is applied to the diffusion properties in the amorphous materials. Therefore, in this research, the structural and atomic diffusion properties of *a*-Li_3PO_4 will be investigated with the high-dimensional NN potential. At the same time, the results are carefully compared with the corresponding DFT simulation to show that the NN potential can accurately reproduce the DFT results in studying the atom diffusion of amorphous. For clarity, the "high-dimensional neural network potential" will be referred as "neural network potential" or "NN potential" in this chapter.

The outline of this chapter is as follow. Section 4.2 introduces the details of constructing the NN potential for Li_3PO_4. The performance of the NN potential in energy prediction is introduced in Section 4.3. In Section 4.4, the NN potential is used to characterize the Li diffusion mechanism in a small size *a*-Li_3PO_4 model together with nudged elastic band, kinetic Monte Carlo, and molecular dynamics. The results of NN potential are carefully compared with the DFT results. In Section 4.5, NN potential is used to construct a large-scale model of *a*-Li_3PO_4, and examine the Li diffusion coefficient in it. The obtained conclusions are provided in Section 4.6.

4.2 Construction of neural network potential

4.2.1 DFT calculation for reference energies

Same as in Chapter 3, a reference database, which contains reference structures and corresponding DFT energies, is needed in optimizing the parameters (or weights) of NN potentials. All the reference DFT energies of reference structures were calculated with Vienna ab initio simulation package (VASP)[109,110]. The projector augmented wave (PAW) method was adopted to treat atomic core electrons, while the Perdew-Burke-Ernzerhof functional within the generalized gradient approximation was adopted to describe the electron-electron interactions.[101],[111] The training structures have variable size containing up to 64 atoms. The setting of cutoff energy (for the plane wave basis set) and *k*-point mesh were set so that the convergence of the total energy within 1 meV/atom was achieved. Specifically, the cutoff energy was set to 700 eV, and the 4 × 4 × 4, 4 × 4 × 2 and 4 × 2 × 2 *k*-point meshes were

adopted for the supercells having 15~16, 29~32 and 61~64 atoms, respectively.

The database for the training of the NN potential included the following three kinds of data: 1) Snapshots taken directly from the molecular dynamics trajectories at various temperatures from 300K to 4000K; 2) Defective structures created by just removing one Li atom or one Li_2O unit randomly from the MD snapshot structures; 3) NEB intermediate images obtained using a roughly trained NN potential. The structures of the third kind were included in the training dataset since we applied the NN potential to the investigation of diffusion paths. Since in an MD trajectory a Li atom spends most of the time vibrating around an equilibrium site and only a small fraction of the time around the saddle points between the neighboring equilibrium sites, the first and second structures might contain very limited information related to transient structures around the saddle points which govern the diffusion behaviors. More specifically, the data of the third kind were obtained as follows: firstly, a rough NN potential was trained with the MD snapshots and defective structures; then, the NEB calculations were performed with the rough NN potential to obtain the Li vacancy diffusion paths in other amorphous structures. At last, the intermediate images, especially those close to the saddle points, were added into training database. The transient structures are of great significance in obtaining an accurate potential. The detailed discussion will be given in Section 4.4.

In total 38592 structures were created. These structures were randomly distributed into the training and testing sets. The training set contains 30874 (~80 %) structures, while the remaining 7718 (~20%) structures were used as the independent testing data.

4.2.2 Construction of neural network potential

As introduced in the Section 2.3, the basic idea of NN potential is: the total energy of a structure can be expressed as the sum of energy contributions of respective atoms, and the each energy contribution can be predicted by the NN according to the local atomic environment of the atom. The local atomic environment can be described with radial and angular symmetry functions. The functional formula of frequently used symmetry functions are given with Equation 2.45 ~ 2.49. In this research the G^2-type radial symmetry functions (Equation 2.46) and G^5-type angular symmetry functions (Equation 2.49) were adopted.

4.2.3 Simplification of neural network potential

Table 4.2 The requisite symmetry function types for the high-dimensional NN potentials that constructed for the unitary, binary and ternary system. The different elements are represented by letters A, B and C.

System	Elements	Types of radial symmetry functions			Types of angular symmetry functions						Total number
Single-element	A	A-A			A-AA						**2**
Binary	A, B	A-A	A-B		A-AA	A-BB	A-AB				**10**
		B-A	B-B		B-AA	B-BB	B-AB				
Ternary	A, B, C	A-A	A-B	A-C	A-AA	A-BB	A-CC	A-AB	A-AC	A-BC	**27**
		B-A	B-B	B-C	B-AA	B-BB	B-CC	B-AB	B-AC	B-BC	
		C-A	C-B	C-C	C-AA	C-BB	C-CC	C-AB	C-AC	C-BC	

A very severe disadvantage of high-dimensional NN potential is its applicability in systems containing a large number of different chemical elements. This problem arises from the rapidly increasing structural variety with the number of elements, which demands too many symmetry functions for the unambiguous description. This trend can be seen in Table 4.2, in which the requisite symmetry function types in the single-element, binary and ternary system are listed. In a single-element system, only one species exists in the neighboring environment of an atom, and thus only one kind of radial symmetry functions A-A (the first letter indicates the central element, and the letters after the dash represents the neighboring elements) and one kinds of angular symmetry functions A-AA (the first letter denotes the central element and the two letters after the dash do the elements of the neighboring atoms) are needed in the atomic NNs. However, in multi-component materials, different species in the neighboring system exists in the local environment of one atom, and the presence of different species should be treated separately. For instance, in Li_3PO_4, a lithium atom can have other lithium atoms, phosphorous atoms and oxygen atoms in its local atomic environment. Thus, for each species, we must employ a set of radial symmetry function for each of three possible neighboring elements, and a set of angular symmetry function for each two-two combinations of three elements. This yields 3 types of radial set and 6 types angular set for each element, 27 kinds of symmetry functions in total. Obviously, the amount of symmetry function types increases rapidly with respect to the number of species. For the quaternary and quinary system, the

number will increase to 56 and 100. In these cases, hundreds, or even more than a thousand, of structural descriptors must be used, which results in the very complex NN architectures. For this reason, the application of NN was restricted in the system with four elements at largest so far.[57]

Under the above situation, simplification of the atomic symmetry function would be worth exploring. We tried this when we constructed the NN potential for Li_3PO_4. Our idea is to omit some types of angular symmetry function that seem physical much less important. To be more

Table 4.3: The RMSEs of the NN energies obtained for the training set and the testing set of the Li_3PO_4 system using different input symmetry function sets. Further, the number of parameters in the NN potential is given for each architecture.

	Species	Types of angular symmetry function set						Network	No. of Parameters	RMSE (meV/atom)	
										Training	Testing
	Li	Li-LiLi	Li-PP	Li-OO	Li-LiP	Li-LiO	Li-PO	156-15-15-1			
1	P	P-LiLi	P-PP	P-OO	P-LiP	P-LiO	P-PO	156-15-15-1	7833	4.9	5.7
	O	O-LiLi	O-PP	O-OO	O-LiP	O-LiO	O-PO	156-15-15-1			
	Li	Li-LiLi	Li-PP	Li-OO				90-15-15-1			
2	P	P-LiLi	P-PP	P-OO				90-15-15-1	4863	5	5.5
	O	O-LiLi	O-PP	O-OO				90-15-15-1			
	Li							24-15-15-1			
3	P	P-OO						46-15-15-1	2553	5.7	6
	O	O-PP						46-15-15-1			
	Li	Li-OO						46-15-15-1			
4	P	P-OO						46-15-15-1	**3213**	**5**	**5.6**
	O	O-LiLi	O-PP					68-15-15-1			
	Li							24-15-15-1			
5	P							24-15-15-1	1893	8.3	8.6
	O							24-15-15-1			

specific, we considered the following features of bonding in the Li_3PO_4: P atoms tend to bond with four neighbor O atoms and form phosphates ($PO4^{3-}$) with the shape of tetrahedron, while Li and O atoms tend to form the Li_2O unit. These P-O and Li-O covalent bonds have specific angular preference. Based on these structure characteristics in Li_3PO_4, we used only four types of angular symmetry function sets, *i.e* P – O O， O – P P， Li – O O and O – Li Li while keeping all the radial symmetry function sets in constructing the NN potential. In fact, we examined several choices of angular symmetry function sets. In the examination, NN potentials based on different symmetry function sets were trained with the Broyden–Fletcher–Goldfarb–Shanno (BFGS) algorithm,[111] using the training set as reference data, while the testing set was used to validate them. The parameters for radial and angular symmetry functions are shown in appendix. Table 4.3 shows the lowest root mean squared errors (RMSE) of energy prediction of the constructed NN potentials. Note that for each kind of NN potential, we repeated the training 10 times to get the best fitting. As seen in Table 4.3, compared with the NN potential having no angular symmetry function as inputs (No. 5), the NN potentials constructed using the angular symmetry function sets have clearly improved accuracy. On the other hand, the difference in the degree of accuracy is hardly seen among NN potentials with different choices of angular symmetry function sets (No. 1 to No. 4). The results shown in Table 4.3 suggests that to describe the characteristics of P-O and Li-O band angles is of great significance in constructing accurate NN potential, while the description of the rest of angular symmetry function sets are much less important. Meanwhile, the use of simplified input symmetry function sets reduces the number of input nodes, which leads to the significant reduction of the total amount of parameters in NN potential.

Although this is just a preliminary attempt to simplify the NN potential, our idea successfully reduced the size of input symmetry function set without severe loss in accuracy. We think this idea could be a promising solution to solve the dilemma of NN potential in the complex materials with many species. Of course, this approach has a limitation as well. Though in the case of Li_3PO_4, we can easily recognize the structural feature and corresponding important symmetry function sets, this may not always be possible for other material systems. Another idea/approach should be explored in such cases if the simplification of NN potential is desirable.

On the basis of the comparison shown in Table 4.3, we adopted the simplified input symmetry function set No. 4 in the construction of the NN potential. The atomic NN for each

species has two hidden layers with 15 hidden nodes in each layer. The hyperbolic tangent activation functions are employed at the nodes of the two hidden layers, and a linear activation function is employed at the output node. Consequently the NN potential contains 3123 parameters in total.

4.3 Neural network potential

4.3.1 Energy prediction

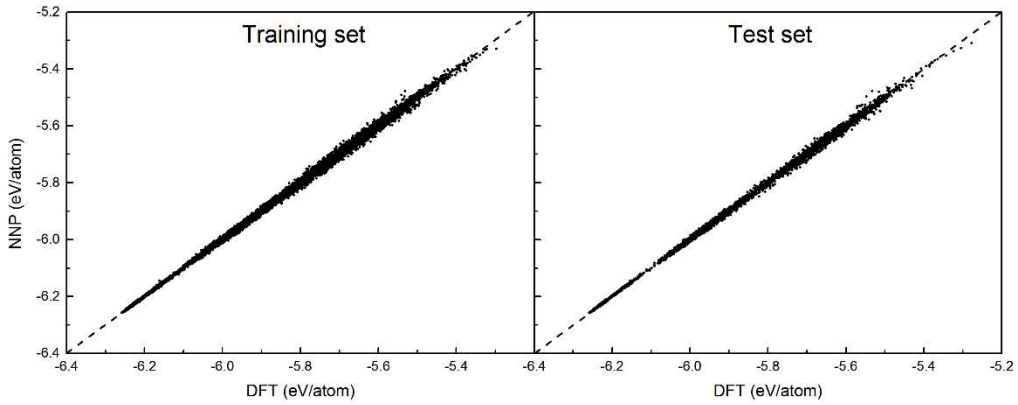

Figure 4.3: A comparison between the total energies of the training set and testing set structures obtained using the DFT and NN Potential. (a) training set; (b) testing set

In Figure 4.3, the energies predicted by the NN potential were plotted against DFT energies. As mentioned above and shown in Table 4.3, the residual mean square error (RMSE) of the energy prediction is 5.0 meV/atom for the training set and 5.6 meV/atom for the testing set. However, verifying the NN potential with the testing set might be problematic for the following two reasons. Firstly, the structures from the testing set might be highly correlated with those in training set due to the inclusion of continuous MD trajectories in the training database. Secondly, the prediction capacity of the NN in structures having much larger supercells is unclear since all the testing structures have relatively small supercells. Considering the above, we performed another verification test with data obtained using a totally

different structure: 500 steps MD trajectory of $Li_{48}P_{16}O_{64}$ at 4000 K. The size of these testing structures is twice larger than the largest training structures, and these data are not correlated at all with any of the training structures. The comparison between DFT and NN potential energies were shown in Figure 4.4. The RMSE of energy prediction is 6.2 meV/atom, which is similar to the error in the training and testing sets. The verification test further proved the accuracy of energy prediction and demonstrated its transferability to larger structures.

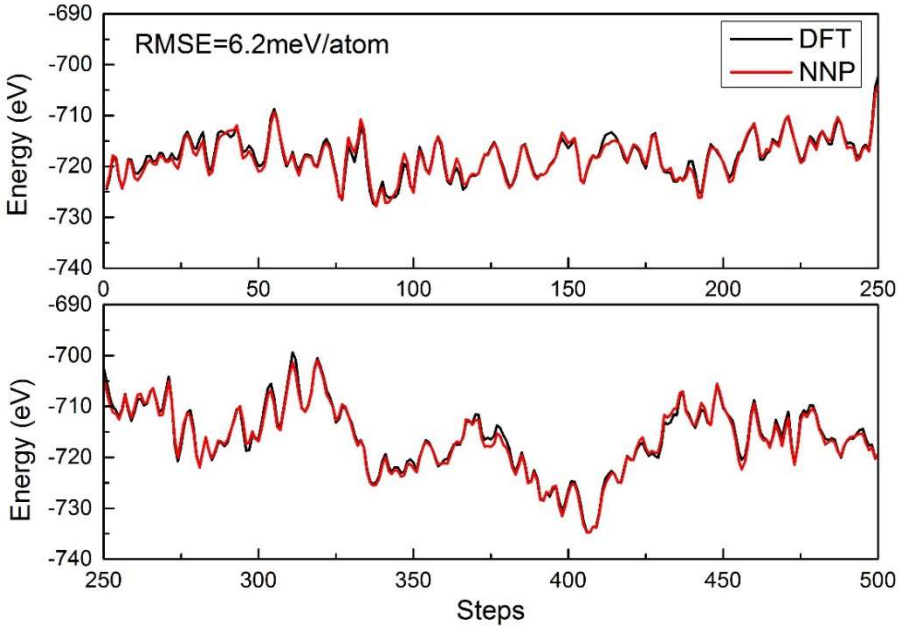

Figure 4.4: Comparison of density functional theory (DFT) and neural network potential (NNP) along a molecular dynamic trajectory. The structure contains 128 atoms and none of structures are included in the training set. The residual mean square error (RMSE) of NNP is 6.2 meV/atom.

4.3.2 Crystal structure parameters

The first application of NN potential was the characterization of the two most important crystal phase of Li_3PO_4, which labeled by β and γ. The crystalline γ-Li_3PO_4 has the orthorhombic *Pnma* structure, while the crystalline β-Li_3PO_4 has the orthorhombic *Pmn2* structure. Table 4.4 lists the lattice constants obtained from DFT (GGA, PBE) calculations, NN potential calculations and experiments. The lattice constants obtained by the NN potential are highly consistent with those by the DFT and experiments (the relative error does not exceed

1%). The total energies calculated by the NNP and DFT also agree with each other well. In agreement with DFT, the NN potential calculations show that the β form is energetically more favorable than the γ form. The energy difference per Li_3PO_4 unit between the β and γ forms, $E_\gamma - E_\beta$, is 0.01 eV for the DFT and 0.03 eV for the NN potential.

Table 4.4: Comparison of the lattice parameters and total energy of β and γ Li_3PO_4 crystal structures obtained with NN potential, DFT and experimental measurement.

	NNP		DFT		Expt.
	Energy (eV)	Lattice constant (Å)	Energy (eV)	Lattice constant (Å)	Lattice constant (Å)
γ- Li_3PO_4	-200.963	a = 5.003	-200.935	a = 5.001	a = 4.927
		b = 6.108		b = 6.177	b = 6.120
		c = 10.502		c = 10.615	c = 10.490
β- Li_3PO_4	-100.491	a = 4.914	-100.484	a = 4.923	a = 4.856
		b = 5.287		b = 5.298	b = 5.240
		c = 6.164		c = 6.177	c = 6.115

The first application of NN potential was the characterization of the two most important crystal phase of Li_3PO_4, which labeled by β and γ. The crystalline γ-Li_3PO_4 has the orthorhombic *Pnma* structure, while the crystalline β-Li_3PO_4 has the orthorhombic *Pmn2* structure. Table 4.4 lists the lattice constants obtained from DFT (GGA, PBE) calculations, NN potential calculations and experiments. The lattice constants obtained by the NN potential are highly consistent with those by the DFT and experiments (the relative error does not exceed 1%). The total energies calculated by the NNP and DFT also agree with each other well. In agreement with DFT, the NN potential calculations show that the β form is energetically more favorable than the γ form. The energy difference per Li_3PO_4 unit between the β and γ forms, $E_\gamma - E_\beta$, is 0.01 eV for the DFT and 0.03 eV for the NN potential.

4.4 Performance of neural network potential in studying atomic diffusion

4.4.1 Structural model for this study

In this section, we test the reliability of the NN potential in atomic diffusion behaviors. For this purpose, we examined diffusion behaviors by combining the NN potential with various computational approaches, i.e. NEB, KMC and MD, and then compared the results with those obtained by the combination of these approaches with DFT. All computations were carried out using an *a*-Li_3PO_4 structure created with the typical melt quenching method: The γ-Li_3PO_4 structure (containing 32 atoms) was melted and equilibrated for 15 ps at 6000 K, then quenched to 300 K at the rate of 1 K/fs. At last, the structure was equilibrated for 3 ps at 300 K. The aforementioned process was performed with *ab-initio* MD. This *a*-Li_3PO_4 structure was further relaxed with NN potential and DFT until the maximum force acting on atoms became less than 0.01 eV/Å to obtain the final models for the NN potential and DFT simulations, respectively.

The two final structures are almost the same: The discrepancy in the atomic positions between the two is 0.02 Å on average and 0.05 Å at a maximum. The total free energy is -200.93 eV in the model for the NN potential, while -200.90 eV for DFT. The final model for the DFT is shown in Figure 4.5.

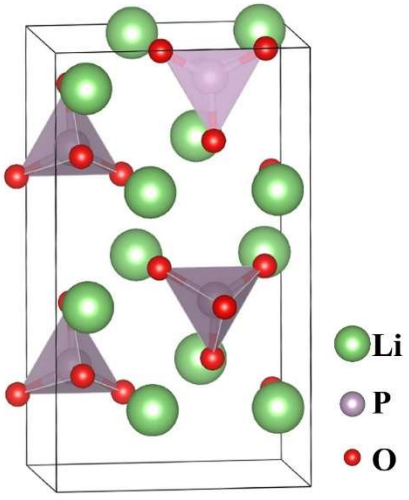

Figure 4.5: The final structure of Li_3PO_4 after melt quenching simulation. The structure was fully optimized with DFT.

It should be noted that these models are partially crystallized after the annealing and relaxation procedures, and thus are not fully relevant to represent the structure of *a*-Li_3PO_4 synthesized experimentally via *e.g.* the pulsed laser deposition technique. However, we call these models "amorphous" for simplicity. To construct a more reasonable model of *a*- Li_3PO_4 requires the use of much a larger supercell and a slight different composition. The structure of *a*-Li_3PO_4 will be discussed in Section 4.5.

4.4.2 Vacancy formation energy

The vacancy formation energy was defined as,

$$E_f = E\left[O_{Li}\right] - E\left[bulk\right] + \mu_{Li}, \tag{4.2}$$

in which $E[O_{Li}]$ is the total energy of the supercell containing one Li vacancy, $E[bulk]$ is the total energy of the disordered Li_3PO_4 supercell, and μ_{Li} is the chemical potential of Li obtained from DFT calculation of a perfect Li *bcc* crystal. The supercells with a vacancy have been generated by removing a Li atom, and then relaxed the structure. Since the supercell contains 12 Li atoms that are not equivalent to one another, we can obtain 12 different Li vacancy formation energies. Figure 4.6 shows the comparison of the vacancy formation energies between DFT and NN potential. The average disagreement is 0.029 eV, and the maximum is 0.040 eV. The final vacancy structures relaxed by DFT and NN potential were also quite similar.

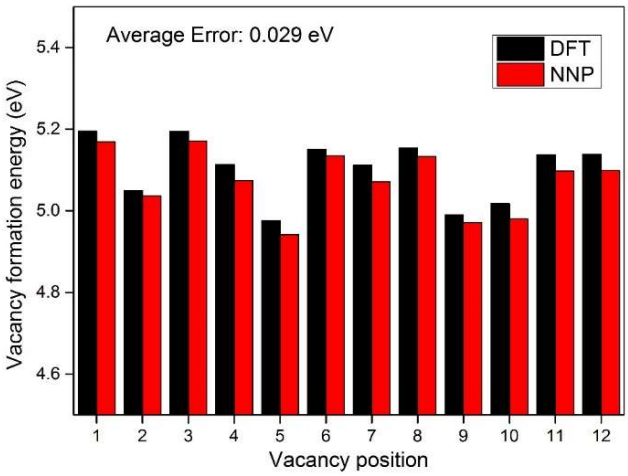

Figure 4.6: Li vacancy formation energies in the Li_3PO_4 model calculated by density functional theory (DFT) and neural network potential (NNP).

The average and maximum differences in atomic positions are about 0.03 Å and 0.08 Å, respectively.

It should be noted that the large formation energies (～5 eV) obtained here means very small probability of formation of Li vacancy. In reality, a vacancy-interstitial pair would be formed rather than an isolated vacancy. Since the purpose of this section is the verification of the applicability of the NN potential in various calculations, we do not discuss the cases with complex defects here.

4.4.3 Diffusion paths and network

Here we examine the Li vacancy diffusion network (including the Li migration paths, barrier energies and the topology connection of paths) using the nudged elastic band (NEB)

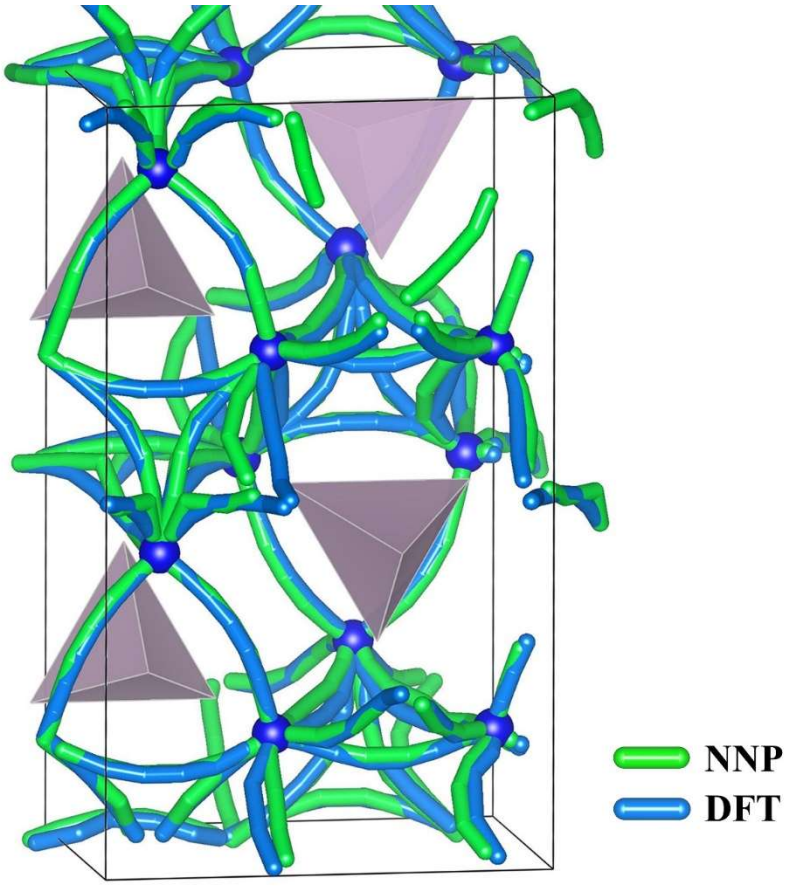

Figure 4.7: All diffusion paths of Li atom in the Li_3PO_4 model, predicted by density functional theory (DFT) and neural network potential (NNP) with nudged elastic band (NEB) method.

method, which is introduce in Section 2.1.2. The images optimization can be based on the potential energy surface provided by DFT calculation or classical interatomic potential (e.g. NN potential).

In the present study, we assumed that a Li atom can directly hop to the neighboring vacancy site when the distance between the two sites is shorter than 3.5 Å. Then, we obtained a Li diffusion network comprising 46 individual migration paths in the disordered Li_3PO_4 model. Each of these paths was characterized by the NEB calculation (based on either NN potential or DFT). The location and shape of these migration paths are shown in Figure 4.7. As we can see, the diffusion paths predicted by the two methods agree well with each other.

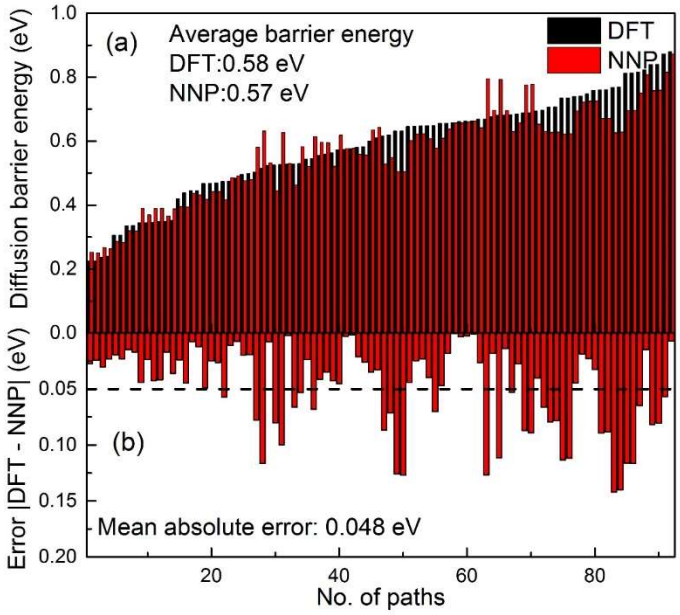

Figure 4.8: Comparison of barrier energies of 92 diffusion paths in Li_3PO_4 model calculated by density functional theory (DFT) and neural network potential (NNP). (a) The barrier energies obtained by NNP and DFT; (b) The difference of activation energies.

Figure 4.8 gives the comparison of activation energies obtained by the NN potential and DFT. The average barrier energy is 0.58 eV in the DFT calculation, while 0.57 eV in the NN potential. The prediction error of barrier energies is 0.048 eV in average, which is about 8 % compared with the average barrier energy.

Here we would like to emphasize that to achieve a high accuracy in predicting barrier energies, it is necessary to include Li diffusion transient structures (introduced in Section 4.2.1)

into the training database. The NN potential constructed without using the transient structures gave the average error of barrier energies of 0.08 eV, though the energy prediction accuracy is not bad (RMSE: 5.2 meV/atom for the training set; 5.8 meV/atom for the testing set). The detailed information is provided in the appendix.

4.4.4 Kinetic Monte Carlo simulation

To evaluate the realistic atomic diffusion coefficients as well as the effective activation energies for diffusion, kinetic Monte Carlo (KMC) simulations are often performed using the information of the diffusion networks obtained from NEB calculations. So we performed KMC simulations employing the two Li diffusion networks, obtained with DFT and NN potential respectively, to check the validity of the NN potential further. As introduced in chapter 2 (Section 2.1.3), the probability for the Li atom hopping from the site *i* to the neighboring vacancy site *j* was determined using the harmonic transition state theory (Equation 2.13). The value of atomic vibration frequency *v'* is assumed to be 10^{13} s^{-1} for all Li atoms, and ΔE_{ij} is the barrier energy of Li vacancy migration computed with NEB.

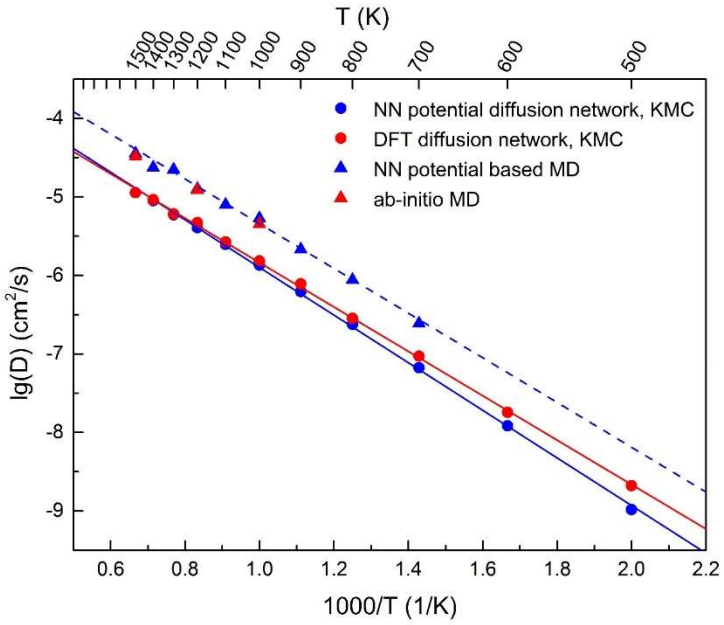

Figure 4.9: Temperature dependence of Li diffusion coefficient obtained from kinetic Monte Carlo simulation and molecular dynamic simulation. The diffusion network topology and hopping possibility obtained from previous NEB calculation were used as prior parameters of KMC simulation.

The KMC simulations were run at different temperatures from 500K to 1500K. For each simulation, 100 million MC events were performed. The statistically averaged mean square displacement (MSD) along the KMC simulation is calculated according to Equation 2.4. Afterward, the diffusion coefficient *D* can be evaluated based on the Einstein relation (Equation 2.5).

Figure 4.9 shows the temperature dependence of Li diffusion coefficients in the Li_3PO_4 model, and the overall diffusion obeys an ideal Arrhenius behavior. By fitting the plots with straight lines, the effective diffusion activation energies of Li vacancy diffusion are estimated as 0.60 eV for NN potential, and 0.56 eV for DFT.

4.4.5 Molecular dynamics simulation

We performed molecular dynamics with vacancy Li_3PO_4 model ($Li_{11}P_4O_{16}$) at 800 K, 1000 K, 1200 K and 1500K. All these MD simulations used the same initial structure, which is an optimized amorphous vacancy model obtained in Section 4.4.2. The simulation was performed

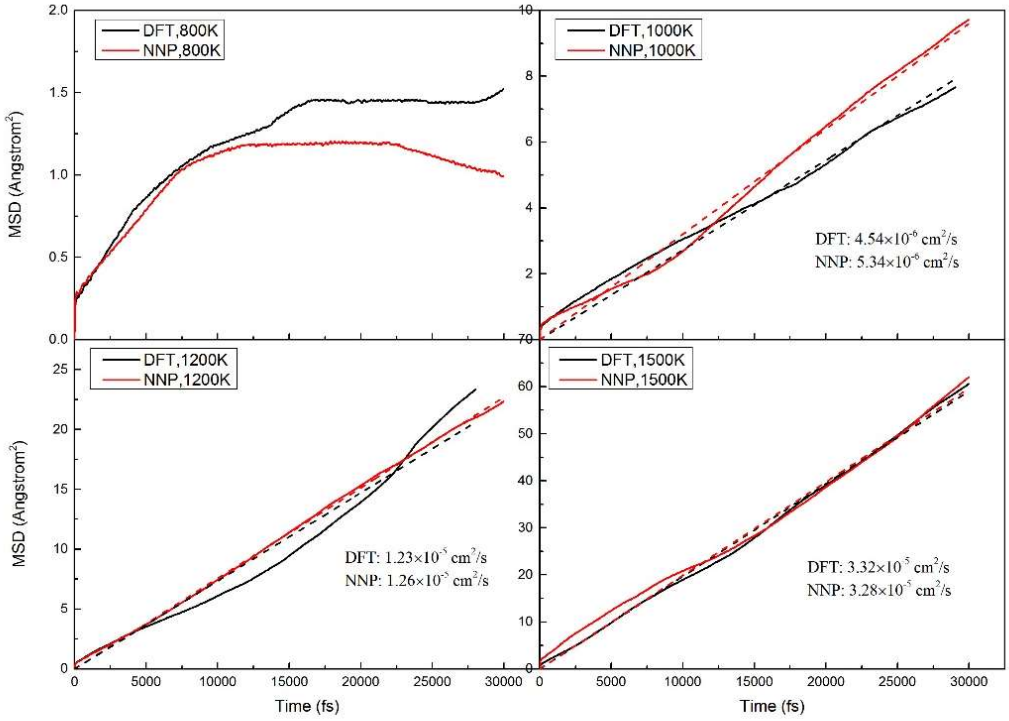

Figure. 4.10: Average mean square displacement along the molecular dynamic trajectory at 800K, 1000K, 1200K and 1500K.

with the canonical ensemble (NVT) using the Verlet algorithm. Each molecular dynamics trajectory last for about 60 ps, and each MD step corresponds to 2fs. The averaged mean squared displacements (MSDs) [112] of Li atoms at different temperatures are shown in Figure 4.10. According to the Einstein equation (Equation 2.5), the diffusion coefficient can be directly obtained from the slope of MSD plot. From Figure 4.11, we can see that MSDs of Li ions increase almost linearly with time at 1000K, 1200K and 1500K. On the other hand, the MSD plot of 800K deviates from the linear relationship considerably, which may be due to the low temperature and short simulation ti me. The Li diffusion coefficients extract from the NN potential trajectories are 5.34×10^{-6} cm^2/s at 1000 K, 1.26×10^{-5} cm^2/s at 1200 K and 3.32×10^{-5} cm^2/s at 1500 K, while those from ab-initio molecular dynamics trajectories are 4.54×10^{-6} cm^2/s at 1000 K; 1.23×10^{-5} cm^2/s at 1200 K and 3.28×10^{-5} cm^2/s at 1500 K. Except the 800K case, for which the effective diffusion coefficients cannot be extracted from the MD simulations, the Li diffusion coefficients determined from the NN potential MD simulations are in good agreement with the DFT results.

In order to further confirm the agreement between the NN potential and DFT in the MD simulations, we calculated the total radial distribution functions averaged over the MD trajectories at respective temperatures, which are shown in Figure 4.11. As can be seen in this figure, there are only slight discrepancies between radial distribution functions obtained from the NN potential and DFT simulations.

The calculation speed of the NN potential MD is much faster than the ab-initio MD. For example, generating a trajectory described above takes about 96 hours on 192 cores (Intel® Xeon® processor L5640) in the case of ab-initio method, while it takes only 4.5 hours on a single core of the same processor in the case of the NN potential. That is, the calculation speed of NN potential MD simulations is about 4000 times faster than the ab-initio ones.

Finally, we carried out long time MD simulations (1ns per trajectory) to obtain reliable Li diffusivities. The results were plotted in Figure 4.10 together with the KMC results, and the mean squared displacements of Li along these trajectories are shown in the appendix. As can be seen from Figure 4.10, the temperature dependence of the evaluated Li diffusivities obeys the Arrhenius law. The effective activation energy for diffusion obtained from the linear fitting of Arrhenius law is 0.59 eV for the MD results with the NN potential, which qualitatively agrees with our KMC simulation results using the same NN potential. The quantitative difference in the diffusion coefficients seen in Figure 4.10 between the MD and KMC can be

attributed to the jump frequency used in our KMC simulations: The same value of 10^{13}/s was set to the jump frequencies of all the transitions, which must be a very crude approximation.

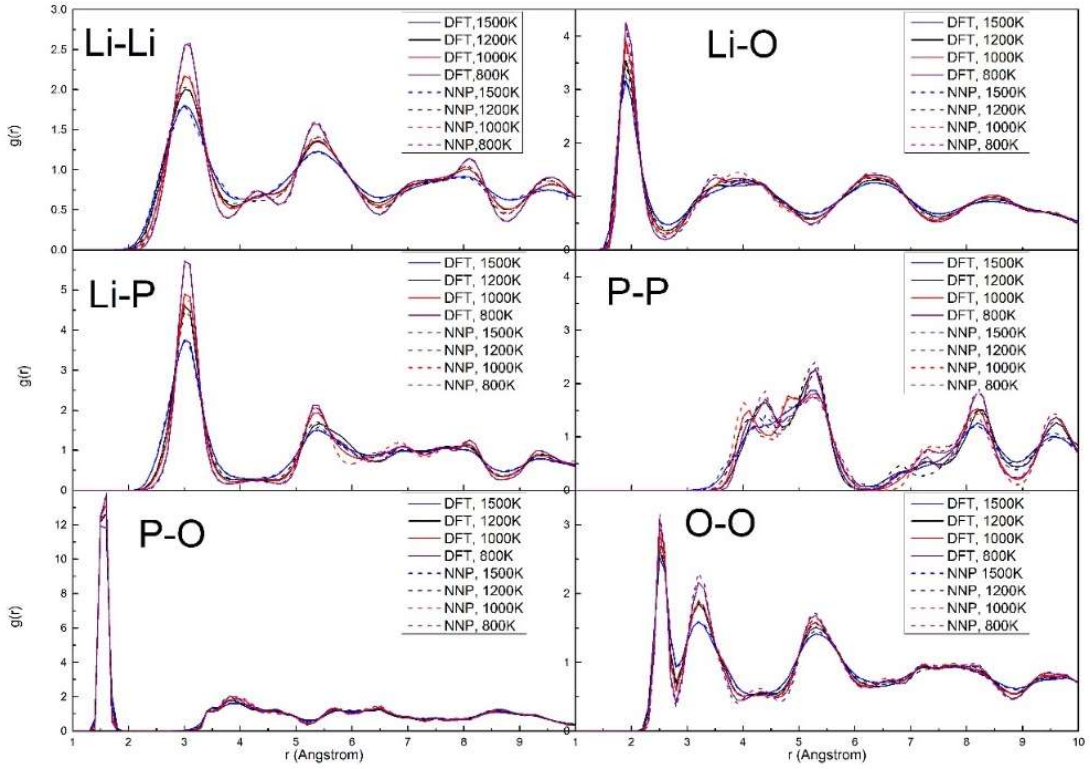

Figure 4.11: The partial radial correlation function of Li_3PO_4 averaged over the 60 ps MD trajectory at different temperatures.

4.5 Large-scale simulation of Li diffusion in amorphous Li_3PO_4

4.5.1 Amorphous Li_3PO_4 structure

By means of DFT calculation, the structure and properties of crystalline Li_3PO_4 and LiPON have been studied[113–116], but the theoretical researches on amorphous Li_3PO_4 are still scarce. We used the NN potential developed in the present work to construct large-scale *a*-Li_3PO_4 models. According to the experimental measurements introduced in the background

(Section 4.1.1), the composition of Li_3PO_4 thin film fabricated by pulsed laser deposition is often slightly different from the stoichiometric one. [107,108] The ratio of Li/P is about 2.9 according to the ICP-AES analysis. The deviation from the stoichiometric value can be attributed to the partial condensation reaction of Li_3PO_4, $2Li_3PO_4 \rightarrow Li_4P_2O_7 + Li_2O$, where the resultant Li_2O is lost during the fabrication.

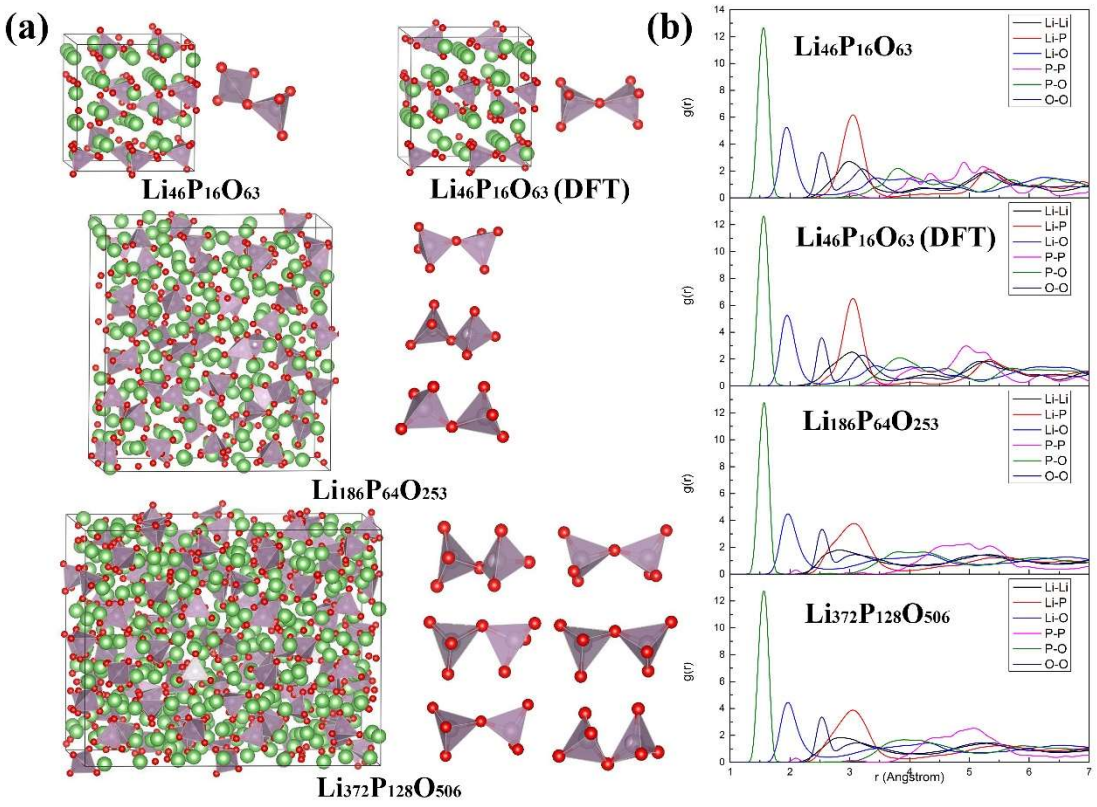

Figure 4.12: The structure of amorphous Li_3PO_4 created by melt quenching simulation. (a) The resultant structures with different size and the shape of $P_2O_7^{4-}$ dimmers inside them. (b) The radial distribution functions of corresponding amorphous structures. Each function is averaged over 5ps MD run at 300K.

The amorphous models having similar Li/P ratio were generated as follows. We started from three crystalline supercells composed of 16, 64 and 128 Li_3PO_4 units. Then, one, three and six Li_2O units were removed from the supercells to set the Li/P ratio as 2.875, 2.906 and 2.906, respectively. The supercells contain 125, 503 and 1006 atoms, respectively. For the three initial structures, the amorphous models were generated by the melt quenching method with the NN-potential-based MD. For comparison, ab-initio MD was also used to perform the same

melt quenching procedures on the smallest model ($Li_{46}P_{16}O_{63}$). The detailed procedure is: 1) initial structures was heated to 2000K and thermalized for 30ps; 2) the structures were subsequently cooled to 300K with a speed of 0.5fs/step; 3) the final structures were equilibrated for 5ps at 300K and then relaxed until the maximum force acting on an atom was smaller than 0.01 eV/Å.

The resultant structures are shown in Figure 4.12(a). We can see a strong similarity between the structures of $Li_{46}P_{16}O_{63}$ created by NN potential and *ab-initio* MD. This demonstrates that the NN potential can reproduce final structures of the melt quenching DFT simulations. On the other hand, it is also noticeable that the generated $Li_{46}P_{16}O_{63}$ structures are partially crystallized. The arrangements of Li and P atoms in the $Li_{46}P_{16}O_{63}$ structures are analogous to those in γ and β-Li_3PO_4, though the orientations of P-O tetrahedrons are disordered. This partial crystallization problem was eliminated by using the larger supercells. As seen in Figure 4.12(a), the resultant structures of large models ($Li_{186}P_{64}O_{253}$ and $Li_{372}P_{128}O_{506}$) are much more disordered. The broader peaks in radial distribution functions shown in Figure 4.12(b) also suggest this. From the first peak positions of the curves shown in Figure 4.12(b), the bond lengths of Li-Li, Li-P, Li-O, P-O and O-O can be estimated as 2.8, 3.1, 2.0, 1.6, and 2.5 Å, respectively. It should be stressed that all the resultant structures include not only the isolated PO_4^{3-} tetrahedrons but also the $P_2O_7^{4-}$ dimers. The $P_2O_7^{4-}$ dimers are formed from two PO_4 tetrahedrons via corner-sharing. The shape of $P_2O_7^{4-}$ dimers found inside the resultant structures are shown in Figure 4.12(a). The presence of this dimer structure is consistent with the observed FTIR spectra of Li_3PO_4 thin film (as introduced in Section 4.1.1).[107]

4.5.2 Diffusivity of Li

The Li diffusion coefficients in the largest amorphous Li_3PO_4 model were evaluated by MD simulations for 100 ps at 600K, 700K, 800K, 1000K and 1200K. The obtained Li diffusion coefficients are plotted in Figure 4.13. The activation energy obtained from the fitting to the Arrhenius law is 0.55 eV.

We also plotted Li diffusion coefficients that measured experimentally by N. Kuwata in Figure 4.13. [108] The Li diffusion coefficient D_{Li} was measured by SIMS for $^6Li/^7Li$ diffusion

couples prepared by an ion-exchange method using liquid electrolyte and a mask method based on thin-film deposition. In addition, the ionic conductivity σ was measured with impedance spectroscopy, and then, conductivity diffusion coefficient D_σ is calculated with Nernst-Einstein equation. The diffusion activation energies obtained from these experiments are 0.58 eV (SIMS, ion-exchange), 0.57 eV (SIMS, mask) and 0.55 eV (impedance spectroscopy).

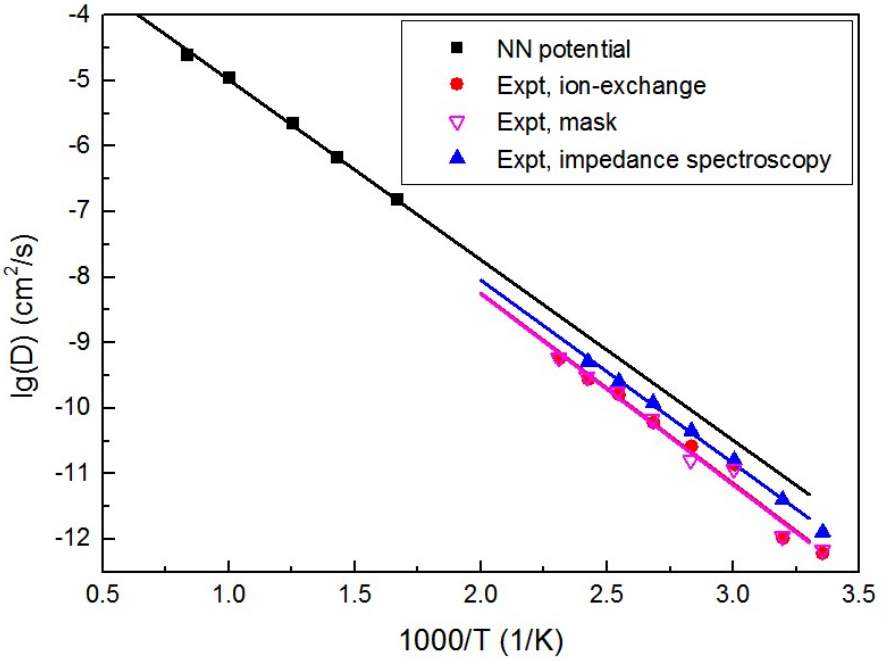

Figure 4.13: The diffusivity of Li in the amorphous Li_3PO_4. The simulation results were obtained from the large-scale MD (1006 atoms) using NN potential. The experimental results were measured with ion mass spectroscopy (SIMS) and impedance spectroscopy (IS)[108].

4.6 Summary

In summary, we investigate the application of high-dimensional NN potential in the study of atomic diffusion using Li_3PO_4 as the model system. For this purpose, an NN potential was constructed using about 38592 various structures and corresponding energies. NNP is capable of accurately predicting the energy of these structures, and the structural and energetic properties of crystalline Li_3PO_4 calculated with NNP are in good agreement with DFT calculation and experiment. In addition, the effective method to reduce the size of input

symmetry function descriptors is discussed. Such method might be useful in applying the NN potential to the system with more chemical elements.

The application of NN potential in atomic diffusion was explored by computing Li vacancy formation energies, diffusion pathways and barrier energies, diffusion coefficients and activation energies in a small disordered Li_3PO_4 model. We found that NN potential can accurately reproduce the DFT results in all kinds of calculation with much small the computational costs. Further, it has been shown that a large-scale amorphous Li_3PO_4 structure can be constructed by the NN potential. The Li diffusivity in it was determined by MD simulation and agrees well with the experimental observation.

Chapter 5

Cu Diffusion in Non-stoichiometric Amorphous AlO_x with Density Variation

5.1 Background

The impact of oxides thin film density on the properties of atomic switch was investigated by T. Tsuruoka[29]. In their work, the Cu/Ta_2O_5/Pt atomic switches were fabricated using the electron beam (EB) deposition and RF sputtering. The Ta_2O_5 thin film deposited with EB deposition has the density of 7.1 g/cm^3, whereas the densities of films fabricated with RF sputtering at 30W and 200W (RF power condition) are 6.2 and 7.6 g/cm^3, respectively. [29] The Ta_2O_5 thin films have a Ta/O atomic ratio of 0.41~0.42, which slightly deviates from the stoichiometric value of 0.4. The cyclic voltammetry measurement of these atomic switches revealed that the density of Ta_2O_5 thin film has great impact of the forming voltage of the atomic switch as seen in Figure 5.1(a). The forming voltage of atomic switch with a dense Ta_2O_5 film (7.6 g/cm^3) is 4.3 V, whereas the one with a low-density film (6.2 g/cm^3) has the formation voltage of 0.44 eV as seen in Figure 5.1(b). They attributed this large reduction of formation voltage to the enhancement of Cu diffusion in the low-density film as schematically shown in Figure 5.1(c).

Actually, the variation of density and composition is widely seen in various amorphous oxides thin films[117][118][119], which has complication influence on the materials properties. For example, C. S. Gorham synthesized several *a*-Al_2O_3 thin films, whose densities were ranging from 2.66 to 3.07 g/cm^3, by varying the temperature during atomic layer deposition (ALD). The thermal conductivities of the thin alumina films at room temperature decreased by 35% with the decrease of atomic density.

In Chapter 4, we have demonstrated that the high-dimensional neural network (NN) potential can accurately reproduce the atomic diffusion behavior in the amorphous materials. In this chapter, our development of the high-dimensional NN potential that is transferable to different density and highly off-stoichiometric composition is described. Such a NN potential has not been developed before as far as we know. In this work, the high-dimensional NN potential was constructed for the amorphous non-stoichiometric Al_2O_3 (a-AlO_x)/Cu system. The density of a-AlO_x (ρ) varies between 2.7 g/cm^3 and 3.3 g/cm^3, while the O/Al ratio, *i.e.* the x value, varies between 1.0 and 1.5. With the Cu/a-AlO_x NN potential, we examine: 1) the effect of density and O/Al ratio variation on the structural characteristics of a-AlO_x; 2) the effect of density and O/Al ratio variation on the Cu diffusion behavior in a-AlO_x. In addition, we expect that these simulations can provide theoretical explanation for the experimental finding of T. Tsuruoka *et al*., that is, the Cu diffusion is enhanced in low-density oxides. For

simplicity, the “high-dimensional neural network potential” will be referred as “neural network potential” or “NN potential” in this chapter.

5.2 Construction of NN potential

5.2.1 Configuration of neural network potential

In constructing the neural network potential for this research, the architecture, input and output of NN potential illustrated in chapter 2 were adopted. To guarantee the quality of NN potential in the large variation ranges of density and composition, it is better to evenly sample the reference structures in the configuration space. However, the density and composition considerably increase the complexity of the configuration space, which makes the selection of training structures not straightforward. Performing the molecular dynamics simulations with DFT, which was adopted in the study described in Chapter 4, is the simplest way to obtain the reference structures. However, the efficiency of this method is low because the snapshots of MD always have high structural correlation. Thus, a more efficient sampling method is urgently needed. Here, a kind of iterative method was adopted to construct the training database for Cu/Al_2O_3 system. The similar procedure is used in the previous study [52] The outline of this method is shown in Figure 5.2. First, an initial training database, which contains only a small number of training structures, is created using a MD trajectory. Then several preliminary NN potentials were trained based on the initial training database. Owing to the small training database, these preliminary potentials can only give a quite rough representation of the potential energy surface. Although these potentials are trained using the same set of training data, the function formula (*i.e.* weights of NN) of these potentials are not exactly the same, because of the high flexibility of NN and different initial values of parameters for training. The two NN potentials with comparable quality are selected. Here, we call them potential I and II, respectively. Then, many structures are generated with potential I, by 1) running the MD simulations at different temperatures (300 ~ 4000 K) and 2) performing NEB calculations for Cu interstitial diffusion. For thus obtained MD trajectories and NEB images, the energies of the structures are recalculated with the potential II. As shown schematically in Figure 5.2, the

energies calculated by potential I and II are compared. If the potentials I and II give very different energies for one structure, it means that the features of the structure is unfamiliar to the NN potential. Such a structure is identified as the problematic structure, which is worth being included into the training database to further refine the quality of potential in this part of configuration space. The refined potentials are again used to identify and select the new problematic structures until no further problematic structures can be found.

To sample the reference structures (Cu/*a*-AlO_x) within the density and composition variation ranges of interest (2.7 g/cm^3 $\leq \rho \leq$ 3.3 g/cm^3; 1.0 $\leq x \leq$ 1.5), the aforementioned self-consistent was used. The initial training database contains the MD trajectories of *a*-Al_2O_3 and *a*-Al_2O_3 +1 Cu whose density and composition as follow: ① ρ=3.2 g/cm^3, x=1.5; ② ρ=3.2 g/cm^3, x=1.0; ③ ρ=1.9 g/cm^3, x=1.5; ④ ρ=2.9 g/cm^3, x=1.0. In the iterative steps, the MD and NEB calculation is performed based on the AlO_x/Cu structures, whose density and atomic ratio is arbitrary combinations of ρ=2.7 g/cm^3, 2.8 g/cm^3, 2.9 g/cm^3, 3.0 g/cm^3, 3.1 g/cm^3, 3.2

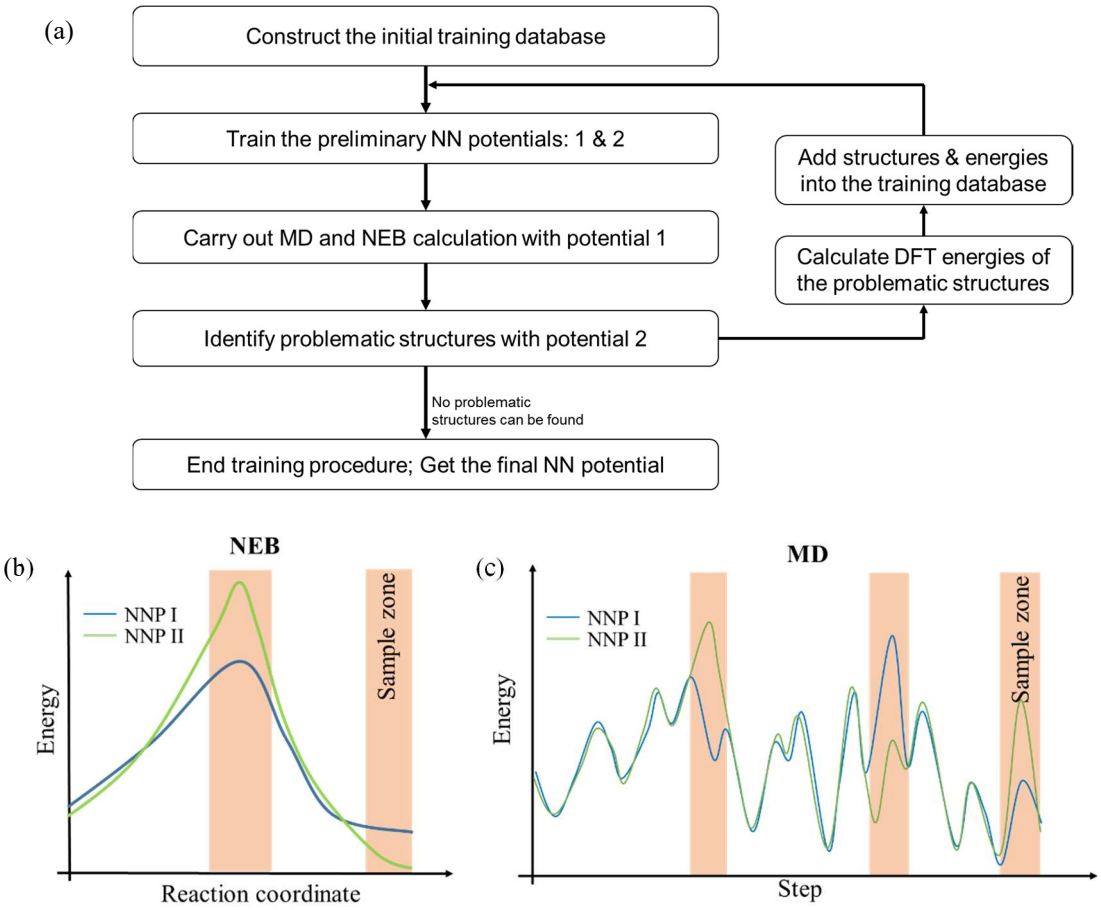

Figure 5.2: (a) Outline of the iterative way of creating training database. (b) and (c) are the illustration of criterion of training data selection using two preliminary fitted NN potentials I and II.

g/cm^3, 3.3 g/cm^3 and x=1.5, 1.375, 1.25, 1.125, and 1. Such method ensures that reference structure evenly distributed in the interested density and atomic ratio range. Finally, we obtained of 41495 structures with a variable size containing up to 161 atoms. These structures are randomly distributed into the training set (90 %) and testing set (10 %).

5.2.3 Training of NN potential

The details of high-dimensional NN potential has been explained in chapter 2 and 4, so I won't reiterate them here. The three layers NN configuration, which is 46-15-15-15-1, was employed for Cu/*a*-AlO*x* potential. Hyperbolic tangent activation functions were used at the nodes of the three hidden layers, and a linear activation function was used at the output node. Such NN architecture results in 3603 parameters in the potential. The G^2-type radial symmetry functions (Equation 2.46) and G^5-type angular symmetry functions (Equation 2.49) re used to

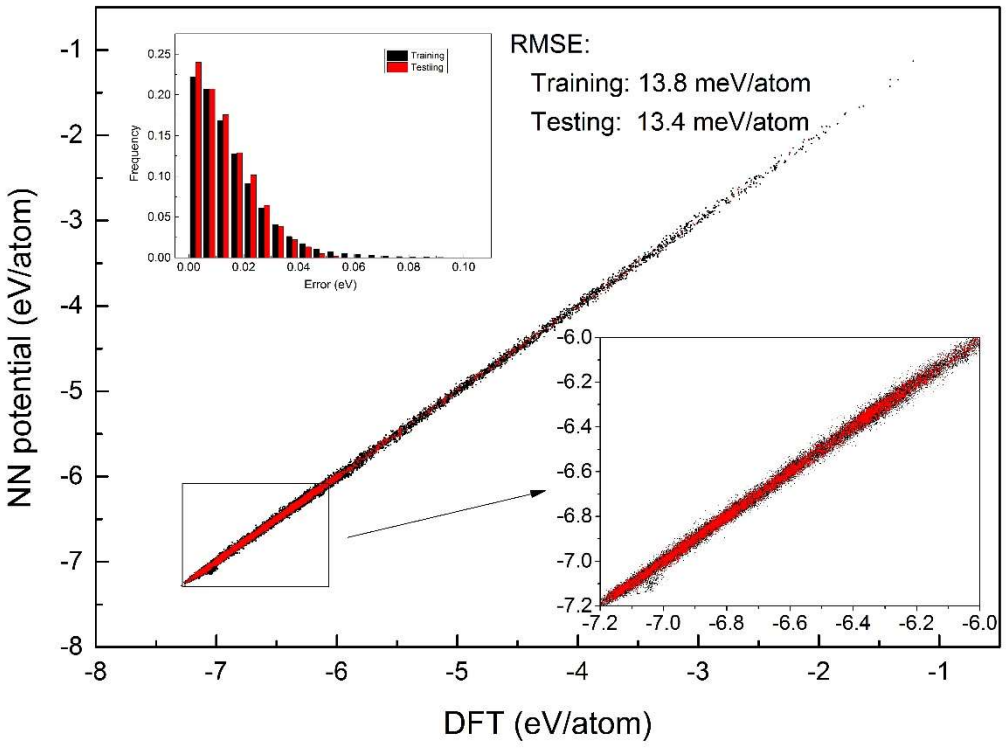

Figure 5.3: A comparison between the total energies of the training set and testing set structures obtained using the DFT and NN approaches. The inset contains the MAE distributions ($|E_{NNP} - E_{DFT}|$) calculated for these two data sets.

describe the local atomic environment of Cu, Al and O atoms. Here, we used the same symmetry functions set with Li_3PO_4, which us presented in the appendix. In Figure 5.3, the NN energies of the training and the testing set are plotted against of their DFT energies. The root mean square error (RMSE) is 13.8 eV/atom for the training set and 13.4 eV/atom for the testing set. The mean absolute error is 6.7 and 6.5 eV/atom for training and testing sets, respectively. The energy prediction error is relatively large compared with the Li_3PO_4 potential in Chapter 4 (RMSE: training 5.0 eV/atom; testing 5.6 eV/atom) and Cu/ZnO NN potential in a previous study [56] (RMSE: training 4.8 eV/atom; testing 5.1 eV/atom), which are both ternary NN potentials. This increase in prediction errot can be attributed to the fact that the density and composition variation considerably increases the structural variety.

5.3 Amorphous AlO_x structures

5.3.1 Structural characteristics of *a*-AlO_x

The melt quenching method base on the constructed NN potential was employed to create the *a*-AlO_x structures with the density and composition variation. The specific steps are as follows. The initial structure was γ-Al_2O_3 supercell containing 256 Al and 384 O atoms. A certain number of O atoms were removed to achieve the desirable atomic ratio. Afterward, the structure was melted at 3500 K for 100 ps under NVT ensemble using a time step of 1fs. During this procedure, the shape of the cell slightly deformed once a few hundred steps, until the density of the as AlO_x supercell is reduced to the desirable value. Then the melted structure was subsequently cooled to 300K with the temperature change speed of 0.5 K/fs. At last, the structure was equilibrated at 300K for 5 ps. This MD trajectory was employed to analyze the structural information (such as bond length, coordination number) of *a*-AlO_x. The final structure was optimized with the NN potential until the maximum force acting on an atom was smaller than 0.02 eV/atom. Figure 5.4 shows representative *a*-AlO_x structures obtained with the procedure described above.

Using the *a*-AlO_x model with ρ = 3.2 g/cm^3 and x = 1.5 (Figure 5.4(c)), we characterized the structural properties of amorphous alumina. The total pair correlation function (PDF) of the *a*-AlO_x model is shown in Figure 5.5(a). The PDF curve is compared with the experimental

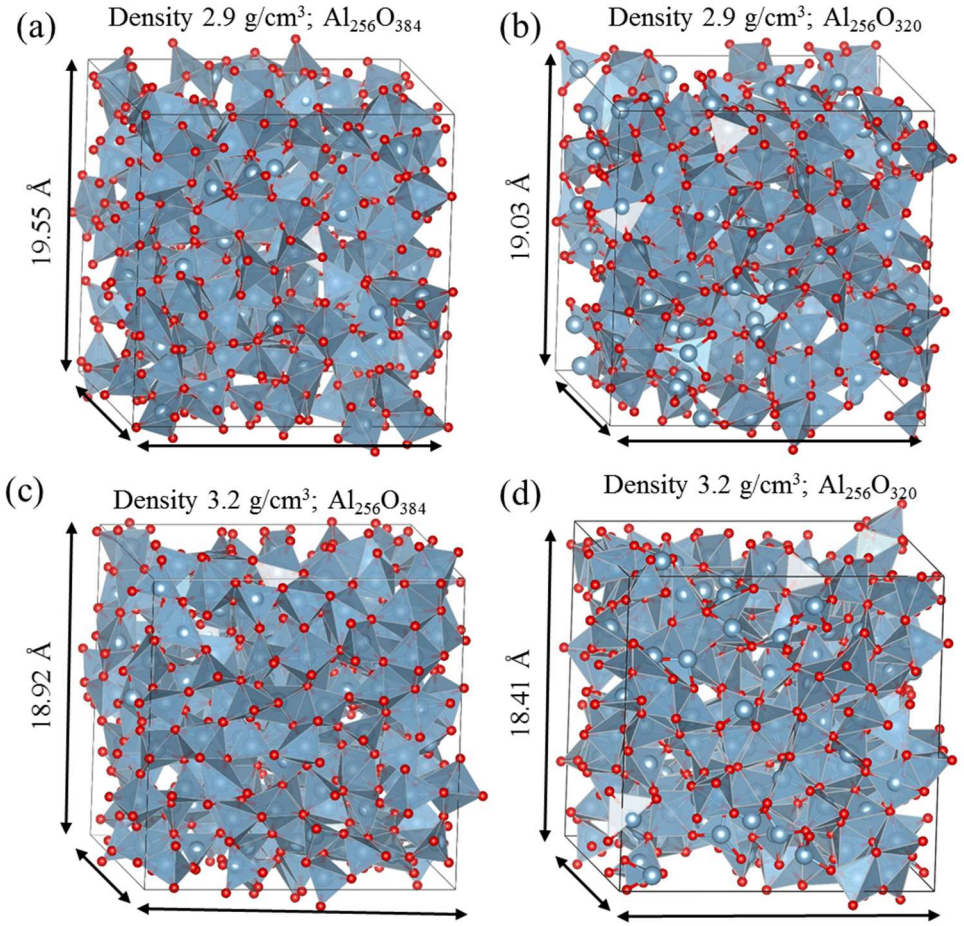

Figure 5.4: The representative *a*-AlO_x structures that created with melt quenching method using NN potential MD.

result obtained from the *x*-ray diffraction measurement by P. Lamparter *et al.*,[120] and two simulation results obtained from the first-principles calculations by D. Sergio[121] and K. Sankaran,[122] respectively. The PDF of our theoretical model shows a good agreement with the experiment measurement and the first-principles calculations. The locations of first and second peaks are 1.81 and 2.82 Å, which coincide with the experimental values of 1.8 and 2.8 Å. The PDF of K. Sankaran's model considerably deviates from other results possibly because the acceleration MD technique (bond-boost method [123]) is used in the simulation.

The partial PDF's of Al-Al, Al-O and O-O pairs are shown in Figure 5.5(b). The location of the first peak of the partial PDF curve represents the corresponding bond length. From it, we estimated the Al-O bond length as 1.81 Å, Al-Al bond length 3.11 Å and O-O bond length 2.79 Å. The bond lengths agree with those estimated from the reverse Monte Carlo model

constructed based on the *x*-ray diffraction, in which the Al-O, Al-Al and O-O bond lengths are 1.8 Å, 3.2 Å and 2.8 Å, respectively. [120]

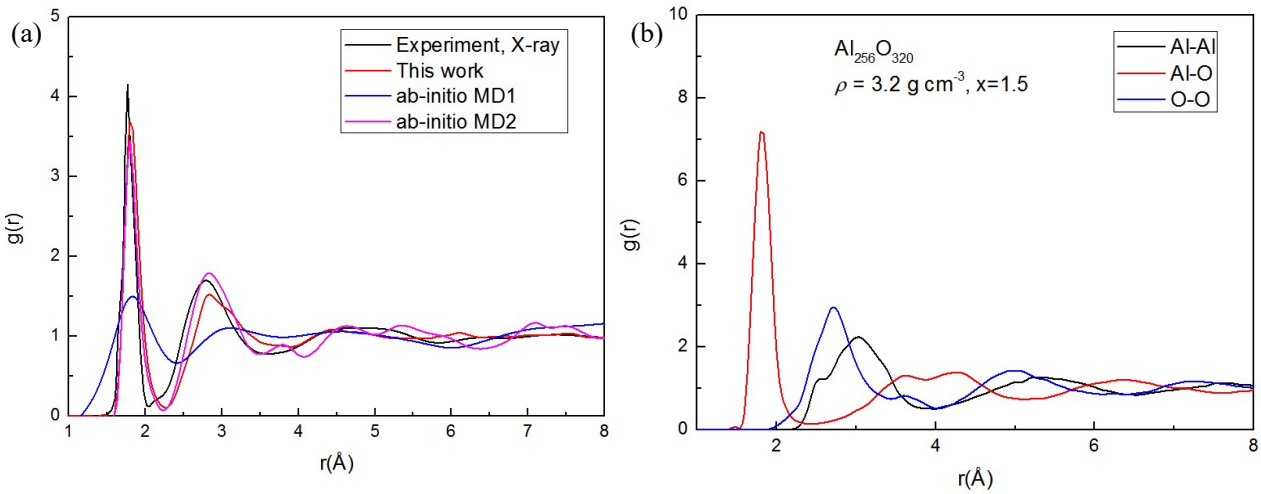

Figure 5.5: (a) The total pair correlation function of amorphous AlO*x* with ρ=3.2 g/cm^3, x=1.5, and the experimental and theoretical results in the previous research. (b) The partial pair correlation function of *a*-AlO$_x$ with ρ=3.2 g/cm^3, x=1.5.

Another very important structural property is the coordination number, which can be computed by the integration around the first peak in the PDF. Note that the Al-O coordination numbers have a great influence on the catalytic ability.[124,125] For example, the five-coordinated Al^{3+} in the Pt/Al_2O_3 heterogeneous catalysts shows much stronger affinity to Pt than other Al^{3+} species and serves as the Pt anchoring site.[125] For this reason, the characterization of Al-O coordination numbers in the amorphous alumina has attracted many research attention. Using nuclear magnetic resonance (NMR) techniques, S. K. Lee's revealed that the fractions for four-, five- and six-coordinated Al were 55%, 42%, and 3% respectively in the amorphous Al_2O_3 thin film fabricated with RF sputtering.[126] Afterward, they further investigated the Al-O coordination numbers in ALD and PLD thin films with the same technique. The fractions of four-, five- and six-coordinated Al in the ALD thin film were 54.3%, 40.6%, and 5.1%, whereas those in the PVD thin films were 56.4%, 36.2%, and 7.4%, respectively.[127] The distribution of Al-O coordination number obtained from the *a*-AlO$_x$ model (ρ=3.2 g/cm^3, x = 1.5) in this work is shown in Figure 5.6, and compared with the experimental results [126,127] and the first-principles calculation results[121]. Three kinds of Al-O polyhedral exist in our amorphous model, which are AlO_4, AlO_5 and AlO_6. Among them,

the four- and five-coordinated Al are the predominant species. The fractions of AlO_4, AlO_5 and AlO_6 were 0.53, 0.45 and 0.02. The average Al-O coordination number was 4.49. We can see the remarkable similarity between our results and previous experimental and theoretical results. All of them show that the AlO_4 and AlO_5 are the main components accounting for more than 90%. The average Al-O coordination numbers are 4.48, 4.508, and 4.51 for the RF sputtering, ALD and PLD thin films and 4.56 for the first-principles calculation.

5.3.2 Effects of density and composition variation

The structural characteristics of our *a*-AlO_x model (ρ=3.2 g/cm^3, x = 1.5) are in good agreement with experimental observations and other theoretical studies. In the next step, the effects of density and composition variation on the structural properties are investigated.

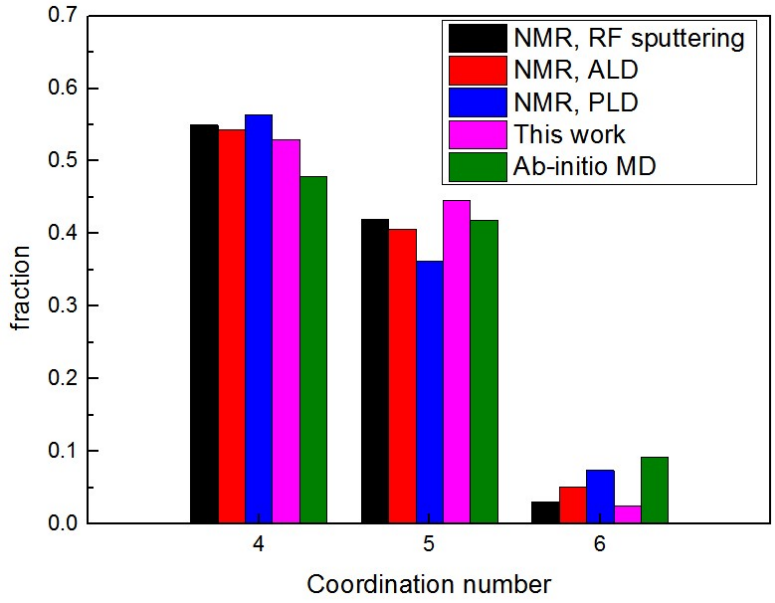

Figure 5.6: The distribution of Al-O coordination numbers. The magenta bars are from the amorphous AlO_x model (ρ=3.2g/cm^3, x = 1.5) in this work. the black, red and blue bars are obtained from the NMR observations of amorphous Al_2O_3 thin films fabricated with RF sputtering[126], ALD[127] and PLD[127], respectively. The Olive bars are from the first-principle structure model of *a*-Al_2O_3[121].

To analyze the influence of density variation, a serial of stoichiometric *a*-$AlO_{1.5}$ models with different densities (ρ = 2.9, 2.95, 3.0, 3.05, 3.1, 3.15, 3.2, 3.25 and 3.3 g/cm^3) were constructed. On the other hand, another set of *a*-AlO_x models, whose densities were fixed to 3.2 g/cm^3 and x values varied from 1 to 1.5, were created to study the effects of composition variation. The

Al-Al, Al-O and O-O bond lengths in these structures were extracted from the partial pair correlation functions, and are plotted in Figure 5.7. With the increase of density, the Al-Al and O-O bond lengths tend to decrease slowly, while the Al-O bond is basically constant. The variation range of Al-Al, O-O, and Al-O bonds are 3.10 ~ 3.21 Å, 2.77 ~ 2.84 Å and 1.81 ~ 1.83 Å. The bond lengths of these structures are shown in Figure 5.7(b). Again, the Al-O bond length is almost constant in the variation range. On the other hand, the Al-Al and O-O lengths increase with x. It is worth mentioning that the Ta-Ta bond length showed similar increase with the proportion of O in the nonstoichiometric a-TaO_x. [128]

The dependence of the average Al-O coordination number and the proportion of different Al-O polyhedra on the density and atomic composition is shown in Figure 5.8. As seen in Figure 5.8(a), a fraction of AlO_5 and AlO_6 increases with the increase of the density, which results in the increase of the average Al-O coordination numbers. The average Al-O

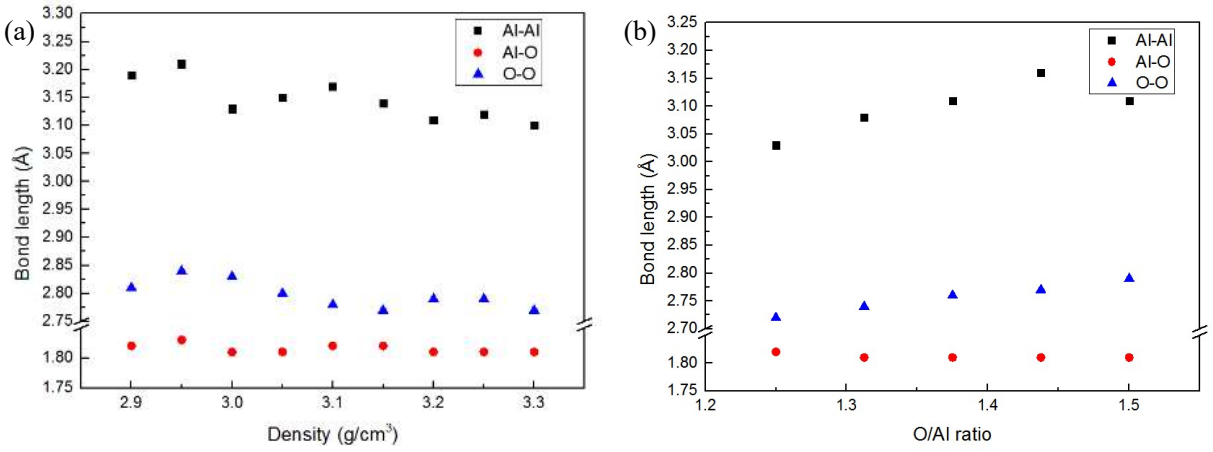

Figure 5.7: (a) The plot of Al–Al, Al-O and O-O bond lengths as a function of density in a-$AlO_{1.5}$ (b) The plot of Al–Al, Al-O and O-O bond lengths as a function of x value in a-AlO_x (density is 3.2 g/cm^3).

coordination number basically follows a linear relationship with the density in the range of 3.0 $\leq \rho \leq$ 3.3 g/cm^3. The similar trend was found by G. Gutierrez also in a-Al_2O_3 with classical MD[43]. The variation range of Al-O coordination number is between 4.3 and 4.7, which also agree with the experimental range of 4.1 to 4.8. The dependence of Al-O coordination number on the atomic composition is shown in Figure 5.8(b). Not surprisingly, the average Al-O coordination number is reduced when the amorphous structure is in O deficiency state (i.e. decrease of x value). In addition, owing to the O deficiency, the two- and three-coordinated Al atoms appear. These species do not exist in the stoichiometric alumina.

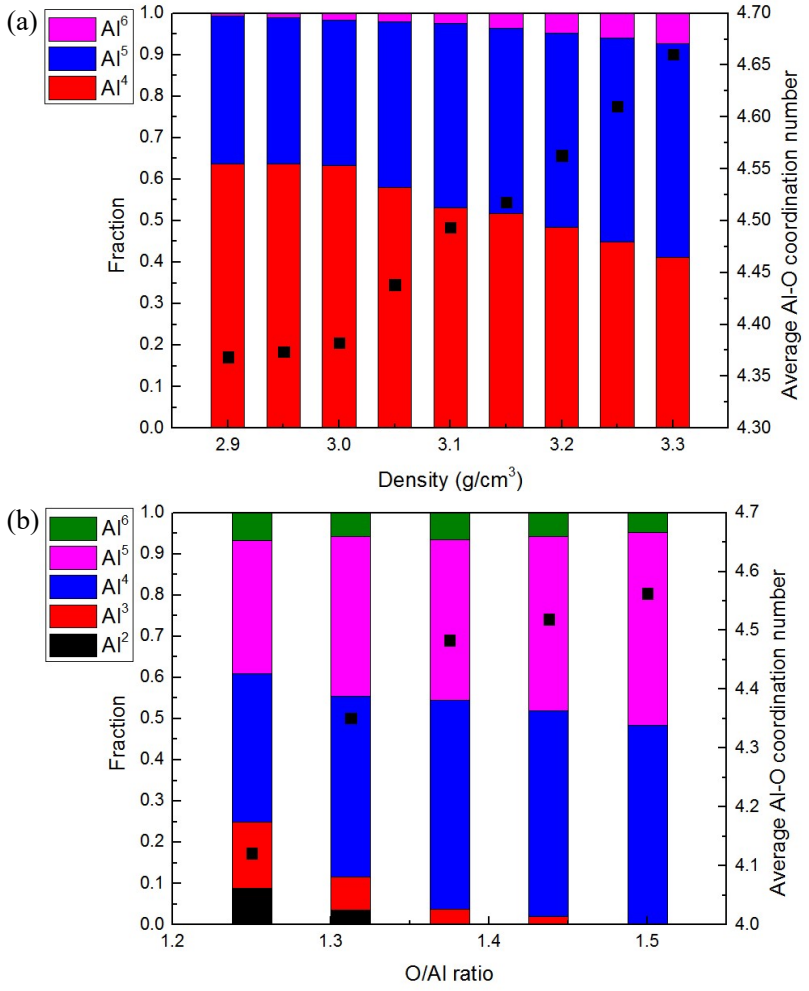

Figure 5.8: The plot of the average Al-O coordination number and the proportion of different Al-O polyhedra in the *a*-AlO_x as a funtion of (a) density (with x = 1.5); (b) x value (with ρ = 3.2 g/cm^3)

5.4 Cu diffusivity in the amorphous Al_2O_3

The Cu diffusivity in the *a*-AlO_x was investigated with the NN-potential MD. In the first step, the Cu diffusion behavior in a stoichiometric amorphous matrix with a density of 3.1 g/cm^3 was studied. The stoichiometric amorphous matrix structure was created with melt quenching method, which has been introduced in the preceding section. The amorphous matrix contains 128 Al atoms and 192 O atoms, and its supercell size is 15.18 Å ×15.18 Å×15.18 Å.

Afterward, one Cu atom was added into the amorphous structures, and MD simulation was performed at 1400K, 1200K, 1000K and 800K. The simulation was performed with the canonical ensemble (NVT) using the Verlet algorithm. The time step is 1fs/step. The total simulation time length is 2ns at 1400 and 1200K and 10 ns at 1000 and 800K. Since the Cu diffusivity is very low at low temperature, we need to perform longer simulations to get reliable values of diffusivity. Figure 5.9 shows the Cu diffusivities of a-Al_2O_3 (ρ=3.1 g/cm^3, x = 1.5). By fitting to the Arrhenius relationship, the activation energy of Cu diffusion was estimated to be 1.02 eV, while the pre-factor D_0 was estimated to be 1.4×10^{-3} cm^2/s. Unfortunately, we could not find any experimental estimation of the Cu diffusivity in amorphous Al_2O_3. However, the theoretical research was performed by K. Sankaran with accelerated ab-initio MD using the bond-boosted technique.[122] Their simulation was also based on the amorphous stoichiometric a-Al_2O_3 with the density of 3.1 g/cm^3. The Cu diffusivities obtained by K. Sankaran are compared with our results in Figure 5.9. We can see that the Cu diffusivities in the temperature range of 800 ~ 1400 K are similar between his and our estimations. The diffusion activation energy extracted from K. Sankaran's simulation is 0.90 eV, which basically agrees with our result.

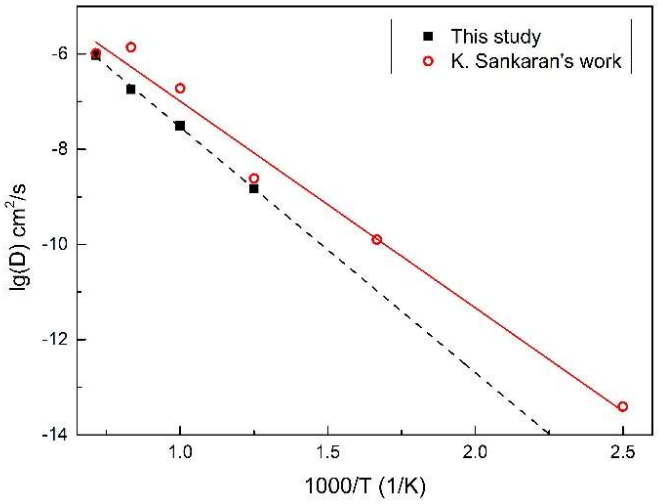

Figure 5.9: The Cu diffusivity in the a-AlO_x (ρ=3.1 g/cm^3, x = 1.5). The black squares represent the results obtained from the NN-potential-based MD, while the red circles represent the simulation results of accelerated ab-initio MD by K. Sankaran[122].

To understand the effect of matrix density on the Cu diffusion behavior, two other amorphous matrices (ρ= 2.9 g/cm^3 and 2.7 g/cm^3) were created, and Cu diffusivities at 800 ~1400K were calculated with the same process. The Cu diffusivities in the three kinds of amorphous matrices are shown in Figure 5.10. The Cu diffusion activation energies and pre-factors obtained from fitting to the Arrhenius relationships are listed in Table 5.1. We can find a rough trend that the Cu diffusion activation energy decreases with decreasing the matrix densities. Although the experimental evidence of this relationship between the density and activation energy cannot be found in the previous literature, the similar trend is reported about the Cu diffusion in amorphous SiO_2. [118] I. Fisher measured the diffusion of Cu into the SiO_2 in metal-insulator-semiconductor devices subjected to thermal stress. The SiO_2 films that were fabricated with self-assembly spin-on deposition, plasma enhanced chemical vapor deposition and thermal growth had very different densities, which were 1.06 g/cm^3, 1.36 g/cm^3 and 2.25 g/cm^3. The Cu diffusion activation energies in these thin films were 0.71 eV, 0.84 eV and 1.02 eV, respectively. By extrapolating the Arrhenius fitting, we estimated the room temperature diffusivities of Cu atoms in the three amorphous matrices to be 4.07×10^{-20} cm^2/s (ρ= 3.1 g/cm^3), 1.17×10^{-18} cm^2/s (ρ= 3.1 g/cm^3) and 1.09×10^{-17} cm^2/s (ρ= 3.1 g/cm^3). With the decreasing of atomic density, the room temperature Cu diffusivity is significantly enhanced. The variation of diffusivities seems to be very large (about three orders of magnitude). Such large diffusivity variation is possible in the amorphous materials. For example, the Li diffusivity in amorphous

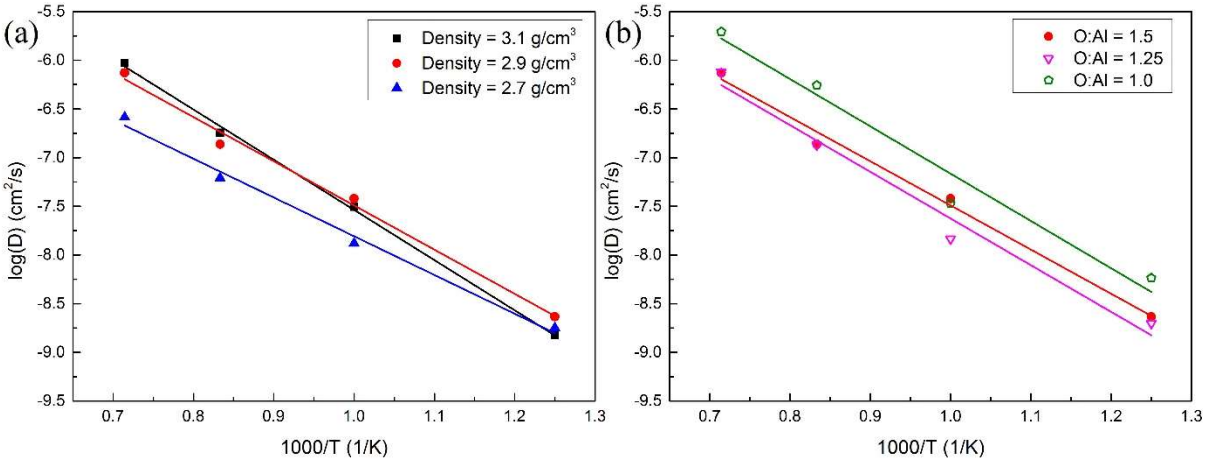

Figure 5.10: The effect of density and composition variation on the Cu diffusion coefficient D in a-AlO_x.

Table 5.1: The Cu diffusion activation energies and pre-factors in the *a*-AlO_x matrix with different densities (ρ=3.1, 2.9 and 2.7 g/cm^3; x=1.5) .

Density	Activation Energy	Pre-factor
3.1 g/cm^3	1.02 eV	4.10×10^{-3} cm^2/s
2.9 g/cm^3	0.90 eV	1.12×10^{-3} cm^2/s
2.7 g/cm^3	0.79 eV	1.49×10^{-4} cm^2/s

silicon spans four orders of magnitude, from 10^{-14} cm^2/s to 10^{-10} cm^2/s.[129–131] The relationship between the density and diffusivity is also consistent with the hypothesis of T. Tsuruoka based on the effect of thin film density on the formation voltage of Cu/Ta_2O_5/Pt atomic switch. In their hypothesis, Cu atoms can migrate faster in the low-density Ta_2O_5 thin film, which results in the significant decrease of formation voltage from 4.3 to 0.44 V.[29] It should be mentioned that their group also reported the great influence of the water molecules absorbed in the *a*-Ta_2O_5 thin film on the Cu diffusion,[28,29] this water molecular effect was not considered in this research. Thus further research is still needed to give a thorough insight of atomic diffusion behavior in the atomic switch. Anyway, we believe the NN potential (maybe Cu/Al/O/H quaternary potential) can be a powerful tool for solving this problem considering the fact that it has been successfully applied to the solid-water interface system.[59]

At last, the effect of O/Al atomic ratio on the Cu diffusion behavior was investigated using three models with (ρ= 2.9 g/cm^3; x = 1.5), (ρ= 2.9 g/cm^3; x = 1.25) and (ρ= 2.9 g/cm^3; x = 1.0). The Cu diffusivities in these models were calculated in the same way as the above and are plotted in the Figure 5.10(b). The Cu activation energies and pre-factors are listed in Table 5.2. Unlike the density variation, the change of atomic ratio in *a*-AlO_x matrix does not significantly influence the Cu diffusion activation energy. However, the Cu diffusion in enhanced in the severe O deficient case (x = 1.0).

Table 5.2: The Cu diffusion activation energies and pre-factors in the *a*-AlO_x matrix with different O/Al ratios (x = 1.5, 1.25 and 1.0; ρ = 2.9 g/cm^3) .

O/Al ratio	Activation Energy	Pre-factor
1.50	0.90 eV	1.12×10^{-3} cm^2/s
1.25	0.95 eV	1.48×10^{-3} cm^2/s
1.00	0.96 eV	4.96×10^{-3} cm^2/s

5.5 Summary

The high-dimensional neural network potential for the Cu/*a*-AlO_x system was constructed. The NN potential that can consider the large density and composition variation ($2.7 \leq \rho \leq 3.3$ g/cm^3; $1.0 \leq x \leq 1.5$) was constructed for the first time. Based on the NN potential, we investigated 1) the effect of density and composition variation on the structure of *a*-AlO_x; 2) the effect of density and composition variation on the Cu diffusion behavior in the *a*-AlO_x.

The structural properties of *a*-AlO_x, such as the pair correlation function, bond length and coordination number, are consistent with the experimental observations and other theoretical models. With the increase of density, the Al-Al and O-O bond lengths decreased and Al-O coordination number increased. On the other hand, the Al-Al and O-O bond lengths as well as the Al-O coordination number increased with the O/Al ratio (*i.e. x* value).

The Cu diffusivity in the *a*-AlO_x (ρ=3.1 g/cm^3, x = 1.5) was consistent with the previous theoretical research with accelerated ab-initio MD. With the decrease of *a*-AlO_x density from 3.1 to 2.7 g/cm^3, the activation energies decreased from 1.02 eV to 0.79 eV. By extrapolating the diffusivities using the Arrhenius relationship, we found that the room temperature diffusivities of Cu are enhanced with the decrease of *a*-AlO_x density. This is consistent with the

hypothesis proposed by T. Tsuruoka to explain the effect of thin film density on the formation voltage of Cu/Ta_2O_5/Pt atomic switch. On the other hand, the variation of O/Al ratio does not have a significant impact on the Cu diffusion activation energy.

Although the relationship between matrix density and atom diffusivity found in this work is consistent with T. Tsuruoka's experiments, further study, e.g. consideration including the moisture effect, is needed to provide a thorough understanding of atomic diffusion in the atomic switch. We expect that such research tasks can be done with the NN potential in the future.

Chapter 6

Summary and Outlook

Atom/ion diffusion in amorphous materials is an important phenomenon in many nanoscale information and energy devices. However, the systematical theoretical investigation of this issue is hindered by the high computational cost and slow simulation speed of first-principles calculation. In this dissertation, we tried to apply the neural network (NN) potential to tackle this issue. We proposed the simplified NN potential method and explored the applicability of high-dimensional NN potential in simulating atomic diffusion in amorphous materials. The material systems that we investigated are 1) the amorphous oxides (*a*-Ta_2O_5 and *a*-AlO_x) with single Cu atoms for the atomic switch and 2) the amorphous Li_3PO_4 (*a*-Li_3PO_4) for all-solid-state Li ion battery and a novel memory device.

1. Potential for Cu diffusion in amorphous Ta_2O_5

We proposed the simplified NN potential, which considers only the diffusing atoms explicitly and can be used to predict interstitial diffusion paths and barrier energies. The main results are summarized as follow:

1) The root mean square error (RMSE) for energy predictions with the constructed NN potential compared with the DFT calculations was 23 meV/structure for the training set and 39 meV/structure for the independent testing set. The computation speed of the NN potential was approximately 10^7 times faster than DFT.
2) The accuracy of simplified NN potential in predicting diffusion paths and barrier energies was demonstrated by comparing the NEB results on an example diffusion path with those of DFT calculation. The largest discrepancy in energy along the path was about 0.15 eV.
3) From the Cu diffusion coefficients calculated with the NN potential and the kinetic Monte Carlo method, we estimated the Cu diffusion activation energy in the temperature range of

500−800 K as 0.67 eV, which agrees well with the estimate based on experimental data, 0.64 eV.

2. Potential for Li diffusion amorphous Li_3PO_4

We constructed the high-dimensional NN potential for amorphous Li_3PO_4 (*a*-Li_3PO_4), and used it to study the Li atom diffusion. Our findings from the results are:

1) The accuracy of NN potential in energy prediction was 5.0 meV/atom in training set and 5.6 meV/atom in the testing set. The structural and energetic properties of crystalline Li_3PO_4 calculated with it are in good agreement with DFT calculation and experiment.
2) Various properties related to Li diffusion properties (*e.g.* Li vacancy formation energies, diffusion pathways and barrier energies, diffusion coefficients and activation energies) were calculated with the NN potential in a small *a*-Li_3PO_4 model. For all of these results, we found good accordance with the corresponding DFT calculation.
3) The large-scale *a*-Li_3PO_4 structure containing 1006 atoms was constructed with the NN potential. The formation of P_2O_7 units in the *a*-Li_3PO_4 was observed, which is consistent with the experimental characterization. The Li diffusion activation energy in it was estimated to be 0.55 eV, which also agrees with the experimental measurements (0.55 ~ 0.58 eV).

3. Potential for Cu diffusion in amorphous non-stoichiometric alumina with density variation

We developed the high-dimensional NN potential for Cu/*a*-AlO_x system with the wide range of variation in density (2.7 ~3.3 g/cm^3) and atomic composition (O/Al ratio of 1.0 ~ 1.5) and utilized it to study the effect of density and composition variation on the Cu diffusion behavior. The important conclusions are:

1) The accuracy of the NN potential in energy prediction was about 14 meV/atom in the whole range of density and composition variation.
2) The *a*-AlO_x structures constructed with the melt-quenching method using the NN potential had the structural properties (pair correlation function, bond length and coordination number) consistent with the experimental observations and other theoretical models.
3) From the MD simulation, we found that the Cu diffusion activation energies decreased from 1.02 eV to 0.79 eV with the decrease of *a*-AlO_x density from 3.1 to 2.7 g/cm^3, while

the room temperature diffusivities of Cu were increased from 4.07×10^{-20} cm^2/s to 1.09×10^{-17} cm^2/s. On the other hand, the variation of O/Al ratio did not have a significant impact on the Cu diffusion activation energy.

4) The above increase in Cu diffusivity in the low-density oxides can provide the theoretical explanation for the experimental finding on $Cu/Ta_2O_5/Pt$ atomic switch, that is, the formation voltage of atomic switch drops with the decrease in the density of oxides thin film.

In this dissertation, we proposed several NN potentials to study atomic diffusion in amorphous materials. There are several issues remained for the future study. In the aspect of methodology, the simplified NN potential method we proposed should be further improved to achieve a better transferability. In addition, it is also an important and challenging task to break through the inherent limitation of high-dimensional NN potential in the cases including many atomic species, and apply the NN potential to more complicated systems. Last but not least, the development of NN potential under external electric fields is also a very interesting topic. In the aspect of application, the NN potentials that we constructed can be used to further investigate the important issues related to novel information and energy devices such as atomic switch and batteries: For example, the Cu diffusion in oxides with the presence of water molecules, the mechanism of Li diffusion in amorphous Li_3PO_4 or LiPON, *etc.*

Appendix

Parameters of symmetry functions

A. For the Cu/Ta_2O_5 simplified NN potential

(1) Parameters for G^2-type symmetry functions

No.	Neighboring atom	η (Å^{-2})	R_c (Å)	No.	Neighboring atom	η (Å^{-2})	R_c (Å)
1	O	0.001	8	9	Ta	0.001	8
2	O	0.03	8	10	Ta	0.03	8
3	O	0.07	8	11	Ta	0.07	8
4	O	0.12	8	12	Ta	0.12	8
5	O	0.20	8	13	Ta	0.20	8
6	O	0.30	8	14	Ta	0.30	8
7	O	0.50	8	15	Ta	0.50	8
8	O	1.00	8	16	Ta	1.00	8

(2) Parameters for G^5-type symmetry functions

No.	Neighboring atom	η (Å^{-2})	ζ	λ	R_c (Å)	No.	Neighboring atom	η (Å^{-2})	ζ	λ	R_c (Å)
1	O	0.004	1	-1	8	11	Ta	0.004	1	-1	8
2	O	0.004	2	1	8	12	Ta	0.004	2	1	8
3	O	0.01	1	-1	8	13	Ta	0.01	1	-1	8
4	O	0.01	2	1	8	14	Ta	0.01	2	1	8
5	O	0.05	1	1	8	15	Ta	0.05	1	1	8
6	O	0.05	16	1	8	16	Ta	0.05	16	1	8
7	O	0.09	1	1	8	17	Ta	0.09	1	1	8
8	O	0.09	16	1	8	18	Ta	0.09	16	1	8
9	O	0.16	1	1	8	19	Ta	0.16	1	1	8
10	O	0.16	16	1	8	20	Ta	0.16	16	1	8

B. For Li_3PO_4 and Cu/AlO_x high-dimensional NN potential

For the different combinations of center species and neighboring species, the same radial and angular symmetry functions are used. Therefore, the species of center atom and neighboring atoms will not indicated in the table.

(1) Parameters for G^2-type symmetry functions

No.	η	R_c
1	0.001	8
2	0.03	8
3	0.07	8
4	0.12	8
5	0.2	8
6	0.3	8
7	0.5	8
8	1	8

(2) Parameters for G^5-type symmetry functions

No.	ζ	λ	η	R_c
1	1	-1	0.0004	8
2	1	1	0.0004	8
3	2	-1	0.0004	8
4	2	1	0.0004	8
5	1	-1	0.01	8
6	1	1	0.01	8
7	2	-1	0.01	8
8	2	1	0.01	8
9	1	1	0.03	8
10	2	1	0.03	8
11	1	1	0.05	8
12	2	1	0.05	8
13	4	1	0.05	8
14	16	1	0.05	8
15	1	1	0.09	8
16	2	1	0.09	8
17	4	1	0.09	8
18	16	1	0.09	8
19	1	1	0.16	8
20	2	1	0.16	8
21	4	1	0.16	8
22	16	1	0.16	8

Bibliography

[1] S. Clima, K. Sankaran, Y.Y. Chen, A. Fantini, U. Celano, A. Belmonte, L. Zhang, L. Goux, B. Govoreanu, R. Degraeve, D.J. Wouters, M. Jurczak, W. Vandervorst, S. De Gendt, and G. Pourtois, Phys. Status Solidi - Rapid Res. Lett. **8**, 501 (2014).

[2] T. Hasegawa, K. Terabe, T. Tsuruoka, and M. Aono, Adv. Mater. **24**, 252 (2012).

[3] D.M. Eigler, C.P. Lutz, and W.E. Rudge, Nature **352**, 600 (1991).

[4] K. Terabe, T. Nakayama, T. Hasegawa, and M. Aono, Appl. Phys. Lett. **80**, 4009 (2002).

[5] K. Terabe, T. Nakayama, T. Hasegawa, and M. Aono, J. Appl. Phys. **91**, 10110 (2002).

[6] T. Hasegawa, K. Terabe, T. Nakayama, and M. Aono, RIKEN Rev. **37**, 7 (2001).

[7] K. Terabe, T. Hasegawa, T. Nakayama, and M. Aono, Nature **433**, 47 (2005).

[8] T. Tamura, T. Hasegawa, K. Terabe, T. Nakayama, T. Sakamoto, H. Sunamura, H. Kawaura, S. Hosaka, and M. Aono, Jpn. J. Appl. Phys. **45**, L364 (2006).

[9] T. Tamura, T. Hasegawa, K. Terabe, T. Nakayama, T. Sakamoto, H. Sunamura, H. Kawaura, S. Hosaka, and M. Aono, J. Phys. Conf. Ser. **61**, 1157 (2007).

[10] I. Valov, I. Sapezanskaia, A. Nayak, T. Tsuruoka, T. Bredow, T. Hasegawa, G. Staikov, M. Aono, and R. Waser, Nat. Mater. **11**, 530 (2012).

[11] A. Nayak, T. Tsuruoka, K. Terabe, T. Hasegawa, and M. Aono, Appl. Phys. Lett. **98**, 233501 (2011).

[12] Q. Xia, J.J. Yang, W. Wu, X. Li, and R.S. Williams, Nano Lett. **10**, 2909 (2010).

[13] R. Waser, R. Dittmann, G. Staikov, and K. Szot, Adv. Mater. **21**, 2632 (2009).

[14] C. Liang, K. Terabe, T. Hasegawa, R. Negishi, T. Tamura, and M. Aono, Small **1**, 971 (2005).

[15] M. Morales-Masis, S.J. van der Molen, W.T. Fu, M.B. Hesselberth, and J.M. van Ruitenbeek, Nanotechnology **20**, 95710 (2009).

[16] M. Kundu, K. Terabe, T. Hasegawa, and M. Aono, J. Appl. Phys. **99**, 103501 (2006).

[17] T. Sakamoto, H. Sunamura, H. Kawaura, T. Hasegawa, T. Nakayama, and M. Aono, Appl. Phys. Lett. **82**, 3032 (2003).

[18] M. Kundu, T. Hasegawa, K. Terabe, and M. Aono, J. Appl. Phys. **103**, 73523 (2008).

[19] R. Soni, P. Meuffels, A. Petraru, M. Weides, C. Kügeler, R. Waser, and H. Kohlstedt, J. Appl. Phys. **107**, 24517 (2010).

[20] T. Sakamoto, K. Lister, N. Banno, T. Hasegawa, K. Terabe, and M. Aono, Appl. Phys. Lett. **91**, 92110 (2007).

[21] M. Haemori, T. Nagata, and T. Chikyow, Appl. Phys. Express **2**, 61401 (2009).

[22] C. Schindler, M. Weides, M.N. Kozicki, and R. Waser, Appl. Phys. Lett. **92**, 122910 (2008).

[23] K. Tsunoda, Y. Fukuzumi, J.R. Jameson, Z. Wang, P.B. Griffin, and Y. Nishi, Appl. Phys. Lett. **90**, 113501 (2007).
[24] Y.C. Yang, F. Pan, Q. Liu, M. Liu, and F. Zeng, Nano Lett. **9**, 1636 (2009).
[25] I. Valov, R. Waser, J.R. Jameson, and M.N. Kozicki, Nanotechnology **22**, 254003 (2011).
[26] N. Banno, T. Sakamoto, N. Iguchi, H. Sunamura, K. Terabe, T. Hasegawa, and M. Aono, IEEE Trans. Electron Devices **55**, 3283 (2008).
[27] S. Kaeriyama, T. Sakamoto, H. Sunamura, M. Mizuno, H. Kawaura, T. Hasegawa, K. Terabe, T. Nakayama, and M. Aono, IEEE J. Solid-State Circuits **40**, 168 (2005).
[28] T. Tsuruoka, K. Terabe, T. Hasegawa, I. Valov, R. Waser, and M. Aono, Adv. Funct. Mater. **22**, 70 (2012).
[29] T. Tsuruoka, I. Valov, S. Tappertzhofen, J. van den Hurk, T. Hasegawa, R. Waser, and M. Aono, Adv. Funct. Mater. **25**, 6374 (2015).
[30] S. Watanabe and B. Xiao, 2014 IEEE Int. Nanoelectron. Conf. 113 (2014).
[31] B. Xiao and S. Watanabe, ACS Appl. Mater. Interfaces **7**, 519 (2015).
[32] T. Gu, Z. Wang, T. Tada, and S. Watanabe, J. Appl. Phys. **106**, 103713 (2009).
[33] T. Gu, T. Tada, and S. Watanabe, ACS Nano **4**, 6477 (2010).
[34] B. Xiao, T. Gu, T. Tada, and S. Watanabe, J. Appl. Phys. **115**, 34503 (2014).
[35] J.F.M. Oudenhoven, L. Baggetto, and P.H.L. Notten, Adv. Energy Mater. **1**, 10 (2011).
[36] J.B. Bates, Solid State Ionics **56**, 53 (1992).
[37] X. Yu, J.B. Bates, G.E. Jellison, and F.X. Hart, J. Electrochem. Soc. **144**, 524 (1997).
[38] C.H. Choi, W.I. Cho, B.W. Cho, H.S. Kim, Y.S. Yoon, and Y.S. Tak, Electrochem. Solid-State Lett. **5**, A14 (2002).
[39] S. Zhao, Z. Fu, and Q. Qin, Thin Solid Films **415**, 108 (2002).
[40] F. Vereda, R.B. Goldner, T.E. Haas, and P. Zerigian, Electrochem. Solid-State Lett. **5**, A239 (2002).
[41] F. Vereda, N. Clay, A. Gerouki, R.. Goldner, T. Haas, and P. Zerigian, J. Power Sources **89**, 201 (2000).
[42] D.M. Guzman, N. Onofrio, and A. Strachan, J. Appl. Phys. **117**, 195702 (2015).
[43] G. Gutiérrez and B. Johansson, Phys. Rev. B **65**, 104202 (2002).
[44] H. Momida, T. Hamada, Y. Takagi, T. Yamamoto, T. Uda, and T. Ohno, Phys. Rev. B **73**, 54108 (2006).
[45] R. Bassiri, K.B. Borisenko, D.J.H. Cockayne, J. Hough, I. MacLaren, and S. Rowan, Appl. Phys. Lett. **98**, 31904 (2011).
[46] G.A. Tritsaris, K. Zhao, O.U. Okeke, and E. Kaxiras, J. Phys. Chem. C **116**, 22212 (2012).
[47] P. Johari, Y. Qi, and V.B. Shenoy, Nano Lett. **11**, 5494 (2011).
[48] S. Hao and C. Wolverton, J. Phys. Chem. C **117**, 8009 (2013).
[49] J. Behler and M. Parrinello, Phys. Rev. Lett. **98**, 146401 (2007).
[50] R.Z. Khaliullin, H. Eshet, T.D. Kühne, J. Behler, and M. Parrinello, Nat. Mater. **10**, 693 (2011).
[51] R.Z. Khaliullin, H. Eshet, T.D. Kühne, J. Behler, and M. Parrinello, Phys. Rev. B **81**,

100103 (2010).
[52] N. Artrith and J. Behler, Phys. Rev. B **85**, 45439 (2012).
[53] N. Artrith, T. Morawietz, and J. Behler, Phys. Rev. B **83**, 153101 (2011).
[54] N. Artrith and A. Urban, Comput. Mater. Sci. **114**, 135 (2016).
[55] T. Morawietz and J. Behler, J. Phys. Chem. A **117**, 7356 (2013).
[56] N. Artrith, B. Hiller, and J. Behler, Phys. Status Solidi **250**, 1191 (2013).
[57] N. Artrith and A.M. Kolpak, Nano Lett. **14**, 2670 (2014).
[58] G.C. Sosso, G. Miceli, S. Caravati, F. Giberti, J. Behler, and M. Bernasconi, J. Phys. Chem. Lett. **4**, 4241 (2013).
[59] S. Kondati Natarajan and J. Behler, J. Phys. Chem. C **121**, 4368 (2017).
[60] G. Kresse and J. Furthmüller, Comput. Mater. Sci. **6**, 15 (1996).
[61] G. Kresse and J. Furthmüller, Phys. Rev. B **54**, 11169 (1996).
[62] L. Verlet, Phys. Rev. **159**, 98 (1967).
[63] R. Car and M. Parrinello, Phys. Rev. Lett. **55**, 2471 (1985).
[64] G. Henkelman, B.P. Uberuaga, and H. Jónsson, J. Chem. Phys. **113**, 9901 (2000).
[65] D. Sheppard, R. Terrell, and G. Henkelman, J. Chem. Phys. **128**, 134106 (2008).
[66] H. Jónsson, G. Mills, and K.W. Jacobsen, Class. Quantum Dyn. Condens. Phase Simulations 385 (1998).
[67] A. Voter, Radiat. Eff. Solids **235**, 1 (2007).
[68] A.F. Voter and J.D. Doll, J. Chem. Phys. **80**, 5832 (1984).
[69] P. Hohenberg and W. Kohn, Phys. Rev. **136**, B864 (1964).
[70] W. Kohn and L.J. Sham, Phys. Rev. **140**, A1133 (1965).
[71] D.C. Langreth and M.J. Mehl, Phys. Rev. Lett. **47**, 446 (1981).
[72] J.P. Perdew and Y. Wang, Phys. Rev. B **45**, 13244 (1992).
[73] J.P. Perdew, K. Burke, and M. Ernzerhof, Phys. Rev. Lett. **77**, 3865 (1996).
[74] J.D. Pack and H.J. Monkhorst, Phys. Rev. B **16**, 1748 (1977).
[75] R.P. Feynman, Phys. Rev. **56**, 340 (1939).
[76] P. Pulay, Mol. Phys. **17**, 197 (1969).
[77] P. Bendt and A. Zunger, Phys. Rev. Lett. **50**, 1684 (1983).
[78] J. Behler, J. Chem. Phys. **145**, 170901 (2016).
[79] C.M. Handley and J. Behler, Eur. Phys. J. B **87**, 152 (2014).
[80] T. Suzuki, R. Tamura, and T. Miyazaki, Int. J. Quantum Chem. **117**, 33 (2017).
[81] S. Kondati Natarajan, T. Morawietz, and J. Behler, Phys. Chem. Chem. Phys. **17**, 8356 (2015).
[82] J. Behler, J. Phys. Condens. Matter **26**, 183001 (2014).
[83] J. Behler, Int. J. Quantum Chem. **115**, 1032 (2015).
[84] J. Behler, Phys. Chem. Chem. Phys. **13**, 17930 (2011).
[85] A.P. Bartók and G. Csányi, Int. J. Quantum Chem. **115**, 1051 (2015).
[86] A.P. Bartók, M.C. Payne, R. Kondor, and G. Csányi, Phys. Rev. Lett. **104**, 136403 (2010).
[87] A. Seko, A. Takahashi, and I. Tanaka, Phys. Rev. B **90**, 24101 (2014).
[88] A. Seko, A. Takahashi, and I. Tanaka, Phys. Rev. B **92**, 54113 (2015).

[89] J. Behler, S. Lorenz, and K. Reuter, J. Chem. Phys. **127**, 14705 (2007).
[90] C.G. Broyden, IMA J. Appl. Math. **6**, 76 (1970).
[91] G.C. Sosso, G. Miceli, S. Caravati, J. Behler, and M. Bernasconi, Phys. Rev. B **85**, 174103 (2012).
[92] J. Behler, J. Chem. Phys. **134**, 74106 (2011).
[93] J.B. Witkoskie and D.J. Doren, J. Chem. Theory Comput. **1**, 14 (2005).
[94] S. Zaima, T. Furuta, Y. Koide, Y. Yasuda, and M. Iida, J. Electrochem. Soc. **137**, 2876 (1990).
[95] L.A. Aleshina and S. V. Loginova, Crystallogr. Reports **47**, 415 (2002).
[96] A. Fukumoto and K. Miwa, Phys. Rev. B **55**, 11155 (1997).
[97] Y.N. Wu, L. Li, and H.P. Cheng, Phys. Rev. B **83**, 144105 (2011).
[98] W. Andreoni and C.A. Pignedoli, Appl. Phys. Lett. **96**, 62901 (2010).
[99] B.R. Sahu and L. Kleinman, Phys. Rev. B **69**, 165202 (2004).
[100] R. Bassiri, K.B. Borisenko, D.J.H. Cockayne, J. Hough, I. MacLaren, and S. Rowan, Appl. Phys. Lett. **98**, 31904 (2011).
[101] G. Kresse and D. Joubert, Phys. Rev. B **59**, 1758 (1999).
[102] Y. Wang and J.P. Perdew, Phys. Rev. B **44**, 13298 (1991).
[103] P. Langfelder, B. Zhang, and S. Horvath, Bioinformatics **24**, 719 (2008).
[104] S. Hao and C. Wolverton, J. Phys. Chem. C **117**, 8009 (2013).
[105] N.J. Dudney, Mater. Sci. Eng. B **116**, 245 (2005).
[106] I. Sugiyama, R. Shimizu, T. Suzuki, K. Yamamoto, H. Kawasoko, S. Shiraki, and T. Hitosugi, APL Mater. **5**, 46105 (2017).
[107] N. Kuwata, N. Iwagami, Y. Tanji, Y. Matsuda, and J. Kawamura, J. Electrochem. Soc. **157**, A521 (2010).
[108] N. Kuwata, X. Lu, T. Miyazaki, Y. Iwai, T. Tanabe, and J. Kawamura, Solid State Ionics **294**, 59 (2016).
[109] G. Kresse and J. Furthmüller, Phys. Rev. B **54**, 11169 (1996).
[110] M. Fuchs and M. Scheffler, Comput. Phys. Commun. **119**, 67 (1999).
[111] J.P. Perdew, K. Burke, and M. Ernzerhof, Phys. Rev. Lett. **77**, 3865 (1996).
[112] G. Pranami and M.H. Lamm, J. Chem. Theory Comput. **11**, 4586 (2015).
[113] S. Sicolo and K. Albe, J. Power Sources **331**, 382 (2016).
[114] Y.A. Du and N.A.W. Holzwarth, Phys. Rev. B **76**, 174302 (2007).
[115] Y.A. Du and N.A.W. Holzwarth, J. Electrochem. Soc. **154**, A999 (2007).
[116] Y.A. Du and N.A.W. Holzwarth, Phys. Rev. B **81**, 184106 (2010).
[117] K. Arbi, S. Mandal, A. J. M. Rojo, and J. Sanz, Chem. Mater. **14**, 1091 (2002).
[118] I. Fisher and M. Eizenberg, Thin Solid Films **516**, 4111 (2008).
[119] C.S. Gorham, J.T. Gaskins, G.N. Parsons, M.D. Losego, and P.E. Hopkins, Appl. Phys. Lett. **104**, 253107 (2014).
[120] P. Lamparter and R. Kniep, Phys. B Condens. Matter **234**–**236**, 405 (1997).
[121] S. Davis and G. Gutiérrez, J. Phys. Condens. Matter **23**, 495401 (2011).
[122] K. Sankaran, L. Goux, S. Clima, M. Mees, J.A. Kittl, M. Jurczak, L. Altimime, G.-M. Rignanese, and G. Pourtois, ECS Trans. **45**, 317 (2012).

[123] R.A. Miron and K.A. Fichthorn, J. Chem. Phys. **119**, 6210 (2003).
[124] F. Thibault-Starzyk, E. Seguin, S. Thomas, M. Daturi, H. Arnolds, and D.A. King, Science. **324**, 1048 (2009).
[125] J.H. Kwak, J. Hu, D. Mei, C.W. Yi, D.H. Kim, C.H.F. Peden, L.F. Allard, and J. Szanyi, Science. **325**, 1670 (2009).
[126] S.K. Lee, S.B. Lee, S.Y. Park, Y.S. Yi, and C.W. Ahn, Phys. Rev. Lett. **103**, 4 (2009).
[127] S.K. Lee, S.Y. Park, Y.S. Yi, and J. Moon, J. Phys. Chem. C **114**, 13890 (2010).
[128] B. Xiao and S. Watanabe, Nanoscale **6**, 10169 (2014).
[129] J. Xie, N. Imanishi, T. Zhang, A. Hirano, Y. Takeda, and O. Yamamoto, Mater. Chem. Phys. **120**, 421 (2010).
[130] R. Ruffo, S.S. Hong, C.K. Chan, R.A. Huggins, and Y. Cui, J. Phys. Chem. C **113**, 11390 (2009).
[131] M. Wu, B. Xu, and C. Ouyang, Chinese Phys. B **25**, 18206 (2016).
[132] T. Tsuruoka, K. Terabe, T. Hasegawa, and M. Aono, Nanotechnology **21**, 425205 (2010).
[133] H. Eshet, R.Z. Khaliullin, T.D. Kühne, J. Behler, and M. Parrinello, Phys. Rev. B **81**, 184107 (2010).
[134] N. Kuwata and N. Iwagami, Solid State Ionics **180**, 644 (2009).

List of Publications

Review papers

1. Wenwen Li, Yasunobu Ando and Satoshi Watanabe. “Study of Cu diffusion in amorphous Ta_2O_5 using a neural network potential”, Journal of the physics society of Japan (Under review)

2. Wenwen Li, Yasunobu Ando, Emi Minamitani and Satoshi Watanabe. “Study of Li atom diffusion in amorphous Li_3PO_4 with neural network potential” *to be submitted.*

International Conferences

1. Wenwen Li, Yasunobu Ando, Emi Minamitani and S. Watanabe, 2016 MRS fall meeting and exhibit, America, Nov, 2016.

2. Wenwen Li, Yasunobu Ando, Emi Minamitani and S. Watanabe, AEARU forum materials workshop and the 12^{th} TU-UT-SNU student workshop, Korea, Oct, 2016.

Domestic Conferences

1. Wenwen Li, Yasunobu Ando, Emi Minamitani and S. Watanabe, International Symposium on Atomic Switch: Invention, Practical Use and Future Prospect, Tsukuba, Japan, Mar, 2017.

2. Wenwen Li, Yasunobu Ando, Emi Minamitani and S. Watanabe, 2016 MRS fall meeting and exhibit, America, Nov, 2016.

3. Wenwen Li, Yasunobu Ando, and S. Watanabe, The 18th Asian Workshop on First-Principles Electronic Structure Calculations, Kashiwa, Japan, Nov, 2015.

4. Wenwen Li, Yasunobu Ando, and S. Watanabe, The 41th symposium on Solid State Ionic in Japan, Sapporo, Japan, Nov, 2015.

Acknowledgements

First of all, I would like to express my deepest gratitude to Professor Satoshi WATANABE, who supervised me in my Ph. D course. Professor WATANABE gave me continuous guidance, meticulous suggestions in my research. Without his patience, encouragement and professional instruction, the completion of this dissertation would be impossible. Also, I would like to thank my co-supervisor, Professor Emi MINAMITANI, for her valuable suggestions in my research.

I am deeply grateful to Dr. Yasunobo ANDO for his very helpful guidance and advice on my research topics. His rich experience and experience in the field of both machine learning techniques and first-principles calculation benefited me greatly. Also, I would like to express my gratitude to each of the members of Watanabe-Minamitani laboratory, for the pleasure time we work together.

It is my pleasure to express my gratitude to my five advisors, Professor Shu YAMAGUCHI, Professor Teruyasu MIZOGUCHI, Professor Shunsuke YAGI, Professor Shinji TSUNEYUKI and Professor Koji TSUDA, for their valuable advice.

I would like to thank my parents, my sister and my fiancee Aili SUN for their continuous support and encouragement.

June 1, 2017

Wenwen Li